Integrated shimming for parallel NMR spectroscopy

Zur Erlangung des akademischen Grades eines

DOKTORS DER INGENIEURWISSENSCHAFTEN (Dr.-Ing.)

von der KIT-Fakultät für Maschinenbau des

Karlsruher Instituts für Technologie (KIT)

angenommene

DISSERTATION

von

M. Sc. Yen-Tse Cheng

Tag der mündlichen Prüfung:	29.10.2024
Hauptreferent:	Prof. Dr. Jan G. Korvink
Korreferent:	Prof. Dr. Ahmet Cagri Ulusoy
Betreuender Mitarbeiter:	Dr. Mazin Jouda

Karlsruher Institut für Technologie
Institut für Mikrostrukturtechnik
Hermann-von-Helmholtz Platz 1
76344 Eggenstein-Leopoldshafen

Abstract

This thesis explores the challenges of parallel nuclear magnetic resonance (NMR) spectroscopy, focusing on key technical hurdles. Such hurdles include the need to achieve exceptional B_0 homogeneity and efficient inter-detector radiofrequency (RF) signal decoupling. The four-part exploration introduces innovative solutions, ranging from a compact detector system for parallel B_0 shimming to a tuned RF detector merging butterfly coil and stripline technologies. Additionally, the thesis explores the combination of parallel NMR with signal amplification by reversible exchange (SABRE) hyperpolarization and addresses obstacles in high-throughput drug development by introducing a novel approach for rapid shimming of parallel detectors. This comprehensive overview provides the background for a detailed examination of each contribution.

Part 1: Parallel NMR Environment for Accelerated Analysis at 1.05 T Field: The first segment addresses the challenges of parallel NMR spectroscopy, proposing a compact detector system featuring two NMR unit cell (NC) resonators. This system successfully implements parallel B_0 shimming and RF detection, achieving local field correction within a 1.05 T permanent magnet. Signal cross-coupling is significantly suppressed, leading to narrow spectral linewidths (from 400 Hz to 28 Hz) and overcoming spatial inhomogeneity.

Part 2: Compact Tuned Magnetic Resonance Detector: The second part introduces a novel magnetic resonance detector that combines the conductor topology of a butterfly coil with that of a stripline. This design increases the magnetic field intensity $\mathbf{B}_1$ per unit current, doubling the detection signal-to-noise ratio (SNR) for mass-limited samples. The detector demonstrates improved RF shielding within an array of similar detectors. It is also compatible with 2D planar manufacturing and surface micromachining.

Part 3: Parallel NMR with Signal Amplification by Reversible Exchange (SABRE) Hyperpolarization: The third section explores the synergy of parallel NMR with SABRE hyperpolarization, demonstrating the continuous hyperpolarization of two samples through a low-field parallel probehead. This innovative approach enhances the versatility of SABRE hyperpolarization in parallel NMR experiments.

Part 4: Development of Parallel Spectroscopy at 15.2 T Field: The final part focuses on how the technical obstacles that emerged during the low-field experiment was overcome. As a result of our implementation, a new fabrication method for stripline coils is reported, based on an origami technique, that facilitates further up-scaling in the number of detection sites within the magnet bore. An improved linewidth (one is 7 Hz and the other is 4 Hz)

was achieved through compact high-order local shimming set. Besides, a deep learning approach is used to rapidly calibrate parallel detectors.

Zusammenfassung

In dieser Arbeit werden die Herausforderungen der parallelen Kernspinresonanzspektroskopie (NMR) untersucht, wobei der Schwerpunkt auf den wichtigsten technischen Hürden liegt. Zu diesen Hürden gehört die Notwendigkeit, eine außergewöhnliche B_0-Homogenität und eine effiziente Entkopplung der Radiofrequenz (RF)-signale zwischen den Detektoren zu erreichen. In dieser vierteiligen Untersuchung werden innovative Lösungen vorgestellt, die von einem kompakten Detektorsystem für paralleles B_0-Shimming bis hin zu einem abgestimmten RF-Detektor reichen, der Butterfly-Spulen- und Stripline-Technologien vereint. Darüber hinaus wird die Kombination der parallelen NMR mit der Signalverstärkung durch reversible Austauschhyperpolarisation (SABRE) untersucht und es werden Hindernisse bei der Entwicklung von Arzneimitteln mit hohem Durchsatz durch die Einführung eines neuartigen Ansatzes für das schnelle Shimming von parallelen Detektoren angegangen. Dieser umfassende Überblick liefert den Hintergrund für eine detaillierte Untersuchung der einzelnen Beiträge.

Teil 1: Parallele NMR-Umgebung für die beschleunigte Analyse im 1.05 T Feld: Der erste Teil befasst sich mit den Herausforderungen der parallelen NMR-Spektroskopie und schlägt ein kompaktes Detektorsystem mit zwei NMR-Einheitszellen (NC)-resonatoren vor. Dieses System implementiert erfolgreich paralleles B_0 Shimming und RF-Detektion und erreicht eine lokale Feldkorrektur innerhalb eines 1.05 T Permanentmagnet Magnetresonanztomographens (MRT). Signal-Kreuzkopplungen werden deutlich unterdrückt, was zu schmalen spektralen Linienbreiten führt, und räumliche Inhomogenität überwindet.

Teil 2: Kompakter abgestimmter Magnetresonanzdetektor: Im zweiten Teil wird ein neuer Magnetresonanzdetektor vorgestellt, der die Leitertopologie einer Butterfly-spule mit der einer Stripline-spule kombiniert. Dieses Design erhöht die magnetische Feldstärke $\mathbf{B}_1$ pro Stromeinheit und verdoppelt damit das Signal-Rausch-Verhältnis (SNR) für Proben mit begrenzter Masse. Der Detektor weist eine verbesserte RF-Abschirmung innerhalb einer Reihe ähnlicher Detektoren auf. Er ist auch mit der 2D-Planarfertigung und der Oberflächenmikrobearbeitung kompatibel.

Teil 3: Parallele NMR mit SABRE-Hyperpolarisation: Der dritte Teil erforscht die Synergie der parallelen NMR mit der SABRE-Hyperpolarisation und demonstriert die kontinuierliche Hyperpolarisation von zwei Proben durch einen parallelen Detektorkopf in einer niedrigen magnetischen Feldstärke. Dieser innovative Ansatz erweitert die Vielseitigkeit der SABRE-Hyperpolarisation in parallelen NMR-Experimenten.

Teil 4: Entwicklung der parallelen Spektroskopie im 15.2 T Feld: Der letzte Teil konzentriert sich darauf, wie technischen Hindernisse überwunden wurden, die während der Niedrigfeld-Experimente auftraten. Als Ergebnis dieser Implementierung wird eine neue Herstellungsmethode für Stripline-spulen basierend auf einer Origami-Technik vorgestellt, die eine weitere Skalierung der Anzahl der Detektionsstellen innerhalb der Magnetbohrung ermöglicht. Durch ein kompaktes lokales Shimming-Set hoher Ordnung wird eine verbesserte Linienbreite erreicht. Außerdem wird ein Deep-Learning-Ansatz genutzt, um parallele Detektoren schnell zu kalibrieren.

Contents

Nomenclature

Abbreviation	Meaning
ICON	Icon magnet
NMR	Nuclear magnetic resonance
NC	NMR unit cell
SNR	Signal to noise ratio
SH	Spherical harmonic
IC	Integrated circuit
FEM	Finite element
SABRE	Signal amplification by reversible exchange
RF	Radio frequency
LNA	Low noise amplifier
SRF	Self resonance frequency
RS	Regular stripline
FWHM	Full-width half-maxumum
PHIP	Para-Hydrogen Induced Polarization
DNP	Dynamic Nuclear Polarization
SEOP	Spin-Exchange Optical Pumping
ppm/ppb	Parts per million/billion
AC/DC	Alternating/Direct current
ROI	Region of Interest
PI	Polyimide
OD	Outer diameter
ID	Inner diameter

1 Introduction

1.1 Motivation

This research focuses on the concept of parallel detection, which refers to the simultaneous detection of multiple signals or stimuli in a coordinated and efficient manner. To illustrate this, consider the unique structure of insect eyes, which allow them to detect motion, color, and polarization with exceptional sensitivity and resolution. Insect eyes are organized in an array comprising thousands of individual photo-receptor units called Ommatidia. Each unit consists of a lens, many photo-receptor cells, and a crystalline cone, densely arranged in a hexagonal pattern to enable a wider field-of-view. As light enters their eyes, it is detected by the photoreceptor cell array for specific wavelengths, which are then combined to produce a composite image. The remarkable feature of this array is its parallel detection capability.

In engineering and science, techniques such as parallel detection involve using numerous detectors that simultaneously collect data from various sources or samples. Parallel detection has become quite prevalent and offers numerous benefits, including an increase in the speed and efficiency of data collection and analysis. For instance, microarray analysis is a parallel detection technique utilized to determine the presence or absence of particular DNA or RNA sequences in a sample using multiple probes on a single microarray chip [1]. Optical imaging is another parallel detection technique that employs a diode array to capture images from different sections or parts of a sample (e.g. to simultaneously record the activity of many neurons) [2] This technique enhances imaging speed and accuracy, especially for large or complicated samples. Some examples have even been commercialized, as in the example of CMOS imaging sensors that use photodiodes as light-sensitive elements for medical applications [3]. In another example, robotics are able to recognize slippage or surface texture using using an array of tactile sensors with capacitive or inductively sensitive elements [4].

Scientists have also applied parallel detection to magnetic resonance imaging (MRI), prompting the invention of the MRI array for faster and higher-resolution medical

images[5]. However, this parallel concept has not been fully and extensively investigated in NMR spectroscopy research. As one of the most robust characterization tools, scientists have favored NMR spectroscopy for studying the molecular properties of molecules or atoms, as well as in structural biology to investigate the folding mechanism of proteins. Generally, it has several advantages over other characterization methods:

- Non-destructive analysis: NMR spectroscopy does not damage the sample, so it can be used to study delicate or sensitive materials.
- Structural information: NMR spectroscopy can provide detailed structural information about molecules, including their shape, size, and physical orientation.
- Chemical specificity: The method is highly chemically specific, meaning it can distinguish between different types of atoms in a molecule based on their magnetic properties.
- Quantitative analysis: The method can be used to measure the concentration of different components in a sample, making it useful for quantitative analysis.

Over time, addressing certain drawbacks of NMR has grown increasingly imperative: its intrinsic low sensitivity, the long measurement time needed for extensive sample quantities, and the challenges associated with handling and detecting various samples. Therefore, the concept of array and unit-cell organization of ommatidia holds promise for advancing high-throughput NMR, constituting the central focus of this thesis.

1.2 Thesis outline

This thesis focuses on the development of parallel probe design methods based on a multi-coil array. The work can be divided into five main chapters (Chapter 2 to Chapter 6). In **Chapter 2**, the general concept of NMR is outlined, and the current NMR hardware specific to the detectors is explained. The challenges of utilizing an array coil in NMR spectroscopy are investigated. **Chapter 3** presents the first objective of this work: an integrated shimming system with more than one detector on-site. In this work, a concept of an NMR unit cell (NC) is proposed, which contains a local shim set, an RF coil, and a sample handling tube, as a building block for parallel NMR spectroscopy. Its NMR performance is evaluated, and its compatibility with the current low-field magnet system is considered.

In **Chapter 4**, the second thesis objective involves the creation of a completely new design of a stripline coil as an RF detector. The design mimicking the butterfly geometry is discussed. Because some samples of precious materials cannot be obtained in large quantities, there is a significant need for a sensitive RF detector. Since the idea targets parallel spectroscopy, comprehensive investigation is conducted to ensure the detectors can work independently and minimize signal cross-contamination.

In **Chapter 5**, the third objective of this thesis aims to demonstrate how the combination of the hyperpolarization technique enables signal enhancement via a custom-built parallel probe at 1.05 T low field. Because the SNR is the key to high-throughput screening, the viability of SABRE on two different molecules simultaneously in two detection sites is explained. Furthermore, the effects of the flow rate on the NMR performance are discussed.

Chapter 6 details the adaptation and adjustment of the NC-based probe for use in the 15.2 T magnet at higher field strength. Two new probehead designs, namely a four-channel static parallel probe and a two-channel flow probe, are introduced. Higher-order local shims are meticulously designed and implemented, based on the simulations and experimental findings. Additionally, an AI method is showcased to address the challenges of shimming on a two-shim set system.

1.3 Main results

The research conducted within this PhD project has led to five main publications (four of which are published and one of which is in preparation) with a contribution as first author or shared first authorship and one publication as coauthor.

- **Sample-centred shimming enables independent parallel NMR detection**
  Published in Scientific Reports, 2022. [J1, C1,& C2]
  Author status: First authorship
  Content: This paper presents a method to tackle the low throughput problem in NMR spectroscopy machines by employing the idea of parallel NMR detection. A dual NMR detection coil system with integrated active shimming coils was developed for a 1.05 T permanent magnet system.
  Contributions: Designed, constructed, and fine-tuned the experimental configuration. Carried out system characterization, executed parallel NMR experiments, and conducted data analysis. Took the lead in manuscript writing and figure preparation.

- **A field focusing butterfly stripline detects NMR at higher signal-to-noise ratio**
  Published in Journal of Magnetic Resonance, 2023. [J2]
  Author status: First authorship
  Content: This work provides a new butterfly stripline NMR coil for mass-limited samples. Such a design increases the B_1 field and resulting SNR while simultaneously reducing the field outside of the active region of the coil.
  Contributions: Designed, fabricated, and fine-tuned the butterfly stripline. Conducted NMR experiment and analyzed the final data and led in writing the manuscript.

- **Artificial intelligence (AI) driven shimming for parallel high field nuclear magnetic resonance**
  Published in Scientific Reports, 2023. [J3]
  Author status: Shared first authorship with Moritz Becker.
  Contributions: This paper presents a parallel NMR probe for a 15.2 T field MRI magnet adapted from the NC idea [J1]. Higher-order, sample-centered shimming elements is implemented. Moreover, Deep learning was used to cope with overlapping non-orthogonal shimming fields, achieving a faster shimming process than the conventional method.
  Content: Designed and fabricated the hardware part of this project. Conducted the major NMR experiments, apart from the artificial intelligence (AI) part. Analyzed the data and wrote the manuscript with Moritz Becker.

- **Continuous flow high throughput parallel SABRE**
  In preparation. [J5]
  Author status: Shared first authorship with Jing Yang
  Content: This work presents a system combining parallel probeheads and SABRE hyperpolarization to increase the intrinsic low-throughput nature of NMR. The paper describes significant signal enhancements in the parallel NMR spectrum.
  Contributions: Conceived the idea and modified the parallel probe to incorporate the flow system utilized for SABRE. Analyzed the data and led the writing of the manuscript with Jing Yang.

- **A digital twin for parallel NMR spectroscopy**
  Published in Communication Engineering, 2024. [J4]
  Author status: Coauthor
  Content: This paper presents a framework to solve the excitation pulse interference problem and a blind source separation method to decouple parallel spectra during

parallel NMR experiments.

Contributions: Performed parallel NMR experiment using self-built probe.

2 Background Information

2.1 Overview

In 1938, Isidor Isaac Rabi from Columbia University discovered the magnetic moment of a deuteron utilizing a molecular beam magnetic resonance method (the former term for NMR) [6]. He then was awarded the Nobel Prize in 1944. In the following years, several researchers contributed significantly to the development of NMR, including Felix Bloch [7] and Edward M. Purcell [8], who first demonstrated the technique in the late 1940s. They demonstrated that atomic nuclei with an odd number of protons and/or neutrons possess a quantum mechanical property called "spin" with an associated fundamental property called "spin angular momentum" that can be manipulated and detected by radio frequency (RF) coils inside a static magnetic field. Later, Paul Lauterbur [9] and Sir Peter Mansfield [10] developed the concept of utilizing NMR for medical imaging. Lauterbur proposed using a gradient field to encode spatial information into the NMR signals. Meanwhile, Mansfield developed a mathematical method for processing these signals into magnetic resonance imaging (MRI), which became one of the most important tools for medical diagnosis.

RF coils are crucial in determining the quality of MRI images, as they directly impact image resolution and measurement times. Peter B. Roemer was the first to utilize an array of coils to MRI [11], which improves spatial resolution and SNR. In recent decades, most research efforts in medical imaging have attempted to advance array coils. However, there has been limited attention to or utilization of array coils in the realm of NMR spectroscopy.

This chapter is outlined as follows. The fundamentals of NMR are introduced in Sec. 2.2, followed by a discussion of NMR hardware in Sec. 2.3. The core of this thesis is presented in Sec. 2.4, which explores the challenges of applying coil arrays in NMR spectroscopy.

2.2 NMR fundamentals

The nucleus of an atom contains protons and neutrons, which create a positive charge. Such particles possess a natural angular momentum, as illustrated in Fig. 2.1a. Spin can be interpreted as an intrinsic property indicating the particle's intrinsic angular momentum. For an equation that correlates the magnetic moment ($\vec{\mu}$) of a spin and with angular momentum ($\vec{S}$) by the gyromagnetic ratio (γ) of the nuclei, see Eq. 2.1.

$$\vec{\mu} = \gamma\vec{S} = \gamma\vec{I}\hbar \tag{2.1}$$

The gyromagnetic ratio determines the strength of the magnetic moment associated with a given angular momentum. The angular momentum is correlated to the quantum number ($\vec{I}$) of the particle, and is used to quantify the particle's susceptibility to magnetic fields. Based on the sign of the gyromagnetic ratio, spins in a magnetic field proceed in one of two ways: parallel or anti-parallel to the axis of the field. For a nucleus with a positive gyromagnetic ratio ($\gamma > 0$), the direction of the magnetic moment is parallel to the angular moment, and vice versa. The orientation difference is depicted in Fig. 2.1b.

The NMR phenomenon occurs when the spins interact with static magnetic fields (B_0). The spins can either be aligned with or antiparallel to the external magnetic field. In the absence of a magnetic field, the spins of the protons are oriented randomly. Under a strong external magnetic field, the energy of the spin system is quantized in $2I+1$ levels. This is known as the Zeeman effect. Spins change their orientation to parallel or anti-parallel to the direction of the magnetic field (Fig. 2.1c). And the magnetic moment of the dipole starts to precess at the Larmor frequency ω_0, which can be formulated as:

$$\omega_0 = -\gamma B_0 \tag{2.2}$$

This phenomenon resembles the behavior of a gyroscope, which spins around its axis when deviating from the direction of gravity. Similarly, when the axis of rotation deviates from the direction of the external magnetic field, the nucleus will virtually spin around its axis while precessing around the direction of the magnetic field. It is important to note that the gyroscope is influenced by Earth's gravity, whereas the nuclear magnetic moment is influenced by the external magnetic field B_0.

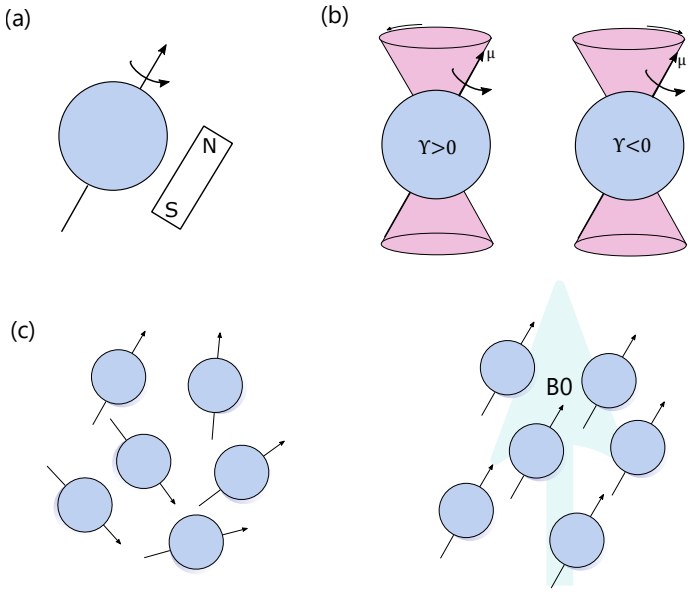

Figure 2.1: (a) An atomic nucleus' spin generates a magnetic moment, acting like a tiny magnet bar. (b) The precessing of spin polarization in a static magnetic field (B_0). Processing direction is determined by the spin's gyromagnetic ratio (γ). (c) The distribution of the nucleur spins when the magnetic field is absent, chaotic, and disordered. In the presence of the magnetic field, their orientation is parallel or antiparallel to the field direction.

Taking the proton with the quantum number of 1/2 as an example, in the presence of a static field, there are two possible spin energy levels, the lower energy level (α) and the higher energy level (β). The energy difference is proportional to the static field strength:

$$E = -\vec{\mu} \cdot B_0 = -\gamma \vec{I} \hbar \cdot B_0 \tag{2.3}$$

It is noted that a single spin is not exactly at one of the two energy levels α or β. Instead, an ensemble of spins is considered. Based on the Boltzmann distribution, the spin's probability distribution occupying one of the two available energy states is ($e^{-\frac{E}{K_B T}}$), where K_B stands for the Boltzmann constant and T for the temperature. The following approximation is based on the high-temperature condition. The net magnetization (M_0) along the direction of static field (z) for the spin ensemble (N) can be written as follows [12]:

$$M_0 = M_z \simeq \frac{N\gamma^2 \hbar^2 B_0 I(I+1)}{3K_B T} \tag{2.4}$$

Based on the classical definition in physics, a magnetic moment present in an external magnetic field produces a torque (τ) to align the dipole in the field direction $\tau = M \times B$. When a transverse oscillating magnetic field (B_1) is applied to the ensemble during

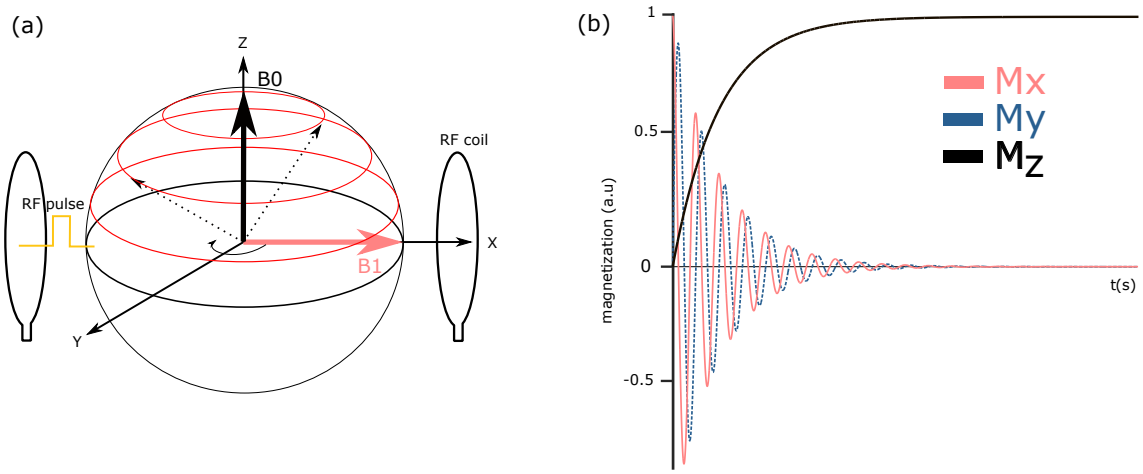

Figure 2.2: (a) Schematic demonstration of net magnetization of the spin ensemble after a transverse B_1 field is applied through the RF coil. (b) The magnetic field generated from the precessing magnetic moment is detected by the RF coil.

excitation, the net magnetization vector flips to X-Y plane (Fig. 2.2a). The transverse net magnetization reaches its maximum, and the longitudinal starts to decrease to zero when the flip angle reaches 90°. As the nuclei relax back to their ground state, they emit energy in the form of electromagnetic radiation, which a coil can detect. Therefore, what follows are the three vector components after excitation (M_z, M_x, and M_y) based on the Bloch equations:

$$\frac{d}{dt}\begin{pmatrix} M_x \\ M_y \\ M_z \end{pmatrix} = \begin{pmatrix} -\frac{1}{T_2} & \gamma B_z & -\gamma B_y \\ -\gamma B_z & -\frac{1}{T_2} & \gamma B_x \\ \gamma B_y & -\gamma B_x & -\frac{1}{T_1} \end{pmatrix} \begin{pmatrix} M_x \\ M_y \\ M_z \end{pmatrix} + \begin{pmatrix} 0 \\ 0 \\ \frac{M_0}{T_1} \end{pmatrix} \tag{2.5}$$

Since the coherence of the transverse field does not last forever, the transverse vector decays in the constant of T_2, which is defined as the spin-spin relaxation time constant. T_1 is defined as the spin-lattice relaxation time constant, reverting the spin to a thermal equilibrium state through a relaxation frequency. Fig. 2.2b plots three vectors of net magnetization as they relax back to the thermal equilibrium.

2.3 NMR hardware

To measure this tiny magnetic signal, NMR spectrometers are built to produce two key main fields, a large static magnetic field to create sufficient net magnetization and an

oscillating field to impose the ensemble to a 90° flip angle. Some NMR experiments require gradient fields (i.e., diffusion experiments). Modern NMR spectrometers contain several key components: a magnet, shimming coils, RF coils, and gradient coils (Fig. 2.3). In the following section, state-of-art miniaturized RF coils used in NMR are listed in the next section. The other key element, shimming is discussed in the Sec 2.4.2

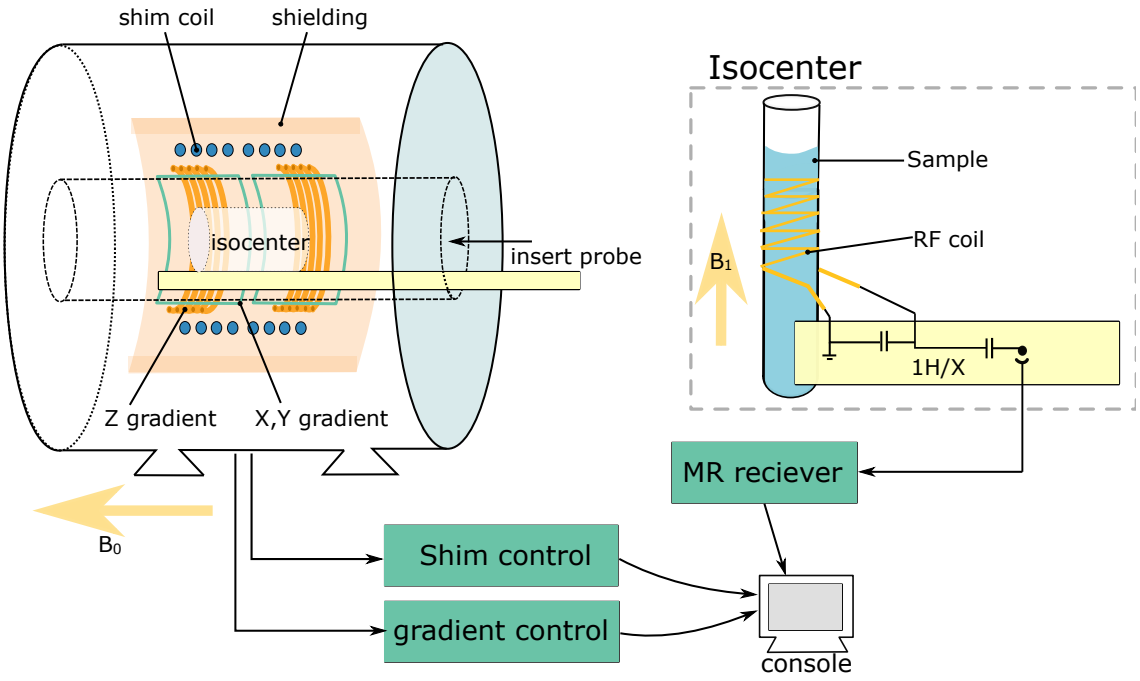

Figure 2.3: Schematics depict the major components inside the NMR magnet.

NMR RF coils

From a geometrical point of view, an RF coil is a continuous element that transmits and receives RF signals. According to the Biot-Savart law, the summation of the magnetic field generated by the current flowing through each discrete element contributes to the final RF field. In the current decade, scientists have pursued coil optimization, aiming to design RF coils based on different coil topologies [13, 14]. The core concept of coil optimization is to efficiently deliver RF pulses to the spin population and receive a high-resolution spectrum, while avoiding the penalty of measurement time. For example, Minard et al. have established practical guidelines for micro solenoid coils aimed at maximizing NMR sensitivity with sufficient B_1 homogeneity [15].

The use of coil arrays for NMR has led to new design considerations. Several groups of scientists have invented parallel probehead with different coils for different field magnets[16, 17]. One natural manifestation of the new design involves expanding the

number of coils into an array. Such practices reduce the N-fold measurement time (where N is the number of coils) without SNR penalty. To allow more coils implemented in a single probehead, Wang et al. [16] constructed an eight-coil probehead with micro solenoids. Another manifestation involves preventing signal cross-coupling through hardware or post-processing. Despite parallel spectroscopy has been demonstrated, there is still an absence of a standardized guideline for designing NMR coil arrays for spectroscopy and it remains largely unexplored in the existing literature.

Optimizing coil performance for NMR spectroscopy is a complex problem since several parameters need to be improved simultaneously. The first is SNR while detecting the sample spins. Second, B_0 homogeneity across the sample spins. Third, B_1- homogeneity across the sample spins, Fourth, RF coil Q-factor, and last but not least, the self-resonance frequency of the RF coil.

SNR maximization minimizes both the measurement time and the material's limit of detection (LOD). It is also vital to have sufficient B_0 homogeneity to obtain high-resolution NMR spectra, i.e. J coupling between chemically bonded nuclei is 7 Hz. Moreover, B_1 homogeneity must be increased to improve SNR or it will degrade the NMR response. In situations involving a higher field magnet, the coil should have a high enough self-resonance frequency (SRF) to tune and match the coil at the nucleus' Larmor frequency. The following section introduces the fundamental theory and figures of merit of NMR transceivers and describes several coil topologies and related fabrication processes.

Singal-to-noise ratio (SNR)

The SNR that results from applying a 90° pulse to the sample measures the quality of the NMR RF detector. An ideal RF detector should be sensitive enough to acquire the precession of the spin, which is in the form of a magnetic field, at the lowest noise level. The SNR of the coil can be written in the simple form shown below:

$$\mathrm{SNR} = \left(\frac{V_{signal}}{V_{noise}} \right) \tag{2.6}$$

As Hoult and Richards [12] stated, the principle of reciprocity is given by [18]

$$\mathrm{SNR} = \left(\frac{B_1}{i}\right) \cdot \frac{k_0 \nu_s N \hbar^2 I(I+1)\omega_0^2 / 3\sqrt{2} K_B T}{V_{noise}} \tag{2.7}$$

In Eq.2.7, B_1/i is the magnetic field per unit current i at the Larmor spin precession frequency ω_0. The constant k_0 accounts for B_1 inhomogeneity. The parameters $\nu_s N$ represent the number of spins involved, I represents the spin quantum number, and $\hbar$ is the Planck constant. The noise voltage associated with the signal is represented by V_{noise} and is mainly dependent on the coil's resistance. The R_{noise} accounts for the coil's resistance and sample losses at the Larmor frequency. The calculation for V_{noise} then can be written as follows, for a given receiver's bandwidth Δf:

$$V_{noise} = \sqrt{4 K_B T R_{noise} \Delta f} \tag{2.8}$$

Eq. 2.8 has been substituted by Eq. 2.7, assuming a uniform sample filling of the coil, as well as a homogeneous B_1. Consequently, the SNR and coil's quality are defined by the coil's field per unit current per square root of its resistance.

$$\mathrm{SNR} \propto \frac{B_1}{i} \cdot \frac{1}{\sqrt{R_{noise}}} \tag{2.9}$$

B_1 uniformity

The magnetic field (B_1 field) determines both the excitation profile and a coil's receiving sensitivity during NMR acquisition. As defined in this NMR experiment, B_1 inhomogeneity refers to the spatial variance of the RF field in terms of strength and direction generated by the RF coil. The fundamentals of signal acquisition from the magnetization precession of the sample were determined, given a sample volume (V_s) in the static field of B_0 in the Z direction. The sample was then divided into multiple units. For each sample unit at location (r), the transverse component of magnetization of the unit volume ($M_{xy}(r)$) rotates the Z-axis at the Larmor frequency (ω). Based on the Faraday law of induction, the

precession induces the unit voltage ($\zeta(r)$). Based on the Hoult and Richart's principle of reciprocity for the emf induced in the coil[12]:

$$\zeta = -\int_{sample} \frac{\partial}{\partial t}\mathbf{B}_1 \cdot \mathbf{M}_0 \, dV_s \tag{2.10}$$

for the changing magnetization during the precession step. The time-varying voltage induced per unit sample volume can be rewritten as follows:

$$\zeta(r) = \omega \cdot \mathbf{B}_1(r) \cdot \mathbf{M}_{xy}(r) \tag{2.11}$$

This can be illustrated differently, with respect to the center (r=0) of the RF coil. For the sample located at the center, the induced voltage is $\zeta(0)$. So in the Eq. 2.11, the NMR response can be written as follows:

$$\zeta(r) = \omega(\mathbf{B}_1(0) - \Delta\mathbf{B}_1(r)) \cdot (\mathbf{M}_{xy}(0) - \Delta\mathbf{M}_{xy}(r)) \tag{2.12}$$

In light of Eq. 2.12, the NMR response deviation between r=r and r=0 is $\zeta(r) = \zeta(0) - \Delta\zeta$ for any coil topology, even one designed for optimal B_1 homogeneity. The B_1 is almost never constant since there is generally some fabrication error, even if it is negligible. Taking the deviation of the NMR response of r from the center. The fraction of this deviation $\Delta\zeta$ and $\zeta(0)$:

$$\begin{aligned} \frac{\zeta(r) - \zeta(0)}{\zeta(0)} &= \frac{(\mathbf{B}_1(0) - \Delta\mathbf{B}_1(r)) \cdot (\mathbf{M}_{xy}(0) - \Delta\mathbf{M}_{xy}(r)) - \mathbf{B}_1(0) \cdot \mathbf{M}_{xy}(0)}{\mathbf{B}_1(0) \cdot \mathbf{M}_{xy}(0)} \\ &= \frac{\Delta\mathbf{B}_1(r) \cdot \Delta\mathbf{M}_{xy}(r)}{\mathbf{B}_1(0) \cdot \mathbf{M}_{xy}(0)} - \frac{\Delta\mathbf{M}_{xy}(r)}{\mathbf{M}_{xy}(0)} - \frac{\Delta\mathbf{B}_1(r)}{\mathbf{B}_1(0)} \end{aligned} \tag{2.13}$$

Eq. 2.13 depicts how the spatial deviation of B_1 inside the RF coil degrades the magnetization and in turn the NMR response. This variance causes non-uniform flip angles across the sample volume, resulting in the spatial difference of magnetization. For a uniform field coil, the degradation will be negligible.

The following section lists some typical forms of RF coil geometry. Due to the complexity and size of most NMR probe-head and instrumentation, it is vital to introduce the state-of-the-art miniaturized RF coil that has been invented.

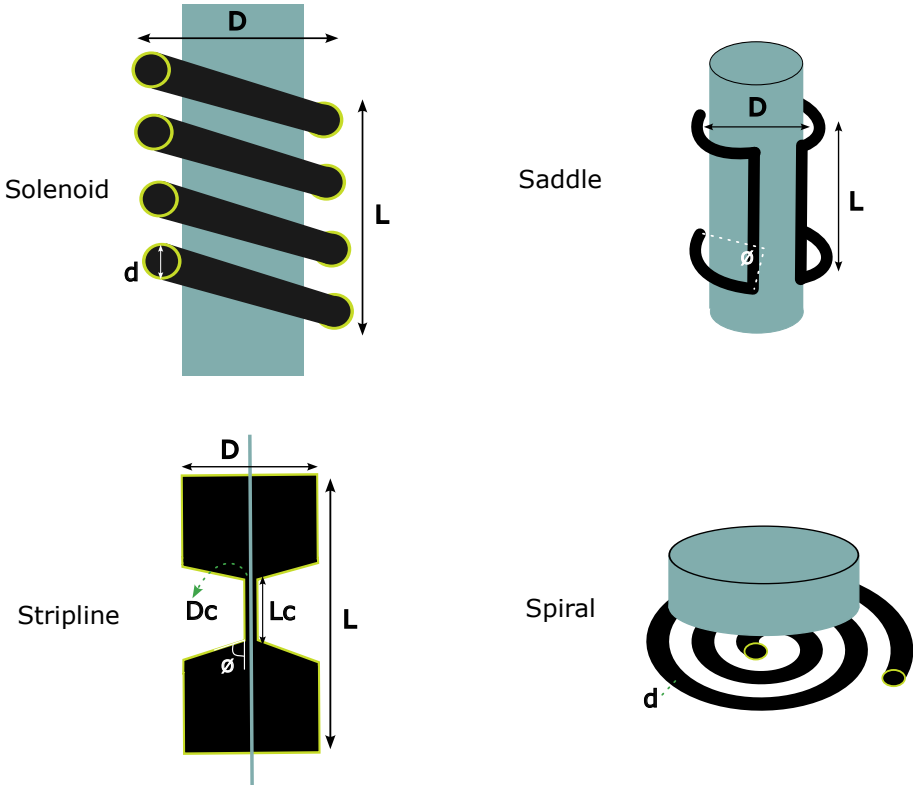

Figure 2.4: Schematics of typical RF coils utilized in NMR spectroscopy: Solenoid, Saddle, Stripline, and Spiral coil. The typical positioning of samples is colored teal. The dimensions of each coil are parameterized.

Solenoid

The solenoid coil is a common NMR detector well known for its high Q-factor. The solenoid is constructed through several windings from a metal wire, typically copper or gold. The close conformation of the solenoidal receiver coils to small samples effectively improves NMR sensitivity. The miniaturization of solenoid microcoils, with a diameter of 1mm, displays excellent mass sensitivity with comparable criteria to that of a 5mm cryogenic probe[19], without the requirement of operating the entire system in a cryogenic environment. Ehrmann et al. demonstrated an NMR microprobe based on solenoids and Helmholtz coils that were microfabricated for the analysis of cells[20]. The study indicated that solenoidal coil can be bottom-up electroplated, enabling the implementation of a flow channel inside the coil. In another fabrication method, a wire-bonding machine provided the winding motion for twining the sub-mm copper wires to a microfabricated sample-handling post [21]. This study demonstrated the potential of implementing a clean-room bench process to massively produce microcoils in large numbers.

Peck et al. [18] presented a model for the design and analysis of a microsolenoidal coil for NMR application. It is possible to parameterize the geometry of the n-turn solenoidal coil into the total length (L) with the inner diameter of (D). The following equation can be used to predict SNR performance, according to the theory of electromagnetics. The on-axis B_1 for a single-layer solenoid coil is related to the diameter and height of the coil, and according to the Eq. 2.7, the sensitivity of the solenoidal coil is defined as B_1/i:

$$\frac{B_1}{i} = \frac{\mu_0 n}{D\sqrt{1+(L/D)^2}} \tag{2.14}$$

The diameter of the copper wires is typically in the sub-mm to 10 micron range. When the diameter is below 10 microns, the typical calculation of a DC coil is no longer vaild (e.g., for a 50 MHz field magnet, the skin depth is around 9 um), and the miniaturization of coils should also consider the skin depth effect. Accounting for the skin depth in the resistance of the coil provides a more accurate estimation of the SNR. As depicted in [18], the SNR per current is

$$SNR = \frac{B_1}{i\sqrt{R}} \propto \frac{w_0^2[n/D\sqrt{1+(L/D)^2}]}{\sqrt{n^2 D w_0^{\frac{1}{2}}/L}} \propto \frac{w_0^{\frac{7}{4}}}{D} \tag{2.15}$$

There is a trend toward reducing the coil diameter for mass-limited samples with good SNR. The small sample channel is necessarily aligned perpendicular to the B_0-field. Moreover, the coils' close proximity to the sample creates strong perturbation of the B_0-field, due to the susceptibility mismatch of coil and sample.

Saddle coil

Saddle coils, which are confined to the cylindrical shape of the sample, have been utilized as NMR sensors for a long time. The two curved rectangular parts are wound onto the circular cylindrical oriented in the Z direction, generating a magnetic field in the X–Y direction. The general advantage of such a topology is that it creates uniform RF field perpendicular to the axial axis of the sample, so that the coil is less likely to perturb the B_0 field. This topology has been found to reach optimal B_1 uniformity when the angle (ϕ) is 120° and the geometrical ratio (L/D) equals to 2 [22]. The saddle-shaped coil is often

chosen for its ability to fit into tight spaces or to optimize the limited available volume. However, the miniaturization of such a coil must also consider practical aspects related to manufacturability. Since the dimensions are below the sub-mm scale, it is challenging to create a high aspect ratio of metallic structure through microfabrication.

Many examples of 3D micro-fabrication have been developed for more complex structures than the saddle coil (e.g. two-photon polymerization [23], bottom–up integration process [24], and 3D assembly assisted by residual stresses [25]). However, so far, limited literature exists on creating micro saddle coils for NMR applications. First, handling such conductive structures in small dimensions is difficult. Second, 3D microfabrication is not a practical solution for NMR saddle coils since they are usually used on polymers. There are some simple methods, such as direct winding, but these still necessitate a handling microstructure to fix the position of the wire without deformation. Wang et al.[26] utilized the inkjet printing method to print metallic structure on a thin Kapton film and wrap it onto a sample tube. They demonstrated that the coil can be used to acquire an MRI image with a diameter less than 600 mm in the sample tube. This method was further adopted to fabricate coils for NMR spectroscopy, which demonstrated an adequate linewidth (<2Hz at 500MHz field magnet)[27].

Stripline coil

There has been a systematic review of stripline, microstrip, waveguide, and antenna for MRI transceivers [28]. Here, the stipline coil or microstrip coil used in the application of NMR spectroscopy is considered. The advantages of stripline coil include higher performance concerning quality factors, high-frequency capability, and shielding capability. Van et al. [29] first proposed the stripline coil, which was adopted from the RF transmission waveguide. They reported a Q factor between 80 and 100. A conventional stripline waveguide is a symmetrical, three-layered metallic structure comprising two layers of dielectric material. The center part of the bone-shaped metallic layer generates a non-consistent RF field along the Z-axis, which is stronger at the narrow part (Dc) but weaker at the wider part (D). Moreover, due to the small gap between the strip and the ground, the symmetric ground plane confines and homogenizes the RF radiation, allowing uniform and strong RF radiation on top of the narrow part of the stripline. It is also possible to design a stripline coil with intrinsic capacitance to the ground as an untuned coil. In this case, it has the same Q as a resonant coil without the disadvantage of narrow bandwidth. The physical length of the central strip should fit with either half or a quarter of the wavelength of the excited frequency. This wavelength is generally larger than the size definition

of a microcoil when using a 500 MHz field magnet. It is also feasible to connect such coils to a tank circuit, allowing tuning and matching to the nuclei frequency. In this case, the coil can be further miniaturized. Chen et al. [30] described a microstrip design that allowed for high-performance 2D NMR spectroscopy of sub-nanoliter samples with an RF conversion efficiency of 4.18 $mT/\sqrt{W}$, and a reasonable linewidth of 1.5 Hz. Finch et al.[31] presented a similar design that accommodates planar microfluidic devices.

Spiral coil

Ideally, coils should be designed to match the dimensions of the targeted sample for optimal NMR performance. Instead of wrapping wires onto the capillary, spiral coil allows the sample to be closely placed on top of the coil. Spiral coil has been utilized as sensitive NMR microcoil due to their easy fabrication through micro-fabrication process. Several groups have demonstrated the fabrication step of the spiral microcoil is compatible with standard integrated circuit (IC) technologies for modern NMR spectroscopy [32–34].

Peck et al. [34] demonstrated the first spiral microcoil fabricated on a Gallium Arsenide substrate, with a dimension near 150 µm. They then placed silicone samples directly on the coil. However, such a design is not ideal for NMR spectroscopy, owing to the low FWHM of 60 Hz. Another drawback of the spiral micro coil is the poor B_1 homogeneity, which degrades the NMR signal.

2.4 NMR parallelism: from imaging to spectroscopy

Hyde et al. [35] introduced the MRI coil array, the first example that brought parallel detection techniques into NMR. The array employed two coils to detect an MR signal. This paper demonstrates that two receiver coils with negligible mutual inductance can halve acquisition time, potentially accelerating human imaging. Afterwards, Roemer et al. [11] borrowed the idea of phased array radar and applied it to NMR, creating the first NMR phased array. Their work showed 2X-3X SNR enhancement over results obtained with a typical rectangular coil. Overlapping adjacent coils was found to achieve minimal mutual inductance, and connecting all coils to low-input impedance preamplifiers can reduce the current flowing in the coils.

Other studies sought to increase the number of RF coils in an array. In 2004, Zhu et al. [36] constructed two 4 x 4 parallel receive-coil arrays, consisting of 32 channels, as seen

in Fig. 2.5a. Their results showed 12- to 16-fold accelerations in detection. The coils overlapped in a row with a proper distance in the column to handle the mutual induction. Later, a 96-channel coil array was developed for brain imaging in 3T [37], which used a "soccer-ball" geometry (Fig. 2.5b). The new design featured hexagonal overlapped coils, and it yielded a 1.3-fold SNR enhancement in the brain cortex compared to the 32-channel array. In parallel, Hardy et al. [38] presented a body receiving array (with 128 channels) comprising two clamshells, each containing 64 coils, with an averaged decoupling ratio between -25dB and -30dB. The design shows a 1.03 enhancement in SNR compared to the 32-channel array, with an eight-fold reduction of residual aliasing artifacts (Fig. 2.5c).

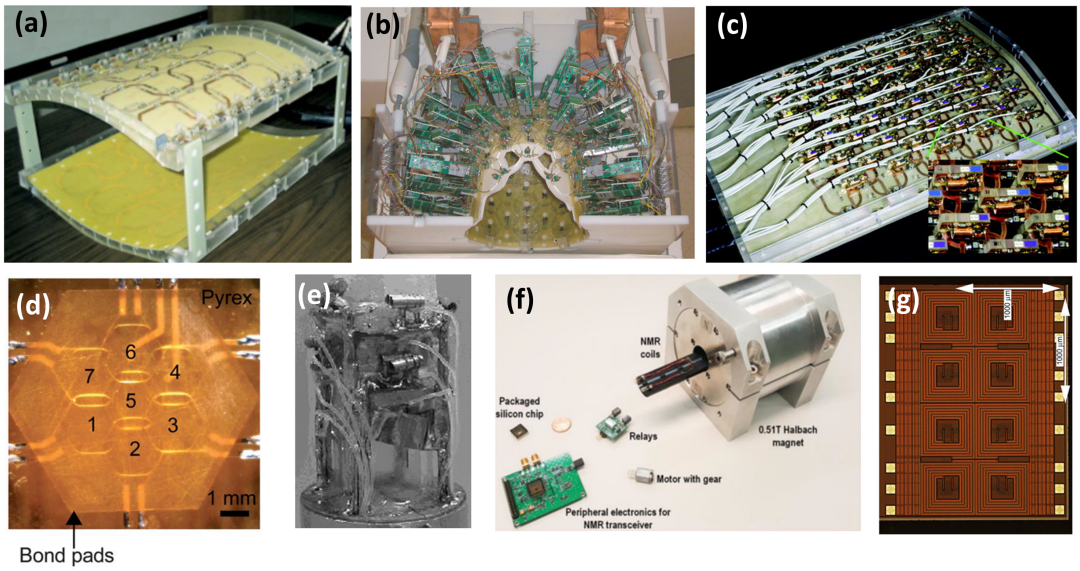

Figure 2.5: (a) Highly parallel volumetric imaging with a 32-element RF coil array. 16 elements on each side, reprinted from [36], with permission of John Wiley & Sons, Inc. (Copyright © 2004 Wiley-Liss, Inc.) (b) 96-channel soccerball-shaped receive-only head coil for 3T magnet, reprinted from [37] with permission of John Wiley & Sons, Inc. (Copyright © 2009 Wiley-Liss, Inc.) (c) 64-channel body RF receiver coil array (bottom view) is mounted in the patient cradle, reprinted from [38] with permission of John Wiley & Sons, Inc. (Copyright © 2008 Wiley-Liss, Inc.) (d) Lab on a chip phased-array NMR analysis system, reprinted from [39]. (Copyright © The Royal Society of Chemistry 2012.) (e) First eight-coil high-frequency probehead design for NMR spectroscopy, reprinted from [16], with permission of Elsevier (Copyright © 2004 Elsevier Inc.) (f) A 4-channel portable NMR system capable of parallel NMR acquisition, reprinted from [17]. (Copyright © 2020 American Chemical Society) (g) A single-chip array of NMR receivers, reprinted from [40]. (Copyright © 2009 Elsevier Inc.)

Compared to using single-receive coils, adding coils to the current MRI array has several advantages. First, adding coils yields an MRI image with enhanced SNR. Second, it increases the field of view with no time penalty. Finally, k-space sampling speeds up acquisition. In conjunction with the parallel imaging algorithms, MRI spatial data can

be acquired and reconstructed more quickly from the multiple encoding processes (e.g., SENSE-type reconstruction [41] and GRAPPA-type reconstruction[42]). Another benefit of the parallel imaging technique is that it shortens breath-hold times, resulting in fewer motion-corrupted examinations. Moreover, it permits selective excitation using parallel transmission to simultaneously excite multiple slices of tissue in the brain or body, allowing for improved control over image contrast and resolution.

From a coil geometry perspective, most MRI array coils are primarily designed in planar looped structures (i.e., surface coils). They may be organized in the shape of a cylinder or sphere for scanning humans or small animals, or particularly for certain parts of the body, like the brain or spine. The first advantage is that it is easy to overlap or position the tuning capacitors. Second, it allows the collection of signals from several object regions in parallel with high inherent SNR [43].

It is expected that applying coil arrays to spectroscopy yields numerous advantages (i.e., shorter measurement times for multiple samples, high throughput with high accuracy, and reaction monitoring that requires several detection sites). However, typical MRI coil array is generally unsuitable for spectroscopy due to the size of the sample, for example, in the case of the imaging the adult cranium. Its volume exceeds one liter, whereas typical NMR samples range from microliters to milliliters. MRI employs additional magnetic field gradients to impose a unique combination of precessional phase and frequency at each position of a sample, acquiring signals from multiple detection sites. In spectroscopy, each coil should exclusively contain only one sample to prevent information cross-contamination. Even with the application of slice selection on NMR samples for acquiring localized information, such as obtaining multiple spectra of sequential samples simultaneously. However, this approach diminishes the signal-to-noise ratio (SNR) of a single NMR spectrum, as only a specific portion of spins is involved, the surface coil introduces spatial localization through B_1 inhomogeneity (where the RF amplitude decreases with distance from the coil), which is not favored in spectroscopy.

To bridge the MRI phase array with spectroscopy, Gruschke et al.[39] demonstrated a 7-channel modular miniaturized phased array capable of micro-imaging and spectra acquisition. They acquired two spectra with 11 ppb resolution at 400 MHz field magnet successively from two non-overlapped coils.

Wang et al.[16] proposed the first practice of multiple coils in NMR probe for NMR spectroscopy (Fig. 2.5e). They showed eight COSY spectra can be parallel acquired within the 8-coil probe, showing three critical issues during the construction of the probe. First, the proximity of the micro-coil will affect the B_0 can be significantly perturbated. And due

to the limited space of homogeneous region inside the high-field superconducting magnet, the arrangement of a larger array is difficult. Third, signal cross-talk from RF coupling become a major issue.

In another study, Lei et al. [17] adapted the multi-coil arrangement in a low-field permanent environment and demonstrated multidimensional ^{1}H NMR spectroscopy using two to four NMR coils. They also incorporated shimming and motional averaging to handle the homogeneity issue and achieved < 0.16 ppm. Similarly, Anders et al. [40] developed a fully integrated reception array (eight-channel) on a single chip, thereby showing the capability of running 1D at the same time. However, the spectra resolution and mutual coupling remain problematic.

The next section briefly reviews the three key issues associated with adapting parallel detectors in NMR spectrometer, and thus provides a conceptual foundation for the rest of the article. **Some parts of the paragraph in the next three subsections are based on my previously published article [J1].**

2.4.1 Inter-coil inductive decoupling

Based on the study's definition of parallelism, the aim was to operate the coils in true synchronization, without any time delay between two acquisitions from two coils. This approach involves a strong signal cross-coupling between two NMR sensors. This signal coupling happens among nearby coils, specifically due to the injection of electromagnetic energy from one coil to another, and results from the Faraday induction and capacitive coupling among the array's elements. As Faraday's law of induction indicates, the electromotive force ε_i in loop i, is defined as the rate of magnetic flux Φ_{ij} passing through inductor loop i with area A_i, as caused by the current in inductor loop j:

$$\varepsilon_i = -N_i \cdot \frac{d\Phi_{ij}}{dt} = \frac{d}{dt} \iint_{\text{loop i}} B_j \cdot dA_i. \tag{2.16}$$

The magnetic flux seen by the sample in loop i, in turn, depends on the magnetic flux density from the neighboring loop B_j, as well as the loop's own enclosed area. Hence this causes the recorded spectra to contain signals from neighbouring samples. Consequently, a drop in one loop may overlap with a neighboring loop, either heating it or hindering charge movement. Consequently, it will also imprint an induced signal among neighboring loops. These correlations among coils could be removed in principle, for example, by invoking the orthogonality of the sensitivity map and the subsequent unravelling of coil signals. However, the noise will also couple and cannot be removed, leaving a significant

degradation of the signals since clean separation becomes difficult. In Wang et al. [16], eight identical solenoid coils were introduced for parallel NMR using separation for decoupling, with 1 to 5% of the NMR signal bleeding among the coils, even though the experiment was carried out in a time interleaved fashion.

MRI arrays have extensively used the modern decoupling method to overcome the limitation. This is accomplished using low-input-impedance pre-amplifiers combined with the overlapping of adjacent coils to reduce mutual coupling between coils [11], as seen in Fig. 2.6a. To understand how this reduces coupling, consider a model of two interacting surface coils (Coil 1 as a primary coil and Coil 2 as a secondary coil). Coil 2 is connected with a L- matching network and a pre-amplifier. If the preamplifier's input impedance is effectively close to zero, the inductor L2 creates a parallel resonant circuit with the capacitor C2, preventing current from flowing through the surface coil. This method has been widely accepted and proven effective, but it has its limitations. For example, it is nearly impossible to handle multiple samples and enable a maximum filling factor for each coil, given that one sample should be placed in the whole sensitive region and only in one coil.

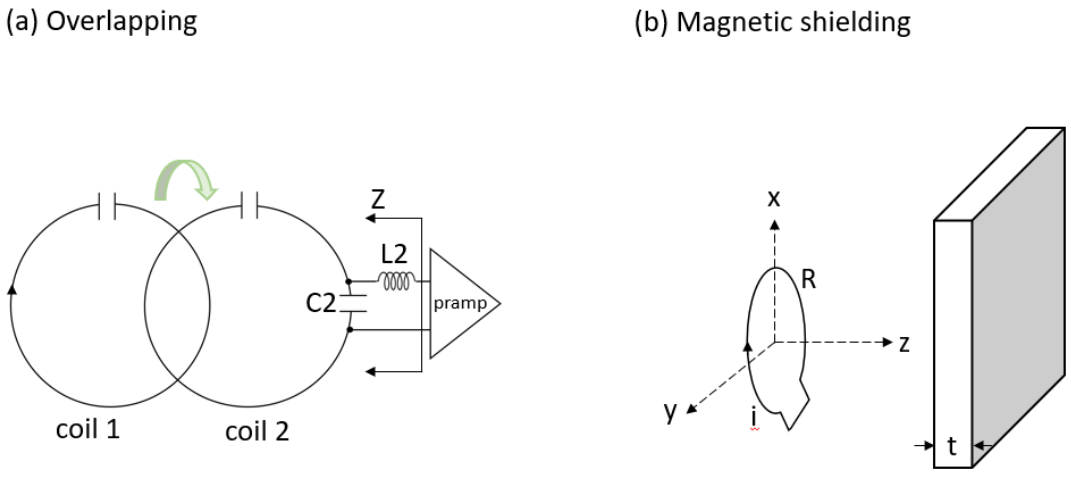

Figure 2.6: (a) A schematic description for two overlapped coils (S1 and S2). A proper aligning distance for overlapping forces the mutual inductance to zero. (b) A schematic description for a coil in parallel with an infinite shielding material.

EMI shielding and effectiveness Based on the fundamental theory of EMI shielding [44], it is possible to insert a shielding structure between two transceivers, hindering electromagnetic radiation from penetrating. Because the NMR works in a near-field region, the inter-element spacing is usually smaller than the wavelength (e.g., for a 400 MHz field magnet, the wavelength is 75 cm, while the typical RF coil size in the spectrometer is a

few centimeters). Therefore, by applying the theory based on the magnetic dipoles, the shielding effectiveness can be defined as follows:

$$SE_H = \left(20log \frac{\left|H^{inc}(r)\right|}{|H(r)|} \right) \tag{2.17}$$

The SE_H measures a material or structure's ability to block electromagnetic radiation by comparing the absolute values of the magnetic field present at a specific point beyond the shield to those of the incident field that would be present without the shield. To design the shielding structure in the application of EMI shielding in an MRI or NMR coil array, it is necessary to determine the shape of the field in the region where a reduction in field magnitude is required. Moreover, EMI effectiveness is influenced by the shield geometry, material parameters, and frequency of the emitted field when the shield is placed between the source and that region. See Fig. 2.6b for an example of a loop coil that creates a magnetic field at a lower frequency in the presence of an infinite shielding plate. The shielding effectiveness, measured behind the plate, can be written as follows, given by [44]:

$$SE_{dB} = 8.686 \frac{t}{\delta} + 20log \left[\frac{L}{8.485 \mu_r \delta} \frac{L}{(z-t)} \left(\frac{L}{\sqrt{R^2+z^2}} \right)^3 \right] \tag{2.18}$$

L denotes the measurement distance ($L = \sqrt{R^2 + (z-t)^2}$) to the coil. δ stands for the skin depth in the shield, with a relative permeability of μ_r. The above equation is based on the assumption that the measurement distance is below the wavelength, and the shielding material has sufficient thickness, twice the skin depth. Based on the Eq. 2.18, the following findings is obtained:

- The SE is independent of the distance between the coil and the shielding material, allowing us to place the shielding at any position between two coils without interfering with the shielding effectiveness when the inter-coil distance remains the same.
- The SE remains constant with the change in current flowing in the coils.
- A suitable shielding material for NMR coils should possess high conductive properties, low permeability, and be thick enough to avoid skin depth effects.

2.4.2 Shimming of multiple neighbouring samples

Sufficient homogeneity of the B_0 field ensures NMR accuracy, particularly in terms of spectral resolution, and for a sufficient SNR for detection. However, the magnetic field inside the magnet is inevitably compromised by imperfections in the system components. These include coil windings, strain caused by temperature differences. Moreover, components are assembled from various materials whose magnetic susceptibility properties cause local field variations and tend to broaden the resulting spectrum [45, 46]. The operation of a regular shim set in the magnet is unable to compensate for the imperfections caused by a dense detector array, since its orthogonal decomposition would require excessively high orders of coils. Another crucial challenge results from how current shim systems are designed. Their design is typically based on spherical harmonic (SH) functions, where field correction coils are used to decompose the correction field into several shim sets. The following paragraph will outline the basic concept of shim coil design. Moreover, it will describe the issue that occurs when two or multiple samples must be shimmed at the same time and provide some possible solutions.

SH shim coil

Based on the fundamental theory of magnetostatic [47], the equation governing the production of static magnetic fields in a given space like magnet bore is as follows:

$$\nabla^2 B_0 = 0 \tag{2.19}$$

Now, 2.19 will be referred to. Once the sample is positioned within the magnet, the distribution of the B_0 field across the sample is divided into multiple components. Essentially, the sample is conceptualized as a three-dimensional space comprising numerous voxels, each with a minute volume. When described in terms of spherical polar coordinates, the characteristics of the field is determined using an equation that can be expressed as follows [48]:

$$B_0 = \sum_{n=0}^{\infty} \sum_{m=0}^{n} C_{mn} \left(\frac{r}{a}\right)^n P_{nm}(\cos\theta) \cos[m(\phi - \psi_{nm})] \tag{2.20}$$

where the (r,θ,ϕ) is the spherical polar coordinates of P, and the term a is the radius of the magnet. The constants are ψ_{nm} and C_{mn}. The SHs are eigenfunctions of the Laplace operator with the associated Legendre polynomials P_{nm}. Given the field distortion of a sample, which could be the result of its magnetic susceptibility or the system imperfection, any field can be plotted in a full expansion of several SH terms, as seen in Eq. 2.20. In this equation, n means the order of the polynomial, and when $m = 0$ that assumes constant values in the same Z direction, using use the term of zonal harmonics. When $m \neq 0$, it's called tesseral harmonics. Fig. 2.7 demonstrates several SH functions plotted on a spherical surface, for a given n and m, ranging from 0 to 4.

$$\begin{aligned} B_0 &= C_{00}P_{00}(\cos\theta) \\ &+ C_{01}\left(\frac{r}{a}\right)P_{10}(\cos\theta) + C_{11}\left(\frac{r}{a}\right)P_{11}(\cos\theta)\cos[(\phi - \psi_{11})] \\ &+ ..... \end{aligned} \tag{2.21}$$

Through expansion, the magnetic field can be analyzed in terms of SH functions; each function is orthogonal to the others. In theory, it is possible to devise a shim coil set in which each unit represents a distinct SH function. Such a set would permit the independent adjustment of individual coils without interaction with the remaining terms. This concept might significantly reduce the time allocated, an aspect that especially favors the FID-based shim approach. However, practical applications often involve samples used in chemistry or physics that are typically in cylindrical sample carriers, capillaries, or tubes for ease of handling. Additionally, the manufacturing imperfections of coils make it nearly impractical to achieve completely orthogonal shims.

To address the issue of B_0 inhomogeneity, commercial methods employ a series of shimming components modeled on the SH function. Despite the availability of other non-orthogonal shim systems [49, 50], SH coils remain the most widely used type of shim system. Each shim is designed to represent a specific SH function, ranging from first to fourth or higher orders for the zonal axis and on the plane (X-Y). As a result, current magnets incorporate a significant number of shim coils, with a typical NMR spectroscopy magnet containing over 20 shims. Fig. 2.8 provides a concise illustration of a SH shim set, including Z1, Z2, and X shims that may be stacked. It is worth noting that these shims generate correcting fields that are either symmetrical or asymmetrical to the center of the region of interest.

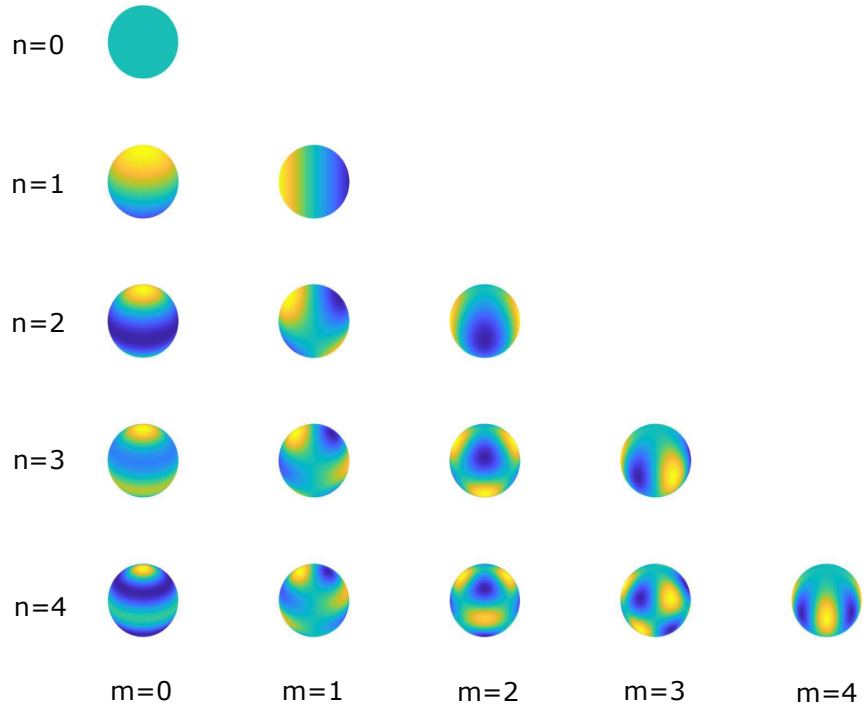

Figure 2.7: Ideal SH function plot on a spherical surface. n and m range from 0 to 4.

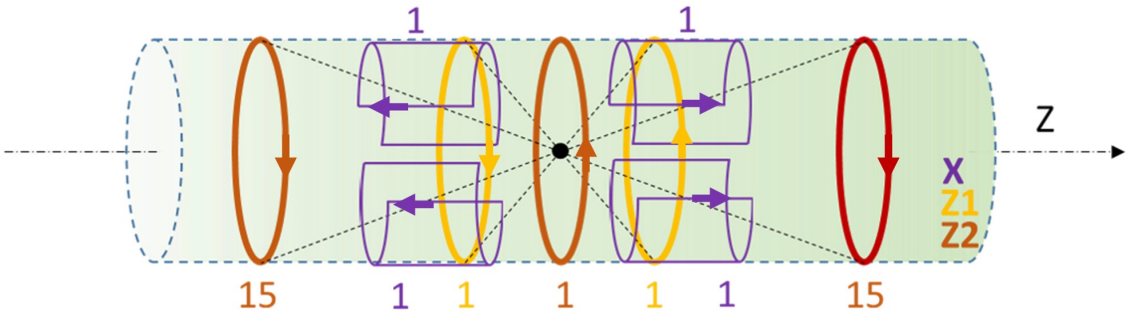

Figure 2.8: An example for the design of SH shim coils on a cylindrical surface, including Z1, Z2, and X. The number represents the number of turns of the coil. The figure is reproduced from Fig. 4 and Fig. 8 in [51].

Spatial field distortion

The main issue with the SH shim design is that each shim corrects the field based on the same single origin of coordinates. Therefore, this profile causes problems when attempting to shim two samples simultaneously. Suppose two identical samples with different magnetic susceptibilities (S1 and S2) are located within a homogeneous magnetic field with S_{air} surroundings, as shown in Fig. 2.9a. The ideal case is when two samples experience the same field distortion, i.e. the B_0 field in both the two samples on the cross-sectional plane is linearly distorted in the same direction with the same strength of

B_0. Additionally, the longitudinal section also follows the same second-order distribution. In such a scenario, a single global linear shim (X shim) could produce a correction field (B_0') to tackle all the on-plan distortions. Moreover, a global zonal shim configuration might be able to correct both fields, provided that the orthogonality and non-ideal spherical shape of the shim coils are not considered. Such a scenario might be attainable with proper placement of all probe elements, for example, in a symmetrical arrangement. However, most of the shimming coils in the commercial magnet are designed to have an optimized shim setting on the center of the isocenter. For two samples, this results in their inevitably being placed off-center and not in a symmetrical-spherical arrangement.

In most cases, ensuring that each sample experiences the same static magnetic field is challenging. Differences in magnetic susceptibility between the samples, the presence of nearby objects, or any geometric variations between the samples can cause the field profiles to differ. Fig. 2.9b illustrates a situation in which two samples display different field distortions on all X, Y, and Z axes. A specific global shimming field would be required to correct the fields in both samples, and it is unlikely to follow the SH distribution used in most current magnets. Therefore, it is nearly impossible to shim on two samples using a single shimming set.

Spatial field correction

Given the problems and limitations of the hardware, the need to shim on multiple samples for NMR parallelism is crucial. Therefore, a method must meet the following requirements: First, the correction field must be adjustable due to the variety of samples that cover a certain range of variance to magnetic susceptibility. Second, the correction field should be generated in an arbitrary shape that can take most of the B_0 inhomogeneity to meet the spectroscopy requirement. Third, the method can shim on two samples or more at the same time without interference with the other components, such as RF coils.

Based on the listed requirements, some field correction methods from the literature are referred. Also, a detailed discussion regarding the pros and cons of each technique is provided. In general, the broad classifications of shimming techniques can be divided into two types: passive and active methods.

The passive approach involves using a material that can undergo passive perturbation with the main magnetic field through magnetization to achieve a uniform field. These materials can be either paramagnetic or diamagnetic, resulting in different correction profiles. Passive shimming elements are designed based on a numerical estimation of

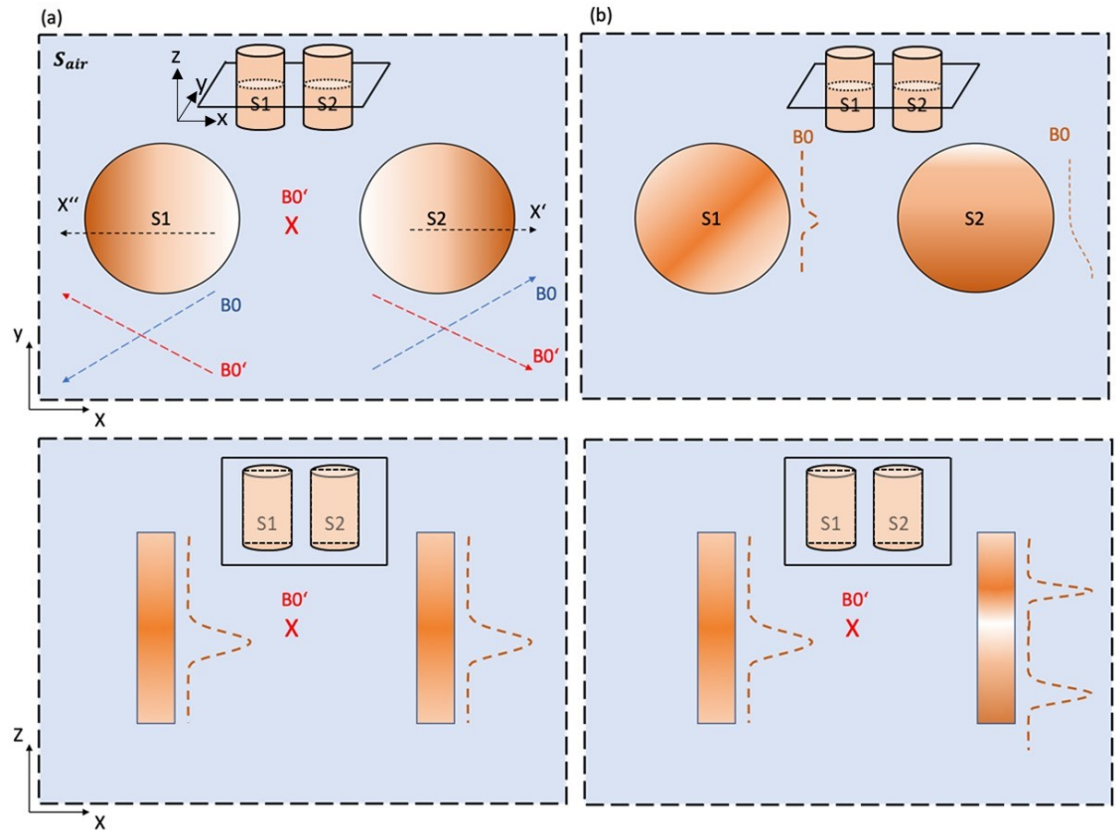

Figure 2.9: (a) An ideal case showing two cylindrical samples (S1 and S2) placed in the isocenter of a magnet exhibiting an identical field B_0 profile. (b) A real-life case showing two different field profiles. Note that B_0 stands for the field profile and B_0' stands for the necessary field to correct the inhomogeneity. (Upper figures: cross-sectional X-Y plane, Lower figures: cross-sectional X-Z plane)

the B_0 distribution in the target area. This method involves assigning specific materials and geometries to the shimming elements and positioning them appropriately in a regime where they can effectively correct the field. Typically, this concept is employed in magnet manufacturing to effectively reduce distortion levels, allowing the shim coil to address the remaining inhomogeneity.

The passive shim can also perform locally. Several studies have utilized shimming materials in human medical applications to improve MRI image resolution. Wilson et al. [52] used a mouth shim made from pyrolytic graphite to shim on the inferior frontal cortex. Cusack et al. [53] further evaluated this method using gradient echo planar imaging (EPI). Koch et al. [54] demonstrated that a two-metal approach can potentially address higher-order spatial fields in vivo. Neufeld et al. [55] demonstrated a distortion shift method that used a susceptibility-matched envelope for brain imaging. Passive shims can also be adjustable. Yang et al. [56] built a shim assembly composed of movable substructures for the shimming of the human brain in vivo (seen in Fig. 2.10b). Passive shim can be utilized

in NMR spectroscopy. Ryan et al. [57] demonstrated a lab-on-chip device with integrated structure shimming (Fig. 2.10d).

However, these methods are unfavorable for NMR parallelism due to the following disadvantages of passive shimming:

- Passive shimming necessitates positioning near the sample with very high accuracy, requiring an extensively integrated design tailored to specific sample geometries and is generally not applicable to different dimensions.
- The magnetic susceptibility of the shimming material can be affected by temperature variations in the environment.
- Passive shimming usually targets larger susceptibility mismatches, as in human body imaging. Even though the shim structure can be potentially miniaturized to microscale, removing distortions would require a complicated design.

The active method employs current-carrying loops to reconstruct the field. The advantage of active shimming is that the currents, hence the shimming field, can be adjusted easily for optimal results. Active shimming is on a subject-specific basis. For example, Hsu [58] introduced a concept to locally homogenize the magnetic field in the interior portion of the frontal lobe, where the field is most seriously distorted, by placing resistive shim coils (Fig. 2.10a) in patient's mouth. In this application, the sample-induced inhomogeneities were too large, so the global shim set was unable to correct the distortions.

This subject-specific active shimming has been further utilized in NMR spectroscopy. Van et al. [59] proposed a shim-on-chip design that integrates the shim coil with RF coils to reach a 2 Hz linewidth (Fig. 2.10c). They found that the parallel current lines produce high-order zonal functions. Moreover, the shim-on-chip method requires far less space, demonstrating the potential of the NMR coil array. Considering the advantages outlined for the Shim-on-chip technique, this concept is adapted to create an integrated NMR cell (NC) based array. The detailed design and results will be presented in Chap. 3 and Chap. 6.

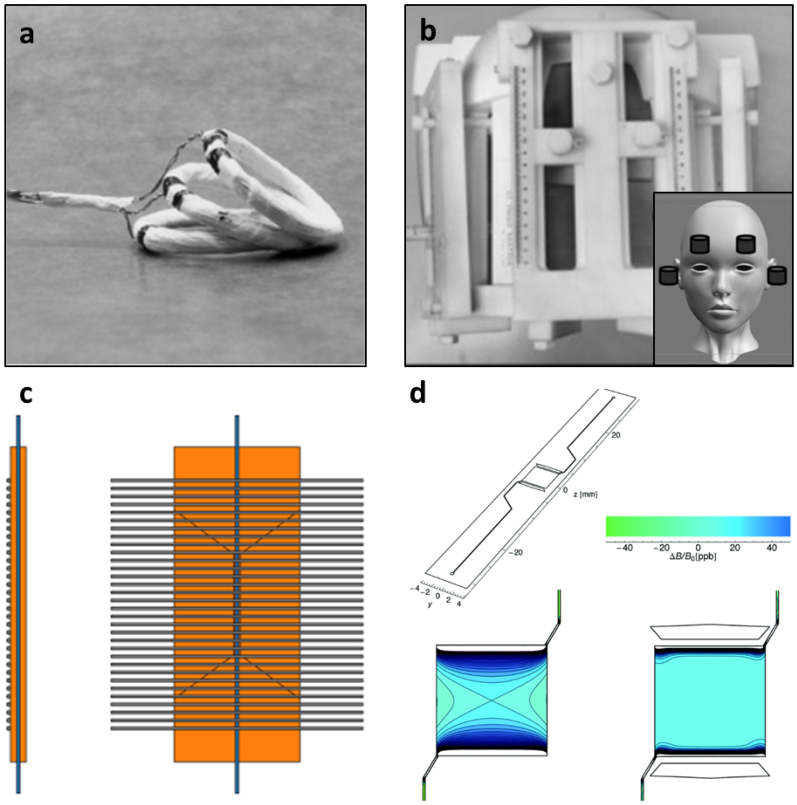

Figure 2.10: (a) A active local oral shim coil, reprinted from [58] with permission from John Wiley & Sons Inc. (Copyright © 2005 Wiley-Liss, Inc.) (b) A passive shim-assembled head mount for frontal lobes, reprinted from [56] with permission from Elsevier Inc. (Copyright © 2011 Elsevier Inc.) (c) Shim-on-chip design for high-resolution NMR spectroscopy, reprinted from [59] with permission from American Chemical Society (Copyright © 2018 American Chemical Society) (d) Passive shimming for lab on chip device using air-filled compensation structures, reprinted from [57]. (Copyright © The Royal Society of Chemistry 2014)

3 Sample-centred shimming enables parallel NMR detection

The contents of this chapter are based on the author's contribution to the material published in the article [J1]. **Material from: Cheng, Yen-Tse et al., Sample-centred shimming enables independent parallel nmr detection, Scientific Reports, published [2022], [Springer Nature]**

In this chapter, a comprehensive study is provided of the design, characterization, and manufacturing of a low-field parallel NMR probehead. Several important aspects are addressed in this chapter. First, the chapter proposed a new concept of NC extending the road toward parallel NMR hardware design. This idea is based on an integration of a shim coil and an RF coil. Parallelizing NMR spectroscopy at the low field is accomplished through two identical NCs. Second, the challenges encountered including the RF coupling when two NCs transmit and receive at the same frequency, during the parallel experiment. We explore several decoupling methods and implement a geometrical decoupling method in our custom-built probehead.

The chapter is divided into several sections. Section 3.1 provides a detailed introduction of the technical aspects and design constraints for the parallel NMR system at low field and state-of-art of hardware design which can be potentially a good candidate and be adapted into a custom-built parallel system. In Section 3.2, owing to the simultaneous transmission and reception of radio waves at the same frequency enables faster acquisition, while the cross-talk needs to be mitigated to ensure accurate detection. Here, we explore the removal of coupling from the front-end arrangement of the array and provide the finite element (FEM) simulation and experimental results. Furthermore, this chapter delves into the perspectives on shimming issues associated with six shims within an array. Finally, we demonstrated the parallel spectroscopy in two NCs.

3.1 Introduction

Magnetic resonance spectroscopy (MRS) enables the robust characterization of organic and inorganic chemical samples whose spin populations are aligned by a strong and uniform B_0 magnetic field. The evolution of the spin population state is initiated by a RF excitation pulse, and after a period of manipulation and evolution, its time-dependent response is recorded at high resolution [60–64]. Conventional NMR is primarily conducted in a time-inefficient sequence that can include one or more of the following steps: sample loading, coil tuning and matching, B_0 field shimming to an acceptable B_0 distortion level, and radiofrequency (RF) excitation and reception at the target NMR frequencies and the long recovery times that restrict the speed of acquisition. Altogether the operations are time-consuming and reduce sample throughput. Current approaches from a hardware perspective, to boost up experimental speed and address the low throughput problem in current magnet systems, include automated sample loading ([27, 65, 66]), multinuclear RF detectors[67–69], and automated tune and match systems[70, 71]. For instance, an automated flow-through system integrated with liquid sample sensing has proven that a large batch of sequential fluidic samples can be handled, each within 2.4 s, with sufficiently high NMR resolution[27]. Broadband detectors were utilized to simultaneously acquire multiculear NMR spectra without further tuning and matching, or switching of coil topology. Despite these significant technical advances in high throughput NMR, the cumbersome procedure of a typical sequential measurement still limits current NMR measurements, which motivates us to explore parallel spectroscopy.

Inspired by the idea of a parallel MRI array [38, 72–75], we aim to perform NMR spectroscopy in a coil array. [11, 76] True parallelisation of detection would dramatically reduce acquisition time, but would require a dense array of decoupled RF detection coils [38, 74] The phased array imaging coil is a successful multiple-detector technology [11, 38, 74] that employs coil overlap, embedded preamplification, and spatial orthogonality of the detected signal distributions. This promotes decoupling and hence good spatial localisation of the spin signals, yet the technique does not decouple sufficiently for spectroscopy, which is more demanding in terms of sensitivity to stray signals. Moreover, even though coupling can be suppressed in such technique, the sample is inevitably detected by two adjacent coils due to the overlap topology. Three main constraints currently limit the application of multiple closely spaced coils in NMR spectroscopy.

Previously proposed approaches [16, 77] for addressing the B_0 homogeneity of a coil array is through the filling intermediate space with a susceptibility matching material, or the utilization of multiple miniaturized coils. However, these approaches are limited when

susceptibility variations among samples are large, which make it nearly impossible to shim multiple samples to an optimal linewidth. For microcoils, the sample volume is also limited, which affects the SNR. Another method is motional averaging [17], achieved by rotating the sample along one axis to up to 60 Hz. However, an additional DC motor and gearbox are not favored in a high field magnet environment for two reasons: 1) DC motors are usually equipped with permanent magnets, or high susceptibility materials, and non-magnetic motors rarely have enough power and compactness. 2) The extensional gearbox system makes the resulting probehead design complicated, since space is quite limited in the magnet bore.

Current technologies for decoupling adjacent coils include induced current compensation[78], capacitive and inductive decoupling networks[79, 80], self decoupled coils [81], all of which have proven to provide an acceptable decoupling value of ($< -20\,\mathrm{dB}$). However, the methods target planar surface coil arrays that allow either capacitors to be attached to the RF coil, or additional loops used to achieve coil overlapping structures [39]. These methods are not favored for spectroscopy for numerous reasons: 1) Surface coil arrays target the study of live animal and human subjects, and the detector size allows bulky capacitors to be attached, which limits the potential of miniaturization. 2) The topology of a surface coil is not ideal for spectroscopy, mainly in terms of B_1 field homogeneity. 3) Surface coils are usually single-looped, which limits their sensitivity. 4) Overlapped coils will detect each other's samples.

Therefore, considering the constraints of previous methods, here we explore the idea of localized shim coils for a parallel detector system. In our case, localized shimming would achieve two advantages: 1) allowing simultaneous B_0 field correction at multiple positions, and 2) introducing the ability to correct strong field inhomogeneities, since the shim coils are spatially closer to the sample. For the suppression of signal coupling, we explore the geometrical decoupling technique, without interfacing with the RF coil, in order to mitigate spectral coupling.

3.2 Geometrical considerations for RF decoupling

In a parallel NMR system for the same nuclei, radio waves have to transmit and receive simultaneously at the same frequency at the same time, providing faster acquisition than in a single coil system. However, in order to design such a system, it is essential to mitigate the cross-talk due to simultaneous transmission and reception, which seriously limits the accuracy of detection as described in Sec. 2.4.1. Considering the method is mostly designed for surface coils, we investigate the removal of coupling from the front-end arrangement of the array, without interfering with any complex decoupling circuit.

Current NMR spectroscopy employs various types of RF coils, with the most commonly used being solenoid, saddle, and stripline resonators. Each of them produces distinct RF field profile. The presence of different RF fields also affects the implementation of suitable decoupling schemes for specific coil geometries. Therefore, it is difficult to find the same method to mitigate the stray fields for different coil topologies. For example, the overlapping method is generally not applicable to the saddle and stripline coils. Given this reason, in this chapter, we simulated some straightforward decoupling methods that is suitable for three commonly used coil geometries: solenoid, stripline, and saddle coil.

Solenoid coil: Faraday shielding

The most common and used coil found is definitely, a solenoid coil. It is not only easily fabricated but also found to have high SNR and low detection limits. The geometry of a solenoid coil typically consists of a cylindrical shape, with the metal wire wound tightly around a core material.

Here, we examined the Faraday shielding method in the solenoid coil to block the transmission of the RF field, since it is the most straightforward decoupling method for solenoid topology. Here a 2 mm OD air core solenoid with 10 windings was simulated at 45 MHz under the RF module in COMSOL multiphysics. Three cases are put into our comparison: a 6 mm OD copper shielding (thickness=0.2 mm, considering the skin depth=9.7 µm), 2 mm OD copper shielding, and a bare solenoid. To visually observe the significant improvement due to the field cancellation, contour plots of the normalized B_1 in the central plane (y = 0) of the shielded solenoid and unshielded is shown in Fig. 3.1. The shielding structure is clearly observed to effectively eliminate lateral stray fields on the X-Y plane, confining the field within the shielding element. Notably, we observed that the field cancellation remains unaffected by the distance between the coil and the shielding elements. However, as the

diameter of the copper shielding decreases from 6 mm to 4 mm OD, the central B_1 field is reduced by 10 %. This reduction corresponds to a 10 % loss in SNR, based on the NMR SNR formula, underscoring the importance of selecting an appropriate diameter for the copper shielding.

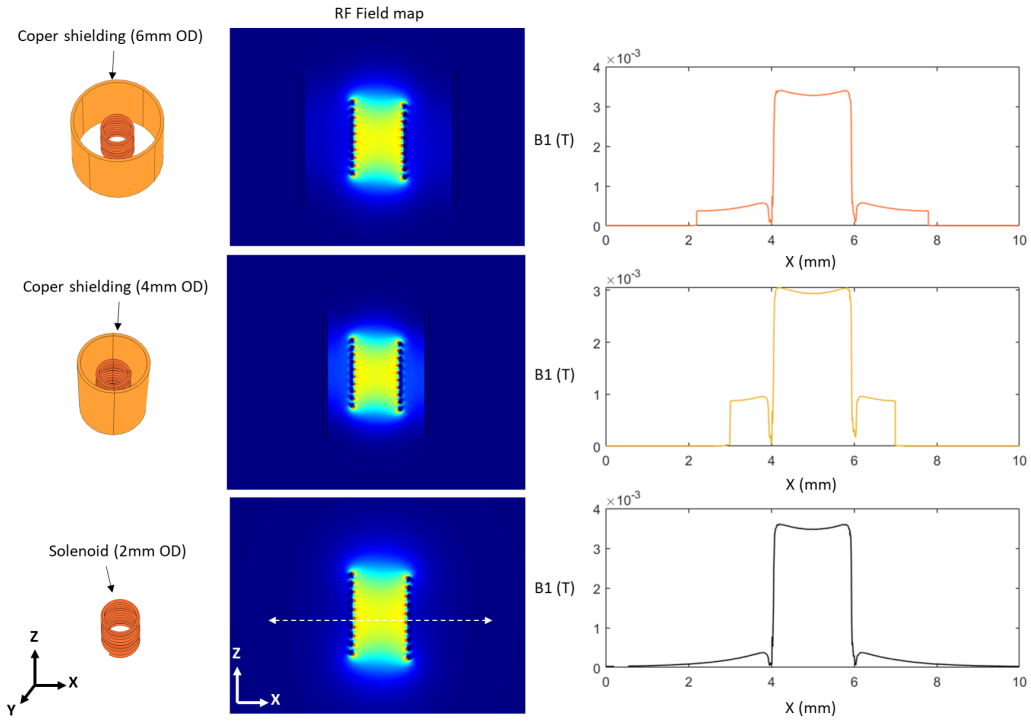

Figure 3.1: Three cases of a solenoid coil within a copper shielding wall (4mm or 6mm) and without shielding for signal isolation. The contour plot of the RF field at the X-Z cross-sectional plane and the field distribution along the X direction in the center of solenoids were simulated under FEM simulation.

Stripline coil: Self-shielding

The electromagnetic shielding has been discussed and examined in the solenoid coil in the previous paragraph, showing the stray field outside of the sensitive regime can be canceled by introducing copper shielding. Such a mechanism can be seen on a conventional microwave circuit board that utilizes a microstrip or stripline transmission line to guide RF energy and is isolated by either one or two ground planes. The first utilization of stripline in NMR spectroscopy was presented by Bentum [29], showing the stripline performs well as NMR sensor in terms of resolution (0.01 ppm) and sensitivity (1×10^{12} spins per $\sqrt{Hz}$). This stripline detects spin signals from a center bone-shaped transmission line sandwiched within a dielectric material between one or two outer ground planes.

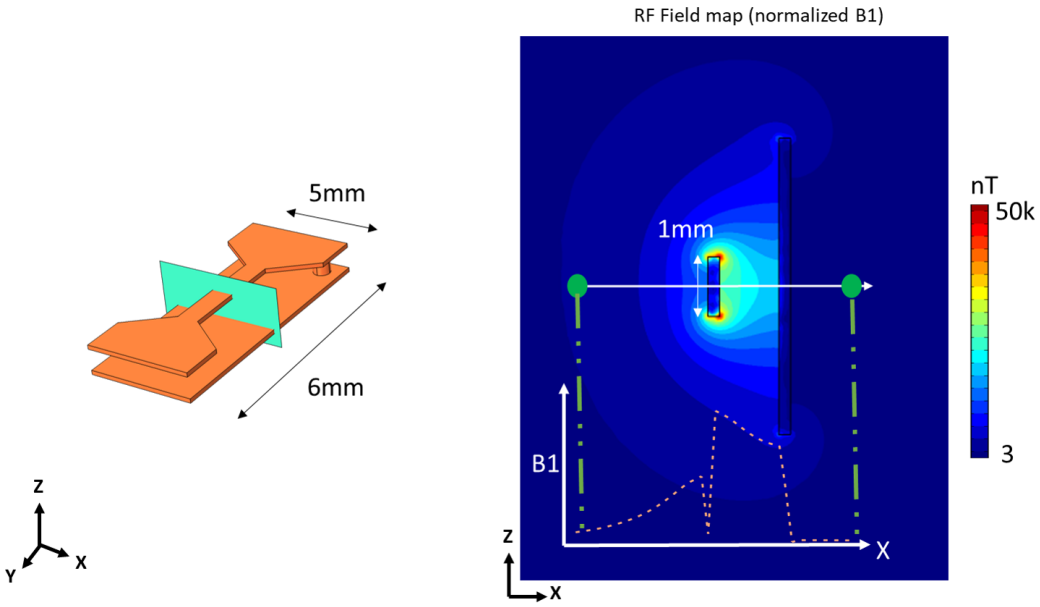

Figure 3.2: CAD model of a stripline/microstrip coil for RF simulation. The contour plot of the RF field at the X-Z cross-sectional plane and the field distribution along the X direction in the center of the stripline.

For communication, the advantage of this geometry is the good confinement of the transmission signal since the electromagnetic radiation is entirely enclosed within a homogeneous dielectric material. While there's limited literature discussing the shielding effectiveness of stripline at NMR bandwidth. Here we perform a FEM simulation for a typical microstrip coil at 45 MHz to estimate how strong B_1 suppression is with the introduction of shielding ground. As seen in Fig. 3.2, the bottom metal plane is closely placed to the transmission line on one side, connected with two vias. Nonetheless, it indicates a strong fall-off B_1 field behind the shielding plane, while at the opposite face, B_1 is gradually and slowly decaying. Based on the shielding effectiveness formula 2.18, comparing the B_1 observed at the same x distance ($\pm$2mm) to the strip, the shielding material provides 53 dB of shielding effectiveness.

Saddle coil: Geometrical decoupling

Based on the definition of Faraday law of induction for magnetic coupling, as seen in Eq. 2.16, the induced electromotive force in one loop coil is correlated to the rate of magnetic flux generated by the other coils. In the case of two orthogonal coils, which generate magnetic fields that are perpendicular to each other, the induced EMF in each

coil is proportional to the rate of change of the magnetic flux through that coil. If the magnetic field is changing only along one axis, say the X-axis, then the EMF induced in the coil along the X-axis will be nonzero, while that in the coil along the Y-axis will be zero ($B_2 \cdot dA_1 = 0$). This orthogonality sounds promising for mitigating the magnetic flux coupling within two coils. While such an arrangement is not suitable for saddle coils, since the coils will be concentric, it only applies to an array of two coils. Even though this orthogonality can still be modified, in the following, we investigate a misaligned method for a dual-saddle coil array.

To evaluate how the geometrical misalignment of two adjacent unloaded coils contributes to the mitigation of cross-coupling, we simulated and measured the scattering parameter set S_{12} for different angles of rotation (θ_1 and θ_2) of each coil (NC1 and NC2) respectively. Based on the Biot-Savart law and Faraday's law of induction , as the coil-to-coil distance $\mathbf{r}'$ is decreased, the coupling will increase significantly. We fixed the inter-coil separation to 35 mm, so that the result would only take the B_1-misalignment into account. The simulation result is shown in Fig. 3.3a, indicating a reduction of S_{12} to -100 dB when $0^\circ \leq \theta_2 \leq 90^\circ$ is varied while θ_1 is fixed at 0° (blue curve). Setting θ_1 to 90°, and again varying $0^\circ \leq \theta_2 \leq 90^\circ$, we see that S_{12} reaches a maximum of -80 dB (green curve). A dip at 10° is contributed by the slightly imperfect magnetic dipole field of the saddle geometry. The result indicates a strong suppression of signal coupling (23 dB) owing to the integrated projection of the RF field of coil 1 onto the sensitive volume of coil 2 induces minimal current when both coils field vectors are orthogonal.

Although the simulation here considered coils without tuning and matching circuitry, geometrical decoupling is independent of the circuits that are interfaced with the coils. Orthogonal misalignment can nevertheless greatly reduce the magnetic flux coupling. We thus fixed the relative orientation to 90°, tuned both resonators to 45 MHz, and matched them to 50 Ω, obtaining less than -20 dB of reflected energy (S_{11}, S_{22}) and -30 dB of coupling (S_{12}) using a network analyzer, as presented in Fig. 3.3b. For loaded coils, a plot of the measured S_{12}-parameters as a function of θ_2 is shown in Fig. 3.3c. As expected, the parallel coils have higher coupling than for the misaligned case, with a transmission coefficient S_{12} of -21.2 dB going down to almost -30 dB, as was found for the unloaded simulation result. We found that this is the most straightforward decoupling method for an array of coils without extensive circuit design or an additional shielding layer.

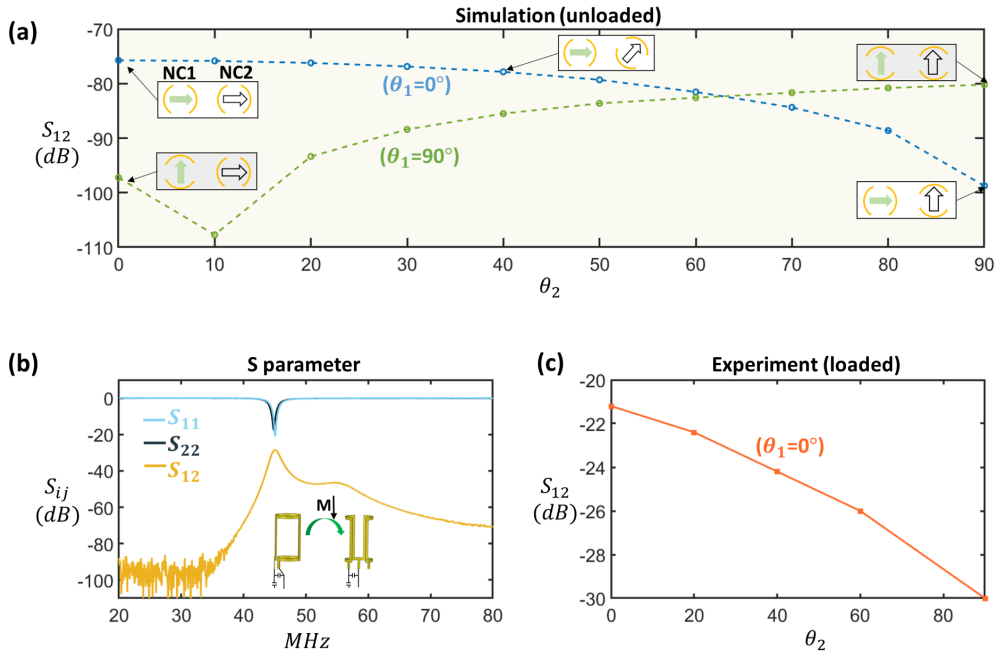

Figure 3.3: (a)Simulated coupling coefficients for two saddle coils resonating at 45MHz, for a range of misalignment angles obtained by rotating NC2 (Blue: Coil NC1 is fixed at 0°. Green: Coil NC1 is fixed at 90°).(b) Measured scattering parameters S_{11}, S_{22}, and S_{12} versus frequency for NC1 and NC2, while employing the proposed geometrical decoupled technique. Both NCs are tuned to 45 MHz and matched to 50 Ω. (c) Loaded coupling coefficients S_{12} measured between NC1 and NC2 for different misalignment angles. Coil NC1 is fixed at 0°.

3.3 Implementation of first-order local shim coils

Commercial NMR magnet systems are typically designed such that they have a single RF coil, and more significantly, a single shim set, thus allowing the measurement of a single sample at a time. Shim systems in commercial magnets are based on the concept of co-located spherical harmonics, and therefore their functions are guaranteed to be orthogonal only relative to a single coordinate origin, and only to some extent. Here considering limitations, we aim to create localized SH shim coils for each RF coil to tackle the spatial field distortion. We targeted a low field 1.05T MRI magnet that is only equipped with global liner shims for prof-of-concept.

As given in [51], the spherical harmonic shims are constructed on a cylindrical surface, which can be easily adapted in our design. When designing a local shim coil for two NCs, we take into account the stray field generated by the NC shim coil and determine the shim capacity. The former static interference should be minimized to avoid higher-order components of distortion. The latter should be high enough to avoid being driven by a high

current. For the spatial variation present, the required strength required for shimming was found to be in the range of few hundred Hz cm^{-1}, as seen from the shim values recorded in Fig. 3.8a.

Subsequently, we proceed as follows:

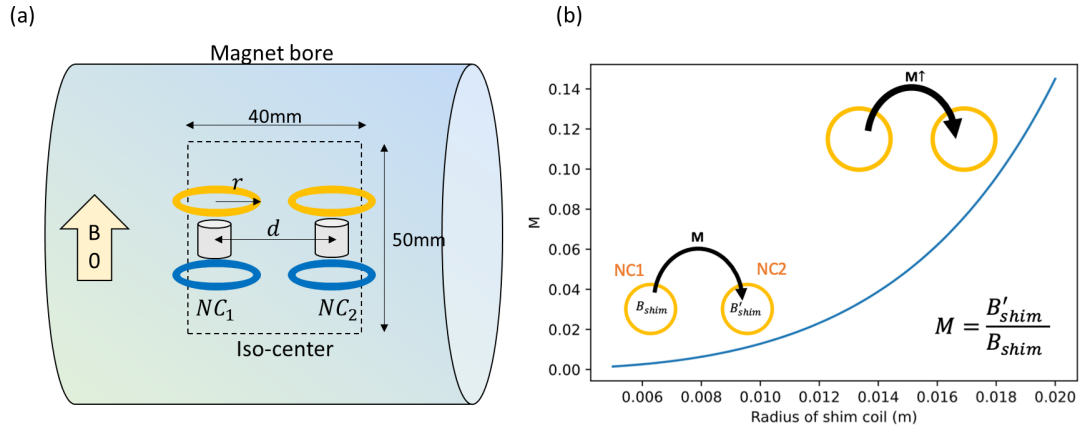

Figure 3.4: (a) Schematic illustration of the magnet bore and geometry design consideration for two NCs, i.e. $d < 40mm, r < 20mm$ (b) Calculated stray field coupling between two circular loop coils with a range of radii based on Biot–Savart law. (M defines the static field coupling coefficient. B_{shim} is the maximum shimming field on the sample of NC1. B'_{shim} is the shimming field on the center of NC2.)

- The homogeneous region (iso-center) of the magnet bore is 50 mm(OD)x40 mm(L). A schematic can be seen in Fig. 3.4a. Therefore, considering the limited distance for placing two NCs and two samples, the distance (d) was set at 35 mm to reduce the stress of RF/DC coupling.

- We measured the linewidth from two samples in two NCs to determine how strong the local shim field is required for two NCs. And, as shown in Fig. 3.8, the shim capacity of each NC shim must be greater than 400 Hz cm^{-1} to correct the spatial inhomogeneity.

- The topology design of the NC shim coil was based on the spherical harmonic correcting coils (x,y,z) as provided by Romeo et al.[51] on a cylindrical surface.

- The diameter of the NC shim coil is our design consideration: Because the shim is placed in very close proximity to the sample, a small diameter shim coil can provide a larger shim capacity. However, it will also generate a counterfield, lowering the SNR of the RF coil. And unwanted noise would couple from the NC shims since they are not optimally shielded. When the diameter of the shim coil increases, where

the shim coil is reaching the other shim, i.e., 0.02m, the stray field coupling reaches 14%.

- Therefore, We estimated the stray shim field coupling between two NC shims through Biot–Savart law. The Biot–Savart law approximation is based on a circular current loop for a range of radii with 35mm inter-coil separation.

- Based on Biot–Savart law the stray field leaking in-between two NCs for a range of radii has been estimated, as shown in Fig 3.4b. Therefore, a reasonable value (8.5 mm) for the radius of the shim was selected as it only allows around ($M =$ 1 % to 3 %) stray field coupling for each shim.

Linear shim design on cylindrical sample

To visualize the correcting profile (B_z') generated from linear X, Y, and Z shims, the shim designs were created on FEM field computations using a commercial solver (COMSOL Multiphysics 5.4, AC/DC module, COMSOL AB, Sweden). The ROI is discretized using a relatively denser mesh with around 100K mesh elements and the shim coils are discretized with a regular mesh size, as seen in Fig. 3.5a and Fig. 3.6a. In the simulation, the value of the current was set to 100 mA. Fig. 3.5b and Fig. 3.6b report the simulated shimming profiles. The simulated result of linearity and shim capacity shows the ability to remove the remaining inhomogeneity (> 300 Hz) with reasonable current intensity.

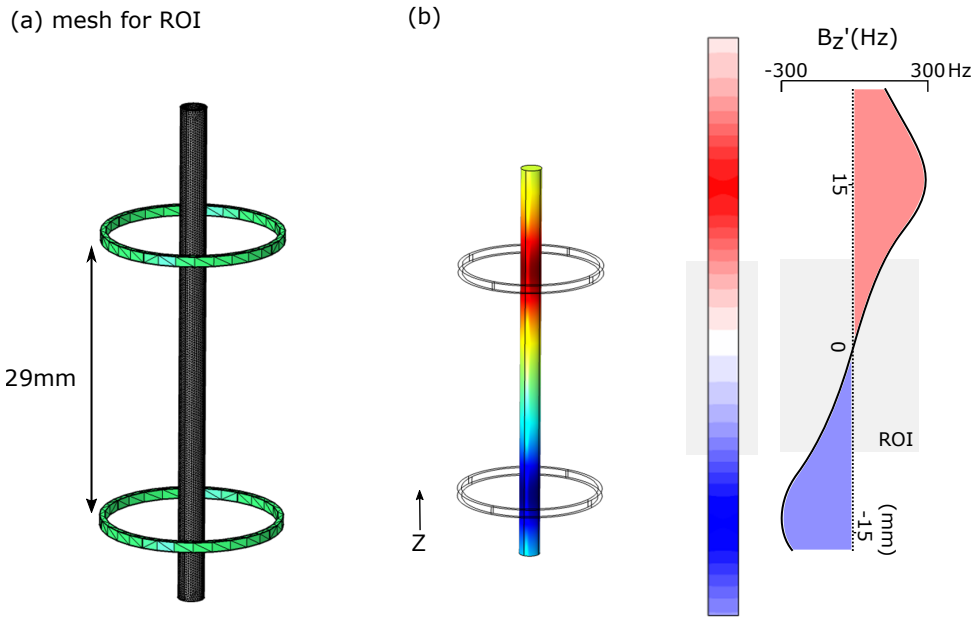

Figure 3.5: (a) Mesh for ROI and the local shim coil Z. (b) Correcting magnetic field B_z' generated by Z shim coil on the Y=0 plane. The field strength is translated to the proton frequency of 45 MHz, based on the gyromagnetic ratio. (note: current setting: 100 mA)

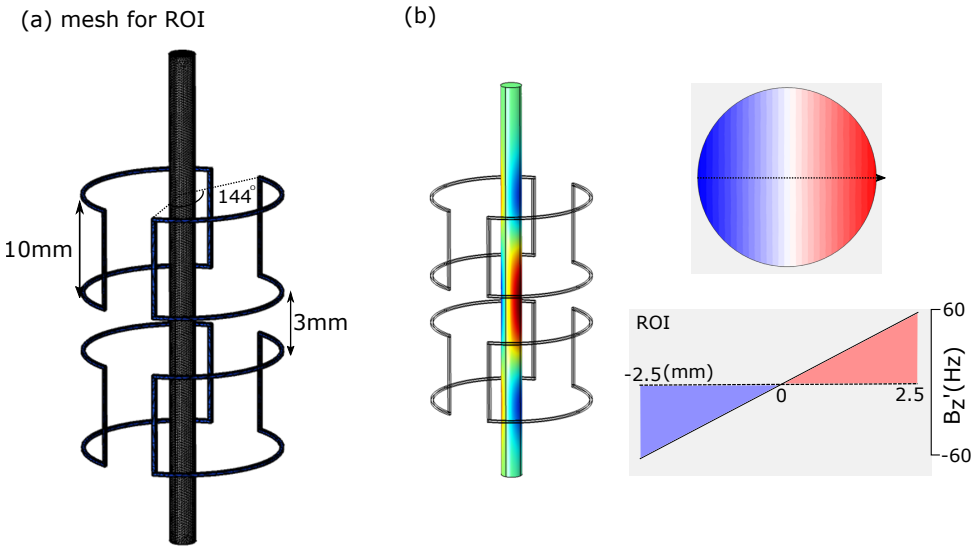

Figure 3.6: (a) Mesh for ROI and the local shim coil(X,Y). (b) Correcting magnetic field B_z' generated by X,Y shim coils on the Z=0 plane. The field strength is translated to the frequency, based on the gyromagnetic ratio. (note: current setting: 100 mA)

3.4 System design of shim-integrated NMR detectors in parallel

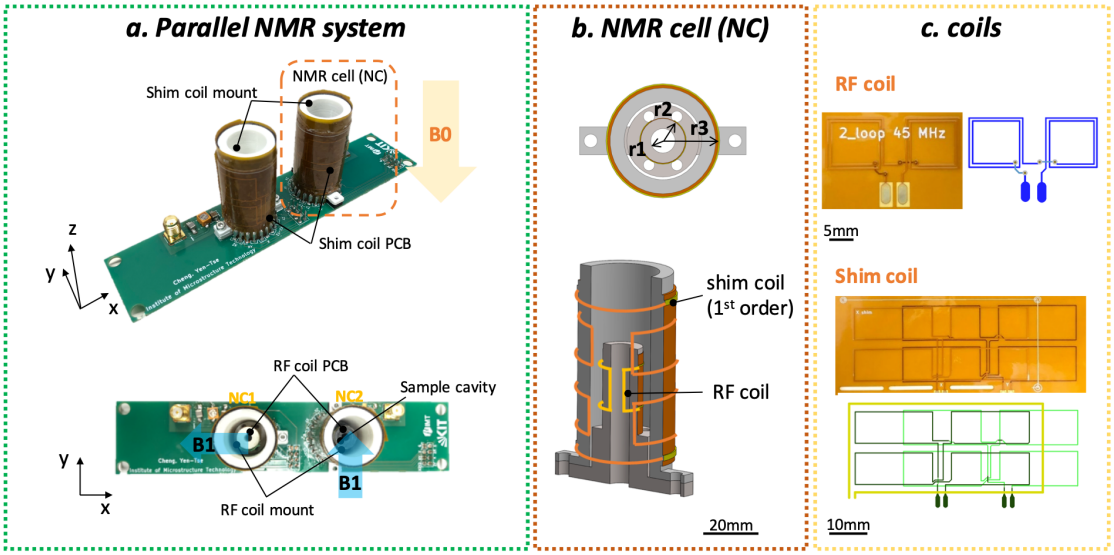

Figure 3.7: (a) Photograph of the proposed parallel system, featuring two NCs mounted on a PCB. (b) CAD model of a single NC, featuring a 3D printed holder for the RF signal detection coil and a circular capillary, and a set of miniaturized shim coils surrounding the detection site ($r_1 = 2.5\,\text{mm}$, $r_2 = 4\,\text{mm}$, $r_3 = 8.5\,\text{mm}$.) (c) Photograph and schematic of a flexible substrate RF coil PCB, and a shim coil stack PCB, prior to wrapping the PCBs onto the support.

Here, we propose a parallel NMR system for a 1.05 T field magnet, capable of spatial field correction enabling individual and simultaneous NMR detection. Fig.3.7a demonstrates a parallel NMR system built from a highly integrated NC as a standalone NMR sensing unit, and conservatively expands the number of units to achieve moderate parallelism. Each NC is composed of an RF coil, for NMR signal excitation and reception, and a set of local shim coils for spatial static field correction. The directions of the B_1 vectors generated by each NC are orthogonal to each other to mitigate magnetic flux coupling. The schematic of the unit NC is shown in Fig. 3.7b. Both shim coil sets and RF coils are made using flexible printed circuit board technology (Fig. 3.7c) and are rolled up around 3D-printed PLA-based supports. The sample holder is made for an $r_1 = 2.5\,\text{mm}$ radius glass tube that is used as a sample holder. A saddle coil with a radius of $r_2 = 4\,\text{mm}$ was utilized as the RF NMR detector. The shim coils were wrapped around the outer support which has a radius of $r_3 = 8.5\,\text{mm}$. The RF coil is based on the Ginsberg et al.[22], presenting the optimal geometry of saddle coil for producing a uniform magnetic field.

The localization of the shim coil sets thus divides the regular isocenter of the magnet into multiple, sample-defined isocenters, allowing for local and separate field correction. The

technical advantage of a local shim system mainly lies in the independent operation of these orthogonal spherical harmonic coil fields when constructing the desired correction profile.

3.5 Parallel shimming strategy

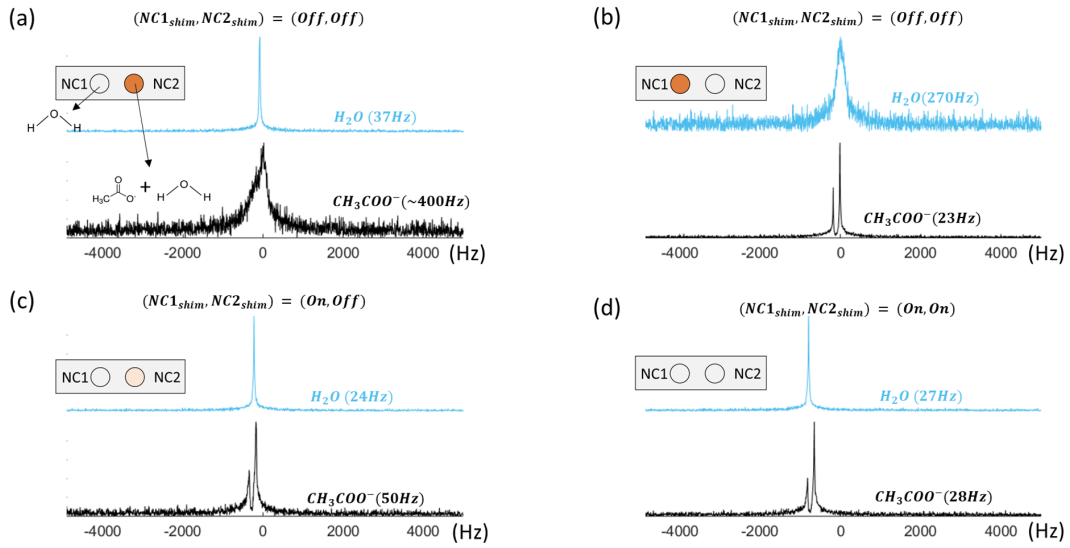

Figure 3.8: NMR experiment using the probehead to observe required shimming value and procedure for achieving shimming on two NCs. (a) Stage 1: regular shimming on NC1 with strength of $\mathrm{Hz\,cm^{-1}}$ $(111, 194, 434)$ (b) Stage 2: regular shimming on NC2 with strength (-313,216,189). (c) Stage 3: use the intermediate regular shimming value (-200,194,250) and turn on local shim of NC1. (d) Stage 4: turn on both local shim. (Note that the color of the circle is used to indicate the inhomogeneity of the B_0 field: deep orange > light orange > gray)

In order to find a proper shimming set which is compatible with the regular shim set of the 1.05 T magnet (ICON, Bruker), a localized shimming coil for each NC was designed as a truncated spherical harmonic set. Given the space provided at the isocenter of the magnet core, each shim coil's topology was determined using a finite element solver (COMSOL).

The regular shim coil is able to reduce general inhomogeneities to within the μT range. The diameter of the dedicated shim coil was chosen to be $d_3 = 20\,\mathrm{mm}$, to ensure its ability to remove any remaining inhomogeneity with reasonable current intensity. This in turn determined the separation among NCs, since shimming coil fields should only minimally interfere with each other, resulting in an inter-NC separation of 35 mm. Thus each NC achieved a shimset coordinate origin within its own sample volume.

Figure 3.8 depicts the result of shimming operations for the dual NC probehead employed using a series of single pulse experiments. For this experiment, NC1 contained pure distilled water, and NC2 contained 50 % acetic acid in diluted water. To perform parallel field shimming in practice, all three sets of shims were employed: the NC1 and NC2 shimsets surrounding the detection sites, and the regular shimset as supplied by the manufacturer of the magnet. For each of the sets, we only considered the first order terms (X,Y,Z) in correcting the spatial B_0 field variation. The quality of the B_0 homogeneity was determined from the acquired NMR spectrum by monitoring its full-width half-maximum (FWHM). The shimming proceeds as follows:

- Stage 1: Based on the DI water sample in NC1, the regular shim settings were determined to have an (X,Y,Z) strength of $(111,194,434)$ Hz cm^{-1} to achieve a FWHM linewidth of 37 Hz. For these settings, NC2 delivered a noisy and broad spectrum, with a FWHM of 400 Hz, in which the Methyl group of the acetate sample was not discernible.

- Stage 2: The regular shim settings for NC2 were found to have an (X,Y,Z) strength of $(-313,216,189)$, to achieve a FWHM linewidth of 23 Hz, acquired on a ^{1}H peak of acetate, yet to have a FWHM linewidth of 270 Hz for the ^{1}H peak of the DI water sample in NC1.

- Based on these results, the regular shim settings were now set to the average of both experiments, i.e., an (X,Y,Z) strength of $(-200,194,250)$ Hz cm^{-1}, which represented a reasonable compromise for the entire sensitive volume.

- Stage 3: As shown in Fig. 3.8c, the NC1 shim was now turned on with a local coilset current of $(X,Z,Y) = (46.6,0.0,97.8)$ mA. This achieved 24 Hz of FWHM on the ^{1}H peak, while for NC2, a 50 Hz FWHM linewidth was obtained without applying any current to its shimset.

- Stage 4: In a final step, the NC2 shim was also turned on, with an (X,Y,Z) shimset current of $(2.9,0.7,23.6)$ mA, which for NC2 achieved a FWHM linewidth reduction to 28 Hz, but without affecting the narrowed linewidth of NC1.

3.6 Sychronized parallel NMR detection and experimental results

The parallel NMR experiment was carried out using a pre-clinical 1.05T cryogen-free MRI magnet system (Bruker Biospin, Ettlingen, Germany) together with a custom-built probe. The sample for each NC was prepared and inserted in the cavity as defined. The vendor-supplied ICON console is limited to single channel acquisition, during the synchronized NMR experiment, each of the two NCs was each connected to one of two separate electronic interfaces in parallel. One RF coil was connected to the ICON console and executed a single pulse experiment under the ParaVision software interface (version 6.0.1, Bruker). A second coil was connected to a low noise amplifier (ZX60-3018G-S+, Mini-Circuits) for RX, a power amplifier (ZHL-20W-13SW+, Mini-Circuits) for TX, and the resulting signal was processed by a lock-in amplifier (UHFLI, Zurich Instruments), operated via the vendor-supplied software (LabOne 17.06, Zurich Instruments). To ensure parallel synchronization, a TTL transmission line of the ICON system was connected to the lock-in amplifier to provide a trigger signal for excitation. Thus both coils were excited simultaneously. For spectral averaging, each repetition was triggered by the ICON's TTL trigger signal to ensure that, during each repetition, both coils were triggered at the same time. Multiple acquired spectra were post-processed, including peak shift adjustment and averaging.

The NC-based parallel system was assigned to detect ^{1}H nuclei in parallel. We investigated six different samples, arranged into three sets of experiments (each set considered two distinct samples). The aqueous samples utilized in our NMR characterization are not only common solvents that are widely used for biological processing, but also contain distinguishable peaks that help to reveal any cross coupling effects. NMR experiments were carried out at 45 MHz, corresponding to the ^{1}H frequency of a 1.05 T magnet. The results are shown in Fig. 3.9. Each spectrum presents a single scan, and the result of signal averaging enhanced SNR.

The parallel NMR acquisition of two samples is demonstrated in Fig. 3.9a from measurements of 1D ^{1}H spectra in samples contained in the two NC's. For each sample, 32 sequential scans in 32 s were carried out to increase the SNR in order to distinguish the NMR spectral peaks. Since the magnet displayed a few $\mathrm{Hz\,s^{-1}}$ of drift, the resulting spectra were post-processed with phase correction and spectral peak alignment after each scan (a frequency lock channel was not available). According to the chemical structure presented, both samples included H_2O which contributed to the water peak. We aligned the H_2O peaks as reference at 4.8 ppm, so that the final spectrum resolved the CH_3 and OH peaks

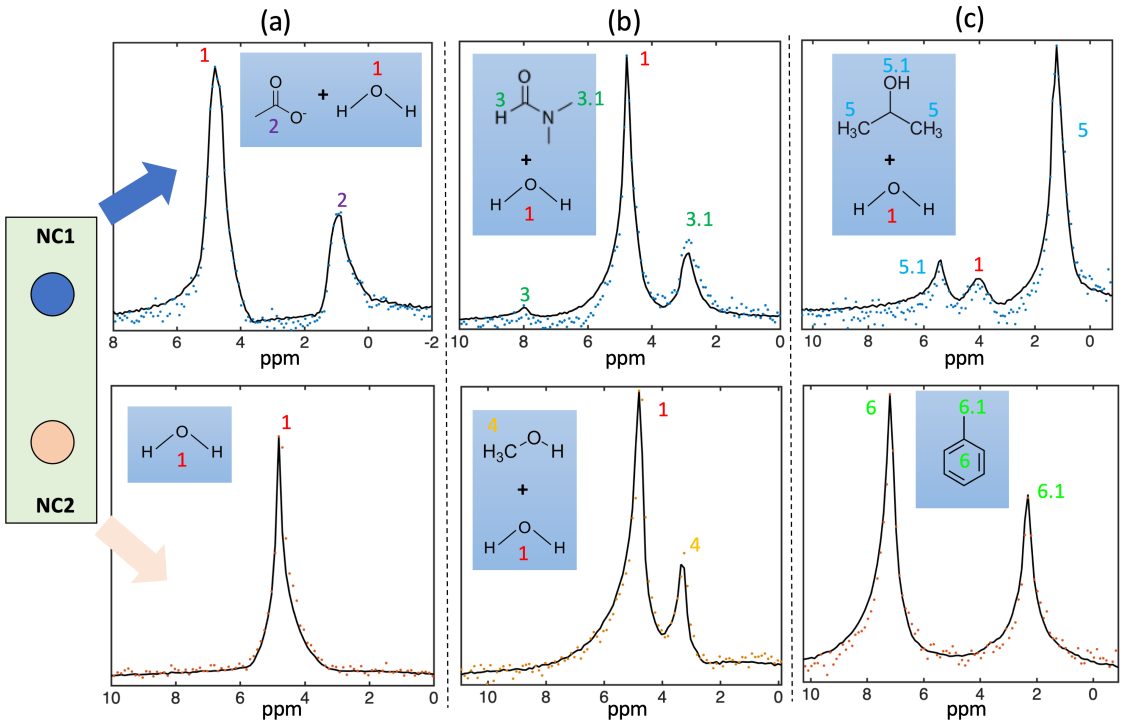

Figure 3.9: Single-shot (dotted lines) and Averaged (solid lines) ^{1}H NMR spectra with synchronized excitation and reception (2 samples in 2 NCs) (a) ^{1}H spectra of acetic acid aqueous solution (top) and DI water (bottom). (b)^{1}H spectra of N,N-dimethylformide (DMF) aqueous solution (top) and methanol in DI water (bottom). (c)^{1}H spectra of 2-propanol in DI water (top) and pure toluene (bottom). Peak numbering: ^{1}H $\rightarrow$ 1, acetic acid $\rightarrow$ 2, DMF $\rightarrow \{3, 3.1\}$, methanol $\rightarrow$ 4, 2-propanol $\rightarrow \{5, 5.1\}$, toluene $\rightarrow \{6, 6.1\}$. (Note that the vertical axis is arbitrary.)

at 0.9 ppm and 4.8 ppm with a FWHM of 22 Hz. However, the J-coupling on the CH_3 peak was not discernable owing to the limitation in the hardware, including the level of magnetization, and the highest shimming order of the magnet system. Even though no detected CH_3 coupling signal was present in H_2O spectrum, both RF coils were operated in synchronized excitation and reception mode, which underscored the decoupling capability of the proposed NC system.

In a second experiment, Fig. 3.9b shows the spectrum of a mixture of both dimethylformamide (DMF) and methanol, each in an aqueous solution. At both measurement sites, 62 scans in 62 s scan time was applied. The ^{1}H water peak for both samples was recorded at 4.8 ppm, the spectrum of DMF is resolved, with ^{1}H peaks at 2.93 ppm, 4.8 ppm, and 8.1 ppm, and the spectrum of methanol with ^{1}H peaks at 4.8 ppm and 3.36 ppm.

Fig. 3.9c presents the spectrum of iso-propanol (IPA) and toluene in 32 scans. The spectra of both samples are referenced at their CH_3 peaks. IPA was referenced at 1.2 ppm, the

other two OH groups were resolved at 4.04 ppm and 5.38 ppm. For toluene, the benzene group peak was at 7.1 ppm, and the peak of the CH_3 group at 2.3 ppm.

Based on the experimental results, it is concluded that the major peak of each sample could be discerned for the evaluation of cross-coupling. Second, it was clear that all three sets of experiments demonstrated sufficient decoupling of the NC coil system, with unwanted coupling signals remaining undetected. Third, the spectral linewidth and hence B_0 homogeneity did not experience any significant change over multiple scans. Fourth, the two samples can be excited in parallel, and detected simultaneously, thereby halving the acquisition time of an equivalent serial experiment.

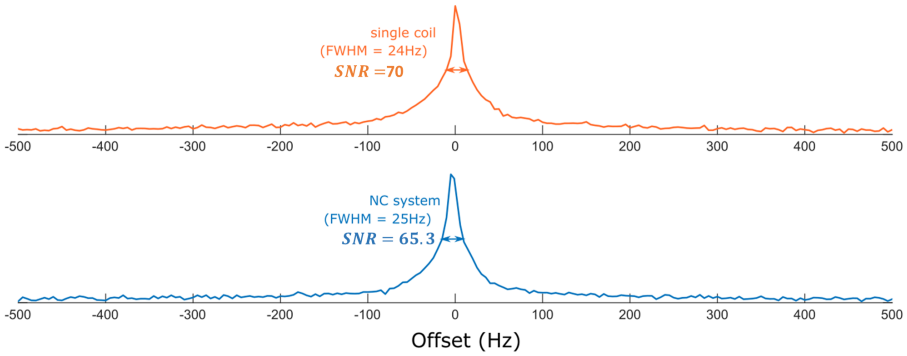

Figure 3.10: Measured ^{1}H NMR spectra with single coil system and dual-coil NC system. Both results are acquired at the optimal achievable line-width, 24 Hz for single coil system and 25 Hz for dual coil NC system.

To determine whether the implantation of a local shim with an RF coil causes noise or linewidth broadening, the traditional single coil spectrum is compared with the NC-based spectrum. Both are carried out under the same experimental conditions, which include the same RF coil, DI water sample, and excitation power. In the single coil test, only the regular shim is utilized. In the dual-coil test, regular shim, NC1 shim, and NC2 shim are utilized. This achieved 24 Hz of FWHM on the ^{1}H peak at the single coil system as shown in Fig.3.10. For an NC based system, 25 Hz of FWHM is achieved, indicating an optimal linewidth can be achieved in the NC system. Nonetheless, the dual-coil NC system spectrum shows similar SNR as to a conventional single coil system.

3.7 Conclusion

State-of-the-art high-throughput NMR spectroscopy reaches its speedup goal through continuous flow arrangements of sample droplets, and is embedded within an additional, automated flow system[27, 65]. Nevertheless, such systems are inherently serial, so that

only one sample can be only characterized at any time, leading to the need to develop coil array implementations for increased throughput. The present article proposes a prototype of a multiple-coil system, based on an integrated NMR cell (NC), towards parallel NMR spectroscopy that potentially extends current high throughput techniques. Here, some challenges have been carefully tackled, such as providing shimming on multiple samples, and achieving geometrical inter-coil inductive decoupling. Our proof-of-principle 1D spectrum results have demonstrated that two side-by-side NCs can achieve the same specifications as a single detector, including a low linewidth and high SNR, implying the future possibility of down-scaling parallel NMR with better resolution and increased SNR, for use also within high field strength superconducting magnets. The potential of integrated systems facilitates the implementation of higher order shim coils, such that the linewidth can be further reduced, and would render rapid compound screening in mixtures possible. Admittedly, when more shim coils are implemented, the shimming procedure will grow in complexity. In conjunction with artificial intelligence strategies, the use of deep regression for NMR shimming [82] is a promising approach with which to accelerate the entire array shimming process. Potentially, the concept can be extended to a larger array of NCs, thereby enabling parallel TX/RX, which would divide the experimental time budget by a factor equal to the number of implemented NCs.

A common method to isolate two transmission line elements, is to position the elements far apart, which reduces the magnetic field coupling by the square of the separation distance. In addition, we demonstrated that the cross coupling of two RF saddle coils can be further reduced with a geometrical misalignment technique. The coupling effect has been evaluated in both simulations, and in synchronized NMR experiments, which indicated a good isolation of two unit NMR cells. Geometrical placement is found to additionally reduce coupling by 23 dB (unloaded) and 9 dB (loaded).

Moreover, the technique is not restricted to saddle-shaped coils, instead, any coil with a similar dipole field can benefit from it. Besides, the technique applies also to micro-coils, allowing a larger ratio of distance to coil size, and when combined with shimming structures, enhances each NC's isolation.

4 Butterfly coil

The contents of this chapter are based on the author's contribution to the material published in the article [J2]. **Material from: Cheng, Yen-Tse et al., A field focusing butterfly stripline detects NMR at higher signal-to-noise ratio, Journal of Magnetic Resonance, published [2023], [Elsevier]**

4.1 Introduction

Obtaining high-resolution spectra from a larger number of individual receive elements requires a highly isolated detection environment. Another key requirement is to enhance the sensitivity in the region of interest, which nudges research towards finding micro coils with a high quality factor Q. Hence, seeking the best coil topology to implement in a coil array has brought our attention to micro coils, especially stripline-based coils, due to their high sensitivity and their inherited RF shielding. The first stripline coil probe for high field NMR spectroscopy was presented by P.J.M. van Bentum et al. [29], exhibiting a very high NMR resolution and good $\mathbf{B}_1$-homogeneity. In parallel, a microslot detector was developed by Maguire et al. [83], which scaled down the sample volume to sub-millimeter dimensions, i.e., by more than a factor of 3,500 compared to a conventional 5 mm sample tube. The planar structure makes the stripline a strong candidate for many applications, such as in-situ electrochemical NMR [31, 84], in-line chemical reaction monitoring [85], or geometrically-differential NMR detection [86]. Additionally, the dual-layer construction, in which one layer is a ground plane, offers a high degree of RF shielding, making it ideal for NMR high-throughput arrays. Previous publications [87, 88] have shown that an electrically highly isolated coil array allows for less signal coupling, removing the need for complex decoupling schemes involving low-impedance preamplifier front-ends [11].

Minute sample quantities, such as individual biological cell clusters, precious biopsies, or bio-active materials which cannot be obtained in large quantities, require a refined mass-limited regime where spins of the sample can be detected with sufficient SNR by the NMR

sensor. Utilizing a micro-coil combined with a microchannel [89] is one of the solutions for such applications with very low detection limit. However, the shrinkage of the stripline coil reduces the spectral resolution due to susceptibility-induced linewidth broadening originating from the proximity of the sample to the coil [83]. Another shortcoming of miniaturized stripline coils is their intrinsically low inductance, requiring larger capacitance to form a resonating circuit, which makes it difficult to integrate with CMOS-based receivers for low-field magnets.

This chapter presents a new stripline design that produces a stronger and more concentrated RF field through a unique butterfly-shaped strip. It improves upon the SNR of a regular stripline when targeting mass-limited samples, which otherwise would result in a low sample filling factor. The presented design inherits the good $\mathbf{B}_0$ homogeneity of the stripline parent, improves $\mathbf{B}_1$ shielding, and achieves $\mathbf{B}_1$ suppression outside the detection region of the stripline, while boosting the detector's NMR sensitivity.

4.2 Resonator design

Based on Bart et al. [90], the geometric parameters of the regular stripline (RS) have been optimized to achieve the best NMR performance; particularly, the SNR is found to reach optimum when the aspect ratio (the ratio of the length of the sensitive part to its width) is 5. Moreover, it is widely accepted that bad resolution mainly originates from the magnetic susceptibility jump along the direction of the B_0 field. That is why solenoidal coils, for instance, are not preferable in high-resolution NMR applications. Therefore, we stick to the sandwich structure as RS with an aspect ratio of 5 to reach its optimal SNR and to avoid the effect of susceptibility artifacts.

Fig. 4.1 shows the modification of a regular stripline into a butterfly stripline, where the center sensitive strip was replaced by two identical and parallel loop coils (L_1 and L_2). Both coils carry the same current and their layout allows the currents to flow oppositely resulting in a B_1 field perpendicular to the B_0 in the sample. The ground plane, besides providing RF shielding, helps to homogenize the B_1 field in the region of interest. The uniqueness of the butterfly stripline is that it goes beyond the sensitivity limits of the conventional stripline by allowing adding as many loops as possible as long as the self-resonance frequency is maintained sufficiently high.

In light of equation 2.9, one can comprehend the superior sensitivity of the proposed butterfly coil by referring to Fig. 4.2, which illustrates its considerably higher current

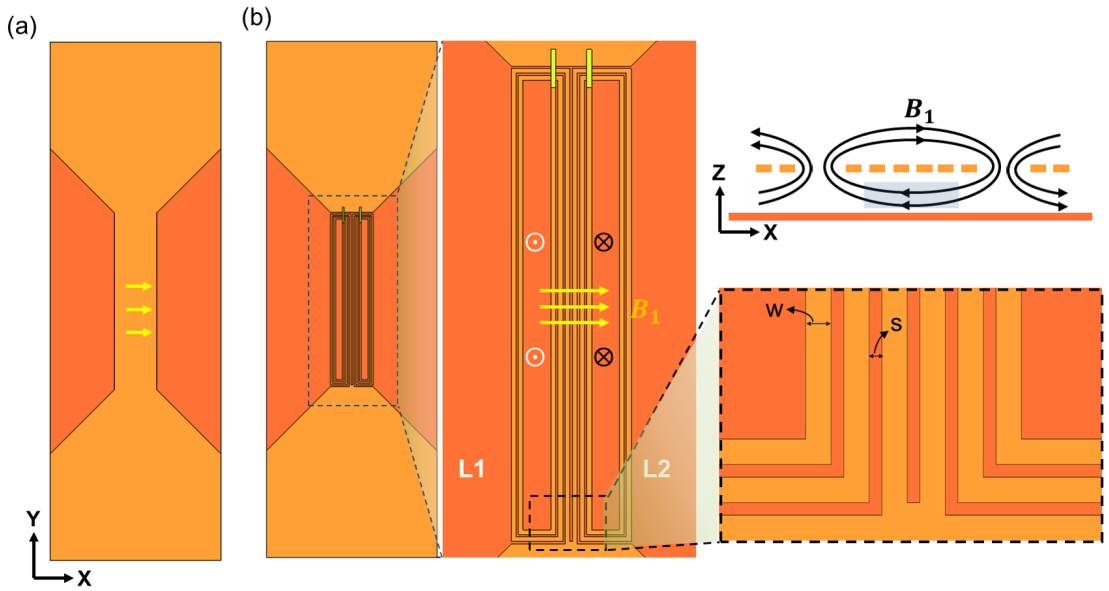

Figure 4.1: The regular and butterfly stripline coils possess a ground plane for RF shielding and produce their $\mathbf{B}_1$ field perpendicular to the $\mathbf{B}_0$-direction. The coils are parameterized by the trace width w and separation between traces $s = w/2$ for the simulation results in figures 4.4 and 4.5. (a) Layout of a regular stripline. (b) The new butterfly-stripline design schematically illustrates the $\mathbf{B}_1$ field streamlines and important geometrical parameters.

density compared to the regular stripline when the same current flows in both coils. It results from the small cross-section of the wires, leading to a stronger $\mathbf{B}_1$ field in the sample region.

4.2.1 FEM simulation

To find a suitable butterfly stripline geometry, we parameterized the dimension of the butterfly stripline, as shown in Fig. 4.1b. The design parameters that define the coil are the trace width w and the space s between traces. Parameters are swept to reasonable values, while avoiding the merging of copper traces. The separation between the stripline and ground plane is fixed to a uniform distance of 500 µm. Electromagnetic simulations are performed with a commercial finite element package (COMSOL Multiphysics 5.4, RF modules, COMSOL AB, Sweden) to reveal their performance for the excitation efficiency, and to achieve the estimated NMR response. Each component in the simulation model is a three-layer stacked structure comprising two metal planes (stripline and ground), sandwiching a sample-carrying capillary. Each coil is excited at a uniform lumped port with an input current of 1 A.

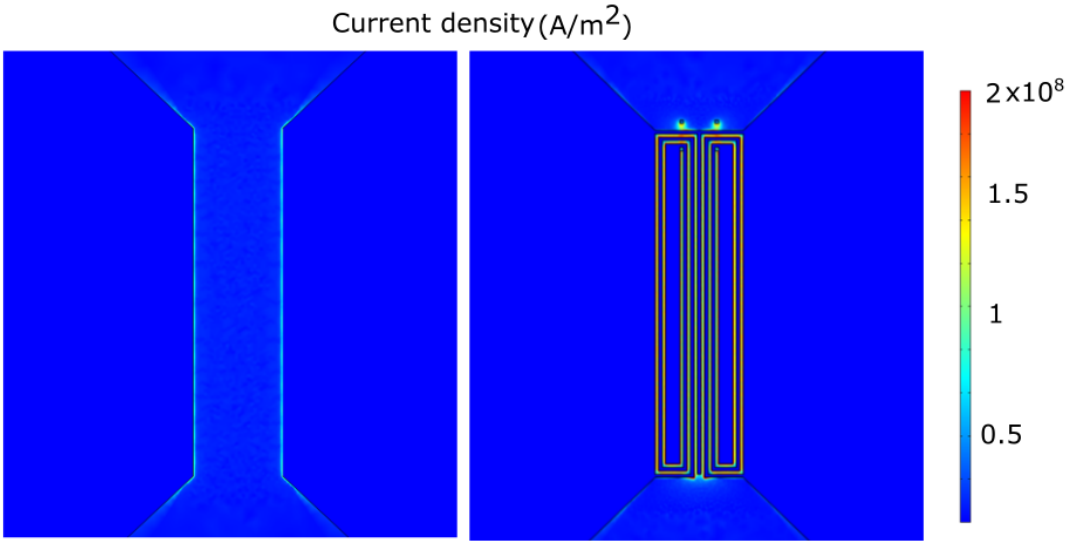

Figure 4.2: A COMSOL simulation of the current density at 45 MHz. The butterfly coil (right) exhibits a considerably higher current density compared to the regular stripline (left) for the same input current.

Table 4.1: Estimated SNR result

	Simulated $\lvert\mathbf{B}_1\rvert$ (mT)	Measured R(Ω)	SNR $(\lvert\mathbf{B}_1\rvert/\sqrt{R})$	Relative SNR
Regular	0.189	0.072	0.704771	1
W02S01T01	1.0946	0.317	1.944132	2.76
W02S02T01	0.954	0.305	1.727476	2.45
W03S01T01	0.928	0.248	1.86371	2.64
W03S02T01	0.823	0.551	1.10917	1.57
W04S01T01	0.792	0.215	1.708071	2.42
W02S01T02	1.3233	0.619	1.68195	2.38
W02S02T02	1.0933	0.512	1.527933	2.17

Fig. 4.4a and Fig. 4.4b display normalized contour plots of the simulated $\mathbf{B}_1$ map over the central cross-section of the coil for the regular and butterfly stripline. The results indicate that the $\mathbf{B}_1$ at the region of interest of the butterfly stripline is 7$\times$ that of the regular stripline, which is significantly higher and due to the confinement of the RF field. The $\mathbf{B}_1$ intensity below the sensitive section decays at the same rate for both coil structures along the vertical z-direction, as seen from the 2% $\mathbf{B}_1$ iso-lines (yellow), also the field above the ground plane in both cases is almost negligible. Furthermore, the iso-line at the edge of the butterfly stripline is much narrower than that of the regular stripline, highlighting its

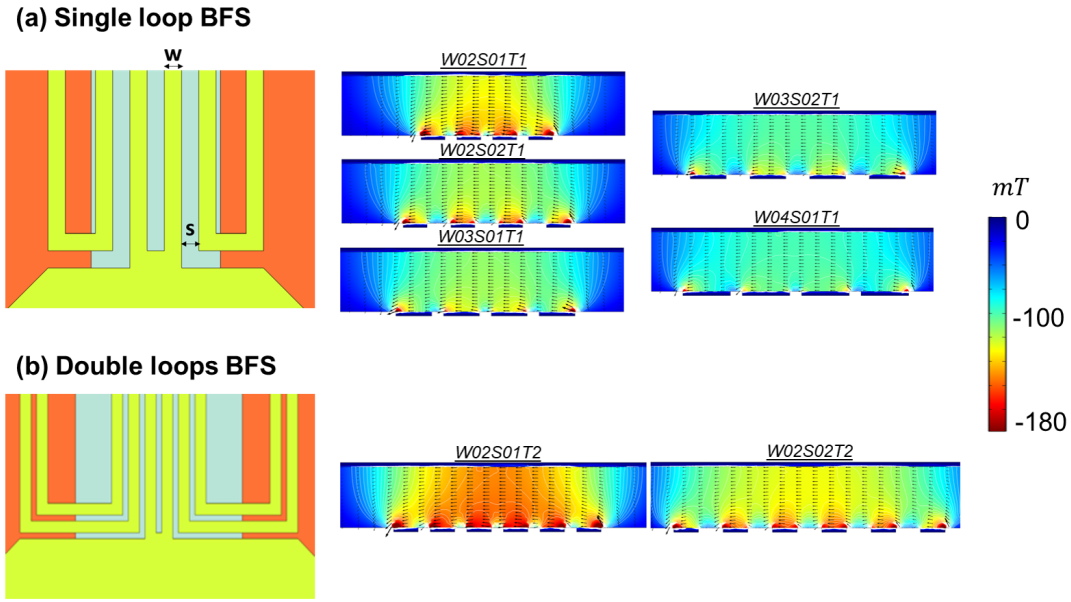

Figure 4.3: $\mathbf{B}_1$ distribution of single loop BFS and double loop BFS with different dimensions obtained from simulation results (Note: W02S01T01 defines $W = 0.2$ mm, $S = 0.1$ mm, number of turns $T = 1$)

superior field shielding and field concentration at the position of the sample. The result can be explained by the cancellation of the field generated from the center and outer loops of the butterfly structure in which the counter currents ensure less field leaking from the edges. Based on a modified Wheeler formula [91] for planar spiral coils, the inductance increases quadratically with the number of windings, thus achieving stronger RF fields by adding more windings. For comparison, we simulated a single-loop and a double-loop butterfly stripline as depicted in Fig. 4.4c, which indicates how the $\mathbf{B}_1$ field in the sensitive area is positively correlated with the number of turns. Also as indicated in Fig. 4.3, we found that a higher $\mathbf{B}_1$ strength can also be attained by reducing the dimension of the looped coils. We further calculated the SNR based on the simulation data, as seen in Table 4.1, showing a maximum SNR enhancement of more than 2.76 times.

An ideal stripline coil should only produce a concentrated magnetic field in the sensitive central region of the strip (the narrow part) and a negligible field at both lateral edges. One important motivation is that the lateral $\mathbf{B}_1$ field could overlap with undesired sample regions, where the $\mathbf{B}_0$ field's homogeneity might be compromised, and thus would result in an unwanted tail in the NMR spectrum. Furthermore, the stripline pads are connected to a tank circuit, where the uniformity and continuity of $\mathbf{B}_0$ is inevitably distorted by the electronic components. Ideally, the sample should only overlap with the strip, but for facile sample handling it would be better to deliver the sample along a longer channel to minimize susceptibility artifacts resulting from the sample-to-air interface. For this

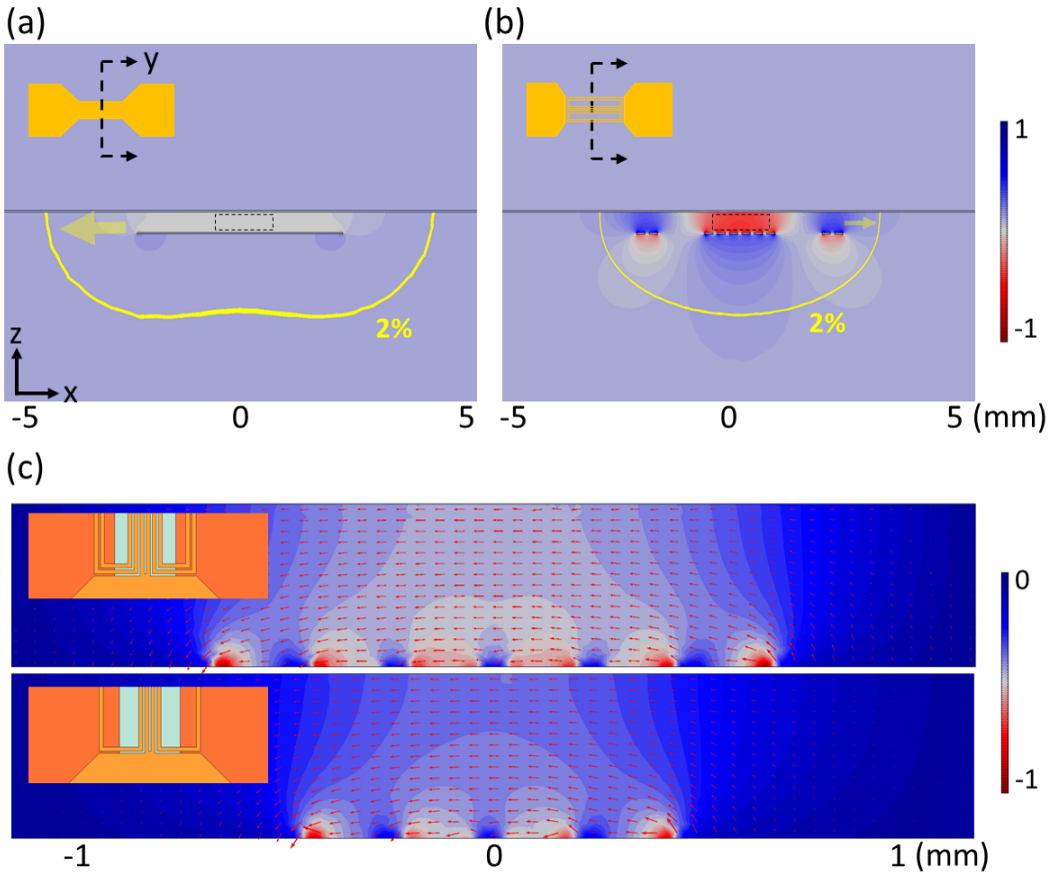

Figure 4.4: Cross-sectional RF field plot at the center of (a) a regular, and (b) a butterfly-stripline coil. (c) $\mathbf{B}_1$ field plots comparing a single and a two-loop butterfly stripline coil at the center cross section (frequency: 45 MHz).

purpose, we simulated the $\mathbf{B}_1$ field in the sample region of both coils along the y-axis, as shown in Fig. 4.5a.The butterfly-stripline exhibits, as depicted, a sharper decay of the $\mathbf{B}_1$ field towards the wider part of the coil, resulting in a lower contribution of this part of the sample to the NMR spectrum. The superior advantage of the butterfly coil in suppressing the sample excitation outside the sensitive region, where field inhomogeneity due to susceptibility jumps typically occurs, was verified experimentally, as illustrated in Fig 4.9, by comparing the sensitivity of the two coils to a sample placed at the stripline pad. Moreover, we simulated the $\mathbf{B}_0$ distribution over a rectangular sample volume $v = 0.5\,\text{mm} \times 3\,\text{mm} \times 60\,\text{mm}$, with an error tolerance of one part per trillion, or $1 : 10^{-12}$. The simulation was carried out with the FEM AC/DC module provided by COMSOL

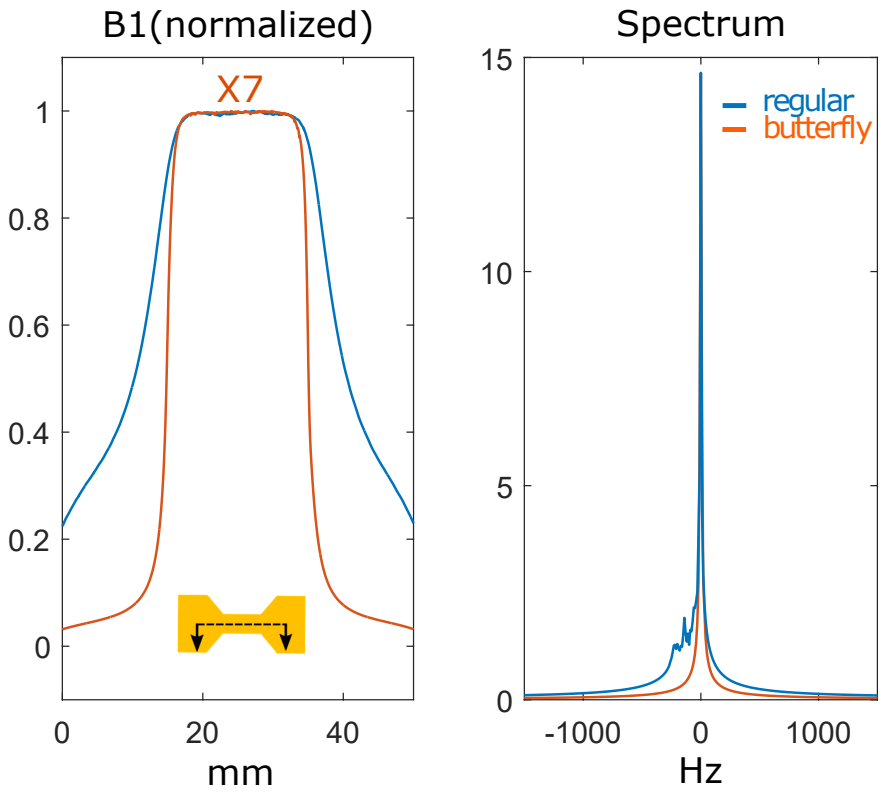

Figure 4.5: (a) Simulation of the $\mathbf{B}_1$ distribution along a regular (blue) and butterfly (orange) stripline. (b) Numerically predicted ^{1}H spectrum using a regular (blue) and butterfly (orange) stripline.

Multiphysics 5.4. We post-processed the simulated $\mathbf{B}_0$ and $\mathbf{B}_1$ result on the sample to estimate the NMR spectrum before shimming, given by [12]:

$$\zeta = -\int_{sample} \frac{\partial}{\partial t}\mathbf{B}_1 \cdot \mathbf{M}_0 \, dV_s \tag{4.1}$$

where $\mathbf{B}_1$ and $\mathbf{M}_0$ represent the RF field and the magnetization in each FEM mesh element of the sample. All mesh elements within the sample were assumed to have the same spin density. Fig. 4.5b clearly shows that the spectrum in the butterfly-stripline had a much narrower peak than the regular stripline, implying better spectral resolution. The NMR spectrum only considered the RF coil and the sample in a 1.05 T $\mathbf{B}_0$ field.

4.3 Coil fabrication and experimental result

Based on the simulation results, both the double-loop butterfly and a regular stripline were selected for comparison. The two coils were fabricated using a commercially available PCB technology, and each resonator comprised three layers, a stripline, a PMMA spacer, and a ground plane, as illustrated in Fig. 4.6a. Each coil was fabricated with an overall length of 40 mm, and a width of 20 mm, with a sensitive conductor section of 20 mm $\times$ 5 mm.

After assembly, the resonators were tuned and matched using a network analyzer (E5071C, Agilent), using nonmagnetic capacitors (model 5641, Johanson Manufacturing, NJ), to the ^{1}H Larmor frequency, corresponding to 45 MHz. Both coils were tested in a pre-clinical 1.05 T cryogen-free MRI magnet system (Bruker Biospin, Ettlingen, Germany)

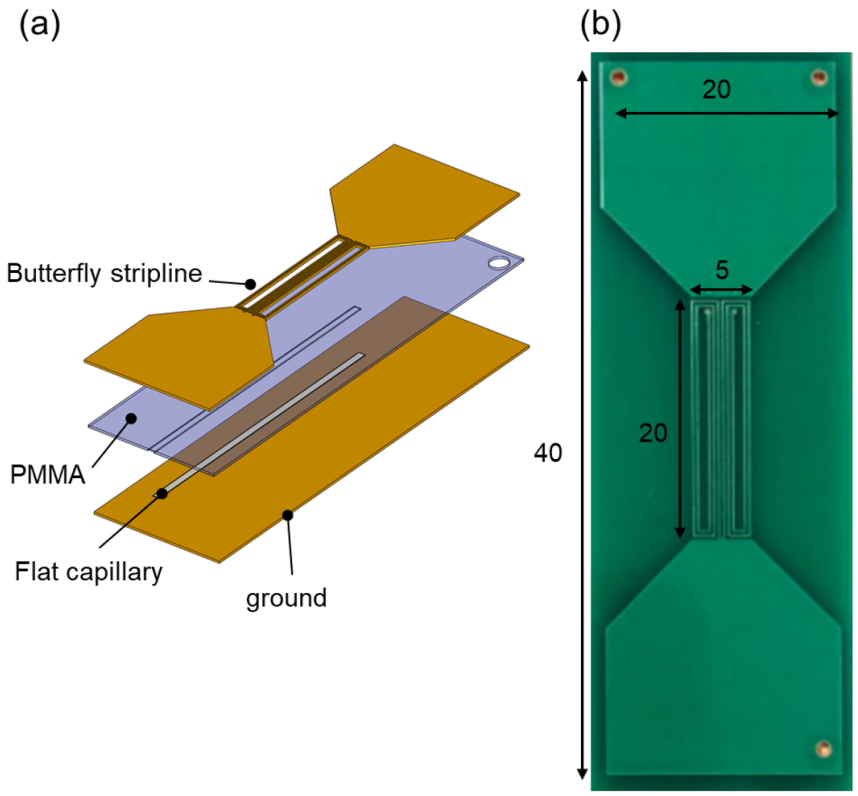

Figure 4.6: (a) The schematic assembly of a butterfly device starts with a top stripline, a PMMA spacer, a flat capillary, and a bottom ground plate. (b) The photo depicts a double-loop butterfly stripline, with 200 µm wide copper tracks, and a 100 µm gap separating the conductor stripes. The two upper vias shown in the photo are used to connect the stripline to the bottom ground plate. All units are in [mm].

One experiment that can evaluate the NMR performance of the butterfly coil, and compare it with the regular stripline, is to measure the nutation curve of the two coils. The ^{1}H nutation signals for both coils are depicted in Fig 4.7. According to these results, the

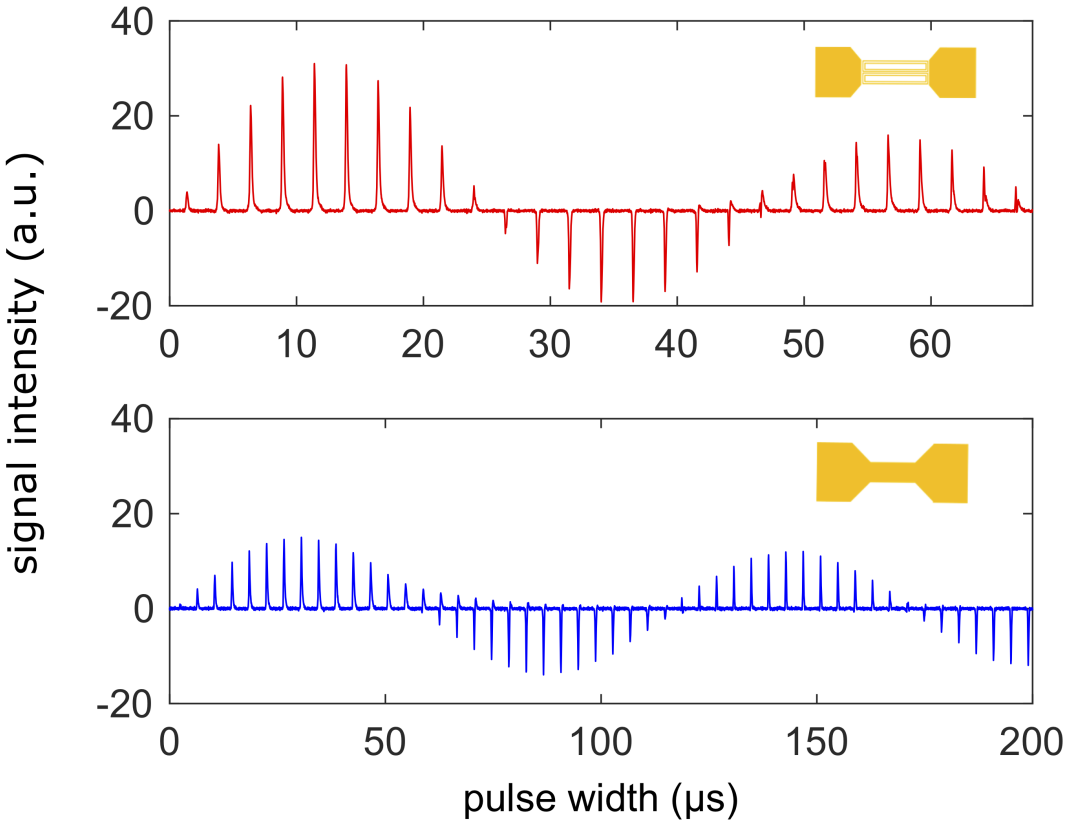

Figure 4.7: ^{1}H Nutation curves of a two-looped butterfly stripline coil (red) and a regular stripline coil (blue). Both coils have the same geometrical footprint, and are excited with 1 W.

maximum NMR signal intensity (around 15 [a.u.]) for regular stripline was achieved at an excitation pulse of $\tau = 30\,\mu s$ and the $\mathbf{B}_1$ uniformity at 450°/90° ratio is around 80 %. On the other hand, the butterfly coil showed a maximum signal intensity of 31 [a.u.] at an excitation pulse duration of $\tau = 11\,\mu s$. Both coils were excited with 1 W. Even though the 450°/90° is decreased to 51 %, the result indicates a large $\sim 2\times$ improvement of SNR, and a $\sim 2.7\times$ reduction in the 90° pulse duration.

An acceptable signal coupling below $-20\,dB$ for two spaced coils has been used as a standard requirement for an MRI array with a decoupling scheme [92]. Although it is possible to utilize techniques such as active decoupling to reduce the crosstalk further, it is still necessary to maintain the geometrical coupling of the coils as low as possible. As indicated in the simulation result, the butterfly-stripline exhibits a relatively more confined RF field map than the regular stripline at the narrow region of the sensitive section. To verify this, four coils (two copies of the regular stripline and two copies of the butterfly coil) were tuned to 45 MHz and matched to $50\,\Omega$ at the bench, with a scattering parameter S_{11} less than $-15\,dB$. The coupling coefficient S_{21} of an array of two similar coils was measured while varying the distance between the coils for two scenarios, once placed

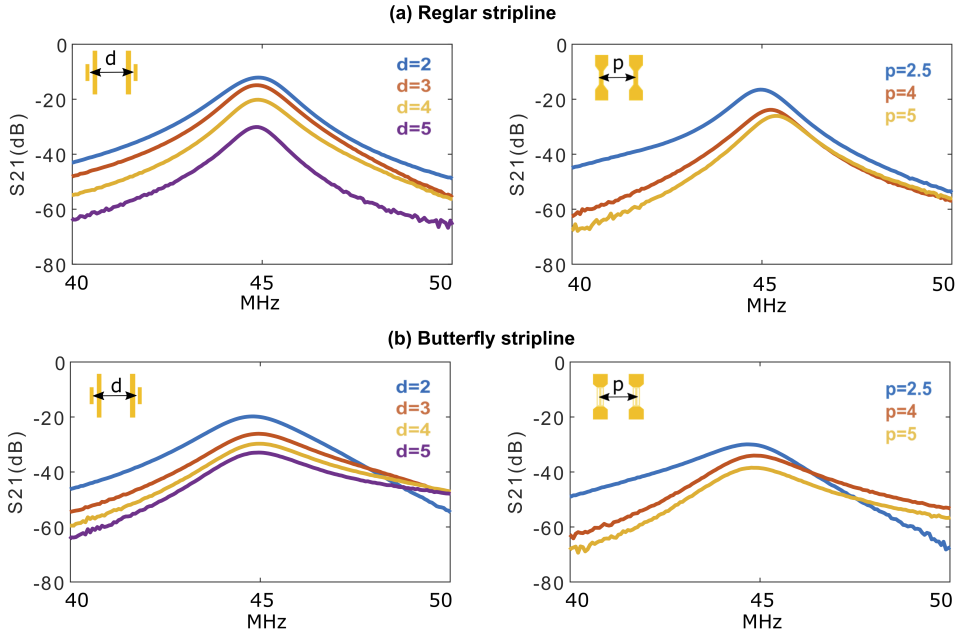

Figure 4.8: (a) Coupling coefficients for two regular stripline coils resonating at 45 MHz, for different back-to-back distances, ranging from 2 cm to 5 cm, with S_{21} varying from -12.25 dB to -30.65 dB, and side-by-side distances from 2.5 cm to 5 cm, with a corresponding S_{21} varying from -16.54 dB to -27.75 dB. (b) Coupling coefficients for two butterfly stripline coils resonating at 45 MHz, for the same back-to-back distances with S_{21} varying from -20.04 dB to -32.96 dB, and same side-by-side distances with S_{21} varying from -30.51 dB to -38.62 dB.

back-to-back, and once placed side-by-side. Figs. 4.8a and 4.8b summarize the results for the two stripline arrays. Compared to the regular stripline, the butterfly exhibits a stronger coupling suppression of 7.79 dB to 2.31 dB for a back-to-back distance range $d \in 2$ cm to 5 cm. Also, a stronger signal decoupling range of 14 dB to 10.87 dB is achieved by the butterfly topology for a side-by-side separation in the range $p \in 2.5$ cm to 5 cm. The result can be explained from the distribution of the $\mathbf{B}_1$ field, see Fig. 4.4a,b. The elliptical shape of the butterfly coil's $\mathbf{B}_1$ field has a lower horizontal stray field than the saddle shaped field of the regular stripline, leading to a stronger suppression of coupling.

4.4 Conclusion

We have presented a method with which to boost the sensitivity of a regular stripline when its filling factor is low due to limited sample mass. The idea, based on replacing the sensitive part of a regular stripline with a multi-loop butterfly coil, yielded a factor 2 enhancement in sensitivity, and a 14 dB lower coupling when the coil was used in an array configuration. Furthermore, the FEM simulations showed a sharper $\mathbf{B}_1$ suppression outside

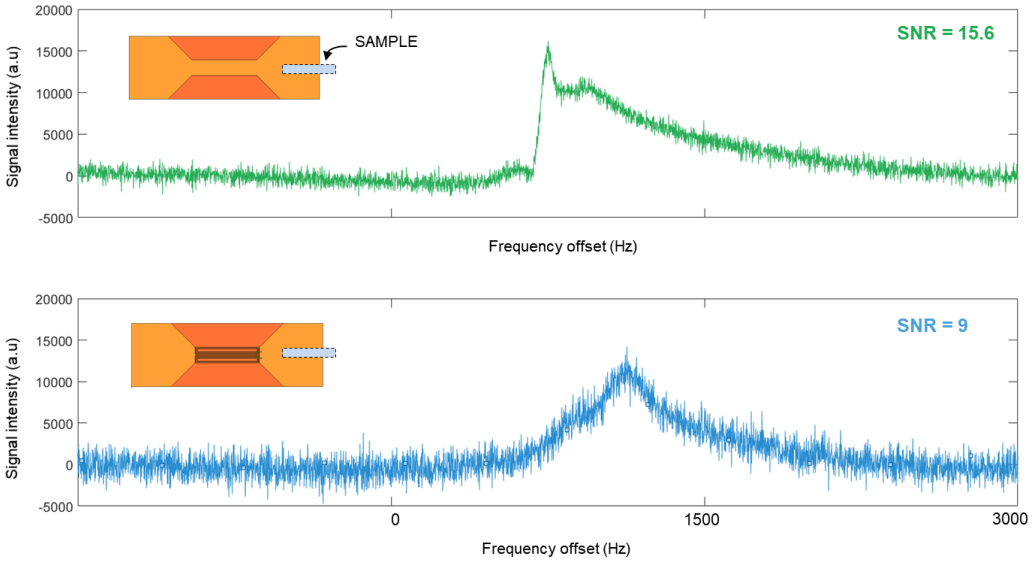

Figure 4.9: Averaged NMR spectrum (10 scans) from a sample located at the pad for a) a regular stripline, and b) a butterfly coil. The latter exhibits a stronger suppression of the sample outside the sensitive region where field inhomogeneity, due to susceptibility jumps, occurs.

the region of interest compared to the RS. The proposed design additionally offers a major advantage of design flexibility where the butterfly structure can be freely optimized, in terms of geometry and number of loops, to achieve arbitrary $\mathbf{B}_1$ profiles. For instance, an asymmetric butterfly structure could be used to produce a linear $\mathbf{B}_1$ gradient along any axis for $\mathbf{B}_1$-gradient coherence selection [93].

In the present study, the butterfly stripline has not yet been exploited in an array for high-resolution parallel MR detection. Nonetheless, its enhanced shielding, confirmed from simulation and experimental results, makes it a good candidate for parallel MR experiments [J1], due to the self-cancellation of the RF field away from the stripline. This guarantees not only less signal coupling to neighboring detector units but also a more dense arrangement of the array.

5 Continuous flow high throughput parallel SABRE

5.1 Introduction

Presently, numerous applications are still constrained by the inherently low sensitivity of traditional NMR detection methods, attributed to the very small energy band gap between nuclear spin states in the presence of the static magnetic field of an NMR spectrometer [94]. Particularly in cases of small sample volumes or low concentrations, a practical yet "slow" method involves acquiring replicate spectra, which are then post-processed to discern small peaks. In such scenarios, experimental time would increase exponentially; for example, achieving a two-fold enhancement of SNR would necessitate four times the measurement time for replicates. Some common hardware-based approaches to increasing sensitivity involve using increasingly powerful, albeit expensive, ultra-high-field superconducting magnets (GHz Class) to boost spin polarization[95]. Another approach is to employ a cryoprobe that cools the RF coil and preamplifier with liquid helium or nitrogen, reducing thermal noise from the electronics and providing up to a four-fold SNR enhancement [96].

An alternative way to overcome the extensively high measurement time imposed by the limited sensitivity of NMR is so-called nuclear spin hyperpolarization. This method involves perturbing nuclear spin state distributions either in-situ or ex-situ during chemical or physical reactions. As nuclear spins are hyperpolarized beyond the equilibrium state, often achieving enhancements of several orders of magnitude, this technique greatly enhances the SNR of the spectrum. However, their adoption in the parallel spectroscopy system hasn't been explored. As in our previous proposed method [97], a parallel platform that employs integrated shimming to simultaneously analyze two samples within two identical NMR sensors. The synchronized operation of the dual-coil system is demonstrated to lead to a two-fold reduction in detection time (Chapter 3).

Current hyperpolarization techniques based on transfer mechanisms include Para-Hydrogen Induced Polarization (PHIP) [98], Dynamic Nuclear Polarization (DNP) [99], and Spin-Exchange Optical Pumping (SEOP) [100].

DNP is a strong spin polarisation method first predicted by Overhauser[101]. Spin polarization is transferred from electrons to nuclei through the microwave irradiation near the electron resonance frequency on the sample containing target nuclei incorporates unpaired electrons, i.e. radicals. The signal amplification is due to the higher gyromagnetic ratio of electrons than that of proton (by 660 times). However, the fundamental spin-transfer reaction happens in the microwave frequency and requires an efficient waveguide to transmit the microwaves from the external microwave source to the probe, and the probe should contain an efficient microwave cavity or waveguide to irradiate the polarizing electrons [102]. This demands not only costly and stable microwave sources but also poses challenges in integrating the microwave waveguide with a parallel probehead.

In the context of SEOP, polarization is transferred from the high-intensity alkali metal vapors' electrons to the nuclei of noble gases, such as ^{3}He and ^{129}Xe, through the use of circularly polarized light [103]. However, this technique is usually employed in clinical applications, for example, functional lung imaging for patients with respiratory diseases. Also, most SEOP instruments are large and expensive, comprising an oven to heat noble gases and a narrow-banded high-power laser diode for irradiating the alkali metal, along with optics that must focus and steer the circularly polarized light.

In the context of PHIP [98], when pH_2 as the source of polarization transfer was present to the un-saturated chemical molecules, they broke into the magnetic symmetry of nascent pH_2 protons, making them highly polarized. Via hydrogenation reactions, PHIP can be performed in low or high fields. The first proof of PHIP effect was published by Bowers and Weitekamp [104]. Compared to some other hyperpolarization techniques, obtaining pH_2 is relatively straightforward and cost-effective. Furthermore, the generation of polarization only takes a few seconds, eliminating the need for extended waiting times between measurements. The main additional cost for this method is associated with obtaining high concentrations of pH_2 through a cooling system.

Within the realm of PHIP, a technique known as Signal Amplification by Reversible Exchange (SABRE) [105] also employs pH_2 as the polarization source, eliminating the need for chemical attachment to a molecule with an unsaturated C–C bond. SABRE is reversible and repeatable, involving the transfer of polarization from pH_2 to a substrate in a transient organometallic complex. It inherits the advantages of PHIP, producing polarization within a few seconds [106] and yielding a 1000X signal enhancement in 1D or 2D NMR experiments. Notably, hyperpolarization can occur ex situ at a low magnetic field, alleviating the spatial constraints on NMR arrays. Additionally, SABRE is compatible with a flow probe [107], utilizing an external sample preparation cell that

allows re-hyperpolarization and operates continuously. Moreover, it can be easily applied to different field strengths without requiring further modifications to the instruments.

Here, we introduce a direct implementation of this platform with the SABRE technique, enabling parallel SABRE. The primary advantage is a halving of the required measurement time for sequential samples. Additionally, the low-field magnet, known for its low SNR, can benefit from SABRE, significantly enhancing signal intensity and facilitating the measurement of low-concentration samples. Finally, the hyperpolarization is performed continuously, increasing throughput.

5.2 System design and setup

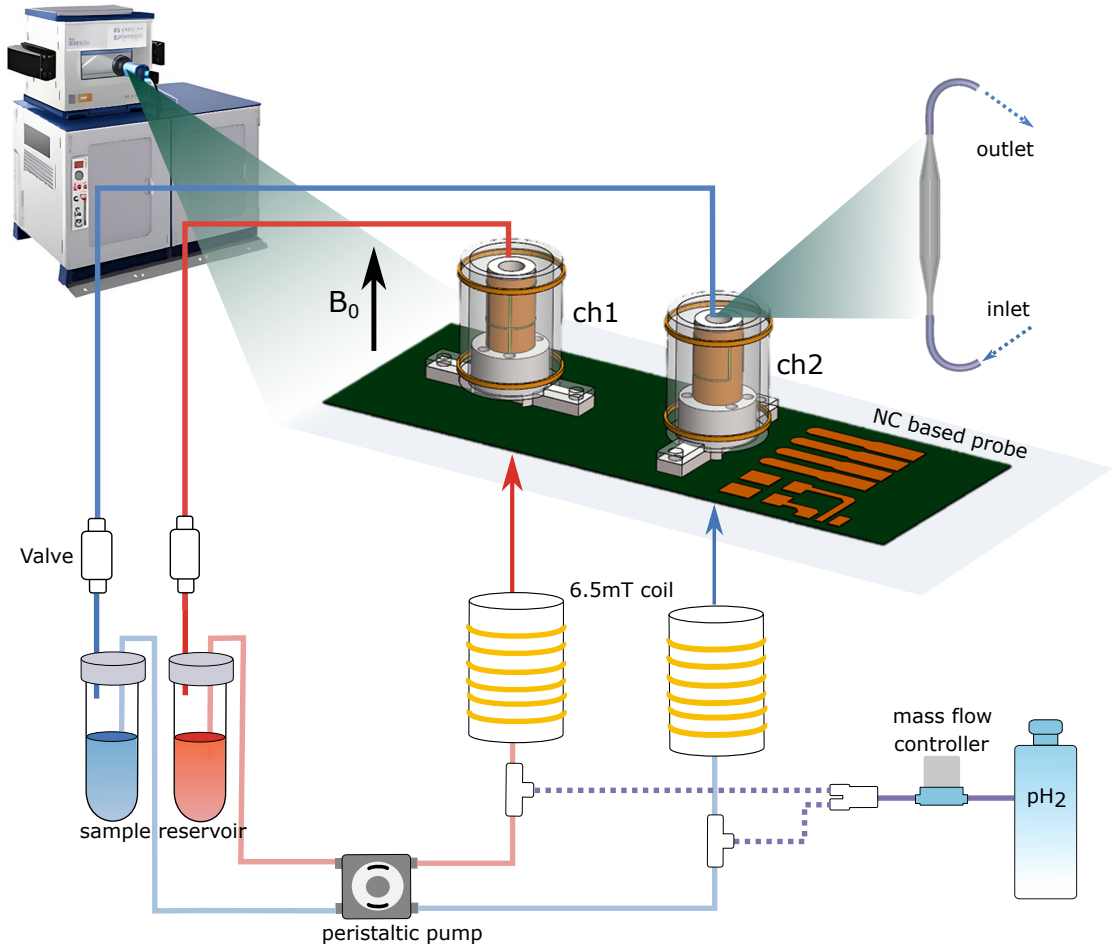

Figure 5.1: Overview of continuous parallel SABRE experiment setup utilizing an NC-based parallel probehead. The NC probehead is positioned inside the 1.05 T horizontal field magnet. The feature of the NC probehead has been briefly introduced in Ch.3, including parallel shimming, and parallel acquisition. Parahydrogen flow is regulated through a mass flow controller to ensure proper pressure equilibrium throughout the system. Two bifurcation gas flows go into the tube-in-tube reactor inside the 6.5mT coil. Two sample solutions are transported inside the probe through two fluidic channels and controlled by the peristaltic pump. Printed conical-sided flow cells were inserted inside RF coils allowing fluid continuous transportation. The sample solution can be continuously re-hyperpolarized.

The portion of the flow setup situated outside the NMR magnet is illustrated in Fig. 5.1. As mentioned in the introduction, the concentration of pH_2 significantly influences the signal enhancement in SABRE experiments. Therefore, pH_2 gas is pre-stored in a container with an approximately 90% concentration. The gas flow is then regulated by the mass flow controller to maintain proper pressure equilibrium in the system, with 5 bar used as the pressure setting. The gas is transported through a 5 mm inner diameter PE tubing and

then bifurcated into two tube-in-tube reactors. These reactors are positioned within the 6.5 mT field coil, recognized as the optimal transfer field for polarizing the ^{1}H nuclei on the substrate [108]. The 6.5 mT coils are strategically placed before the NC probe to minimize the travel time from reactors to the NMR detection site, thereby mitigating relaxation decays that affect polarization.

To facilitate SABRE sample transportation, we employed two identical fluidic systems for the continuous circulation and hyperpolarization of samples. The samples utilized in the two channels (Ch1 and Ch2) were as follows: Ch1 contained 3 mM Ir-Mes catalyst and 60 mM Pyrazine in 3 mL deuterated Methanol, while Ch2 contained 3 mM Ir-Mes catalyst and 60 mM Pyridine in 3mL deuterated Methanol. Sample flow was regulated between 0 and 8 mL/min, pumping from the reservoir to the reactor. After polarization, the sample was injected into the detection site within the 1.05 T field magnet. The sample tube used in the system had a diameter of 1 mm, and is made of PTFE tubing. Instead of utilizing a maximum size of 5mm tubing to flow through the RF coil, we opted for a 3D-printed NMR-free resin-based flow cell. This flow cell featured two conical sides for tube connection, preventing unnecessary fluid transport outside the probehead. To avoid the generation of bubbles, the liquid was pumped upward to the flow cell inside the probehead. The flow cell's structure could be customized as needed. After passing through the probehead, the two samples were returned to their respective sample reservoirs for subsequent re-hyperpolarization.

5.3 Parallel SABRE experiment

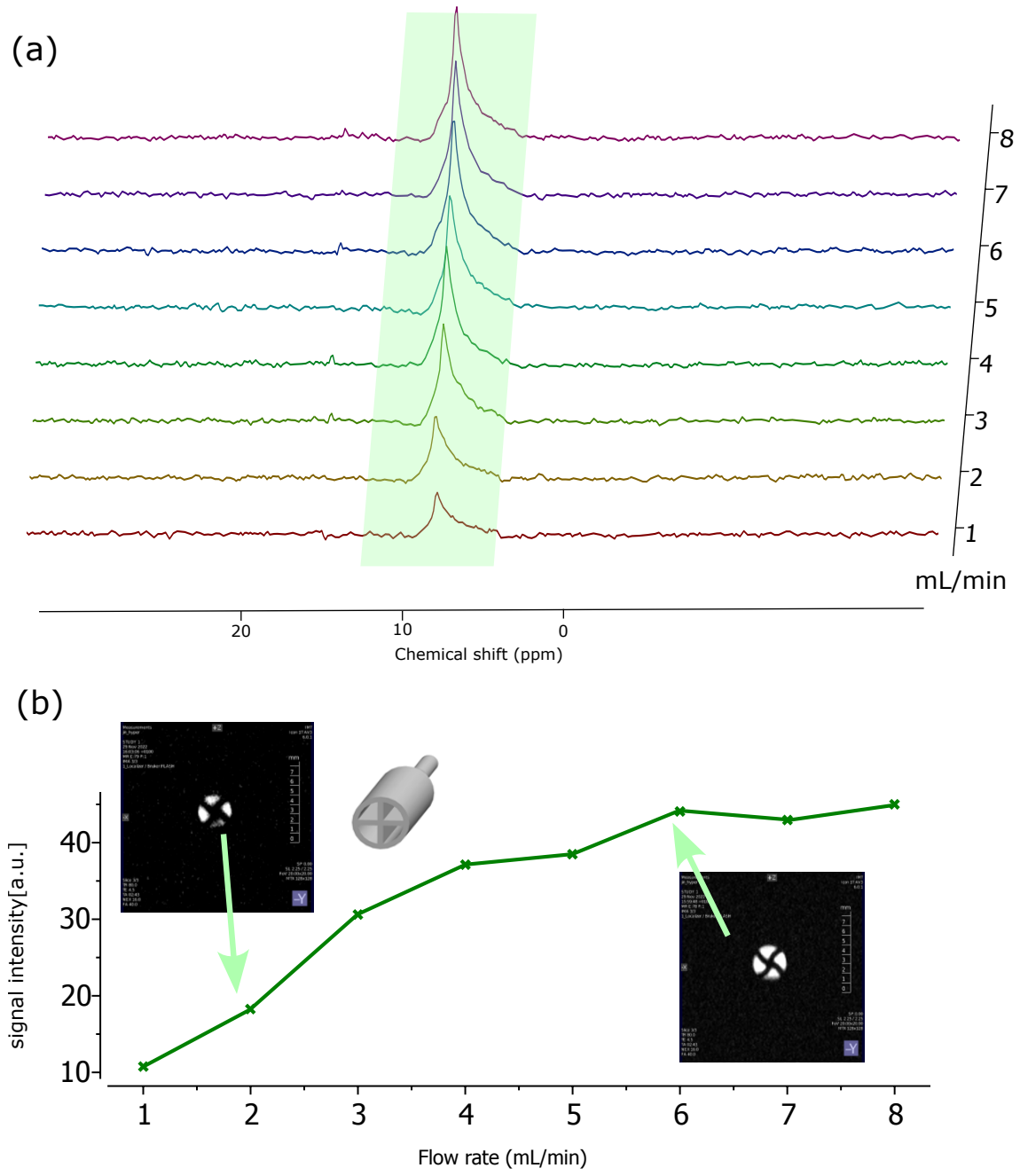

Figure 5.2: (a)^{1}H 1D spectra of 25mM Pyrazine transported at a flow rate of 1 to 8mL/min. (b) The relationship between the signal intensity of the major peak of Pyrazine and the transporting flow rate. SABRE MRI images of a 3D-printed flow cell with a feature of cross-cross-section are included. MRI images were acquired when the sample ran at a flow rate of 2mL/min and 6mL/min.

The first experiment investigates the compatibility of SABRE hyperpolarization with our custom-built probe. To visualize the SABRE effect, we implemented a flow cell with a cross-cross-section inside the sensitive region (Fig. 5.2b). An important factor

affecting the SABRE signal enhancement is the flow rate. Due to the relaxation time, signal enhancement is positively proportional to the flow rate. In the SABRE experiment, 25mM Pyrazine is filled in channel 1. We acquired several ^{1}H 1D spectra with different flow rates, ranging from 1mL/min to 8mL/min, as plotted in Fig. 5.2a. We found that the signal intensity of Pyrazine increases with the flow rates.

However, there's a limit for signal enhancement when the flow is too fast to sufficiently thermally polarize the methanol. We evaluated the maximum signal intensity of each spectrum and correlated them with the sample transportation flow rate. It's found that the signal enhancement reaches the maximum at a flow rate of 6 mL/min and gets saturated. A simple Flash MRI sequence was used. The one-shot images were recorded with an echo time, TE, of 4.5 ms and a repetition time, TR, of 80 ms. The slices were oriented in the cross-sectional plane of the flow cell, with a field of view (FOV) 20X20 mm, a flip angle of 30°, and a resolution of 128 lm/pixel on the 2D plane. The MRI image is shown in Fig. 5.2b. The image of the faster flow has a larger contrast than the slower flow indicating a stronger signal enhancement.

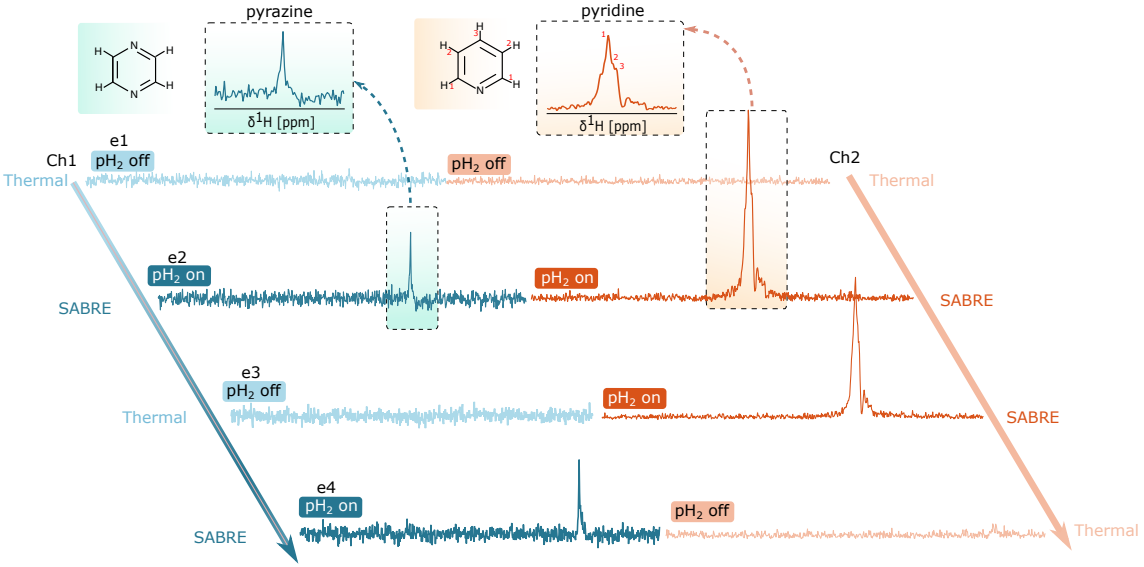

Figure 5.3: (a) Parallel 1D ^{1}H SABRE spectra of Pyrazine and Pyridine with and without the introduction of pH_2 gas. Four sets of experiments are conducted as follows: (i) Ch1: pH_2 off, Ch2: pH_2 off (ii) Ch1: pH_2 on, Ch2: pH_2 on (iii) Ch1: pH_2 off, Ch2: pH_2 on (iv) Ch1: pH_2 on, Ch2: pH_2 off.

Similar to the parallel experiment conducted in Chapter 3, a parallel NMR experiment was demonstrated using a pre-clinical 1.05 T cryogen-free MRI magnet system (Bruker Biospin, Ettlingen, Germany) and a custom-built probe. The probehead used in this study underwent remodeling, with all 3D printed supports replaced with borosilicate glass tubes to reduce the background signal caused by PLA polymer. For the RF component, one

RF coil was connected to the ICON spectrometer and executed a typical ^{1}H single pulse experiment under the ParaVision software interface (version 6.0.1, Bruker). The second coil was connected to another NMR spectrometer (Magritek). A TTL line was utilized to connect the two spectrometers for synchronization. Two different samples (Pyridine and Pyrazine) were continuously pumped at the same flow rate of 5 mL/min in two separate channels for sample transportation.

In the first experiment, pH_2 gas was turned off in both gas channels, revealing two thermal-equilibrium spectra. Due to the low concentration, any peaks were hardly characterized in the two spectra. In the second experiment, pH_2 gas was turned on in both gas channels, resulting in the buildup of polarization, substrate transfer, and reaching maximum signal intensity. A peak located at 7.8 ppm was resolved in the Pyrazine spectrum, and a triplet peak (in the range of 8 to 8.8 ppm) was resolved in the Pyridine spectrum. Subsequently, pH_2 gas in channel 1 was turned off, causing the SABRE effect to diminish and return to the thermal equilibrium state. In the last experiment, pH_2 was turned on in channel 1 and off in channel 2. Pyrazine was hyperpolarized again, and Pyridine reached a thermal equilibrium state.

Based on the experimental results, it was observed that the main peak of each sample could be discerned after SABRE hyperpolarization. Furthermore, the spectral linewidth was deemed acceptable for distinguishing the major peak of the sample substrate, thanks to parallel shimming. Lastly, the two samples could be excited in parallel, and, most importantly, easily re-hyperpolarized, enabling strong signal enhancement.

6 Parallel NMR spectroscopy at 15.2T field

The contents of this chapter are based on the author's contribution to the material published in the article [J3]. **Material from: Becker, Moritz, Cheng, Yen-Tse et al., Artificial intelligence-driven shimming for parallel high field nuclear magnetic resonance, Scientific Reports, published [2023], [Springer Nature]**

This chapter presents a comprehensive overview of the design, characterization, and assembly of a high-field parallel NMR spectroscopy probehead. This probehead is operated in 15.2 T MRI magnet. Parallelizing NMR spectroscopy at a high field is achieved through the integration of various components, including a miniaturized RF coil, a compact shim set, and a fluidic tubing system enabling continuous-flow measurements. Several crucial aspects are addressed herein. Firstly, the chapter discusses the adaptation of the NC concept to a high-field MRI magnet operating at 650 MHz, requiring extensive modifications to the hardware design of the low-field NC system due to frequency variations with magnetic field strength. Secondly, the challenges encountered during the parallelization of an array of shim coils ($>$20) necessitate the implementation of a multi-channel constant current source to drive multiple coils. Third, it outlines the design of a robust sample-holding method for the straightforward transferring of samples to the detection region. Fourth, it presents an optimized parallel shimming procedure for a shim array, given the absence of a standard method for automatically shimming multiple samples. Lastly, the chapter present post-processing method to deal with signal cross-talk.

The chapter is structured into several sections. Sec. 6.1 delves into the technical aspects and design considerations of various components in the parallel NMR system. This section encompasses an in-depth discussion of a novel RF coil, a compact local shim system, a self-built 24-channel constant current source, and a comparison between two versions (2-Ch/4-Ch) of the parallel probehead. In the end, results from parallel experiments are presented, shedding light on the probe head's operation in this configuration. Moving to Sec. 6.2, the chapter explores the concept of AI-driven shimming, seeking to automate the

shimming process for the proposed parallel probe head. The validation of this concept in a high-field magnet is also scrutinized. In Sec. 6.3, two methods to address signal cross-talk are demonstrated, one is empirical method and the other is blind source separation.

6.1 Parallel probe system design consideration

Building upon the NMR cell design detailed in Chap. 3, we have extended the NC concept to align with a 15.2 T high-field magnet. This section commences with an introduction to a groundbreaking RF coil design known as the fold-up stripline, a pivotal element in a single NMR cell utilized for spin signal detection. Additionally, in response to the spectra results from the low-field parallel system, we have refined the design of the shim coils. Recognizing that the linewidth of the spectra is insufficient for spectroscopic purposes, we have incorporated first to fourth order shims to address this limitation. The chapter also provides details on the two new NC designs. Following this, two new probehead designs (4 Ch and 2 Ch) are presented, and parallel spectroscopy was demonstrated within the subsequent subsection.

6.1.1 Design of fold-up stripline coil

Based on the conclusion in Chap. 3, the concept of NC can be extended to a larger array of NCs, enabling a large reduction of experiment time by the number of NCs, also to a high-field environment enabling higher SNR since the sensitivity increases with main field (B_0) by $B_0^{7/4}$. One technical challenge arises from the size of the preceding NC (17 mm OD), which imposes limitations on the number of NCs that can be integrated into the probe head, taking into account signal cross-coupling. Previously, only two coils could be accommodated. Hence, there is a pressing need to downsize the entire NC, encompassing the RF coil, local shims, and sample size. Additionally, based on the findings presented in Chap. 3 and 4, the stripline coil naturally emerges as a suitable candidate for parallel NMR sensors. This is attributed to the fact that the RF field is highly confined in the ROI, where the stray field is minimized.

We leverage the idea of microcoil which is small but also sensitive to small sample volumes, with limit of detection down to 0.1 (nmol/$\sqrt{Hz}$) [109]. Some literature indicate that a microfluidic based chip can be implemented to transfer samples [110]. In the pursuit of miniaturizing the stripline coil, one can continue reducing its dimensions and employing the clean-room method for fabrication. However, this might be not trivial

since micro-fabricating the metal via connecting the two planes is complicated. It is also possible to fabricate stripline coil as a self-resonant structure, while it poses challenges for miniaturization, mainly due to the necessity of a $\lambda/2$ length strip to generate a concentrated RF field in sensitive regions [90]. Moreover, the metallic via connecting the stripline to the ground plate, creates a localized B_0 and B_1 distortion, causing an unwanted shoulder in the spectrum.

Fig. 6.1 shows a new design of stripline coil using the fold-up method. Our design's key innovation involves relocating the via with an extensive arm positioned on top of the stripline, enabling an all-in-one fabrication procedure for the metal layer. This approach simplifies the fabrication process, facilitating the miniaturization objective. The proposed stripline, illustrated as an example in Fig. 6.1a, possesses an overall length of 25 mm and a width of 5 mm, with a sensitive conductor section measuring 8 mm × 1.3 mm. The coil is crafted on a flexible polyimide substrate, allowing for the folding of the coil.

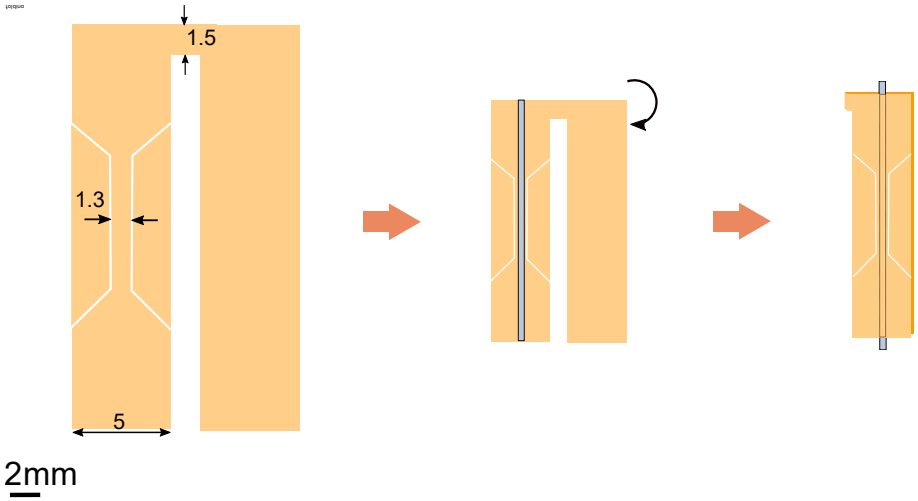

Figure 6.1: Schematic step-by-step procedure of folding the proposed flexible stripline coil. The dimension of stripline is 5x25 mm^2 with sensitive strip of 1.3x8 mm^2

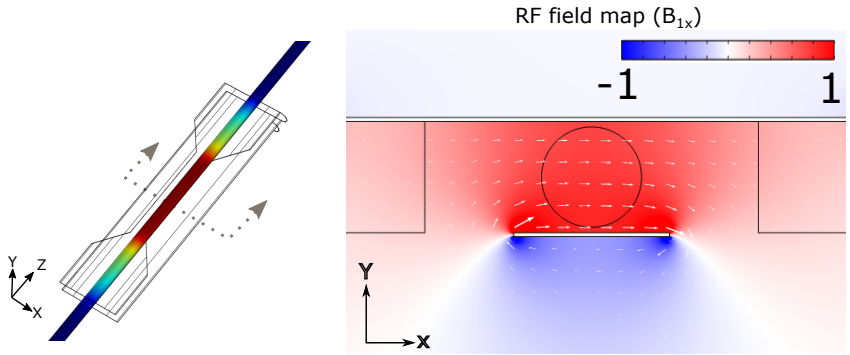

Figure 6.2: Comsol simulation result of the stripline's radiofrequency field map at 650 MHz over the central cross-section. The sample capillary is indicated as a black circle, placed where the radiofrequency field is most uniform.

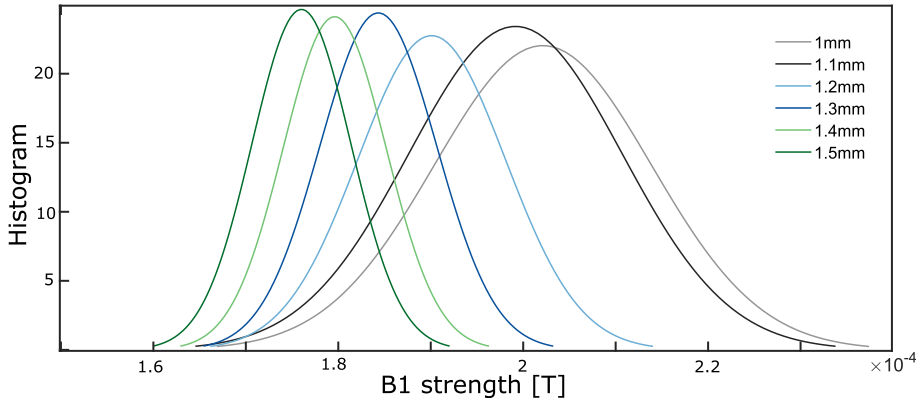

Figure 6.3: Simulated B_1 field uniformity for different stripline widths. The B_1 histogram was plotted from all the mesh elements of a circular capillary placed above the stripline. The simulation of B_1 is conducted using the RF module in COMSOL Multiphysics.

To check the viability of the fold-up stripline as an NMR detector, the first important thing is the B_1 performance, specifically whether the upper arm creates a localized B_1 distortion. Therefore, we conduct a FEM simulation on a case shown in Fig. 6.1, using the lumped-element model. A lumped port of 1 V was defined in between two grounds. The sample capillary is placed at the center where the RF field is most uniform. The resulting B_1 field map is shown in Fig. 6.2. As expected, along the Z axis, the coil shows a stronger field on the narrow part of the stripline due to higher current density and without noticeable field distortion from the arm. On the cross-sectional plane, the B_1 field (B_{1x}) is mostly uniformly distributed and concentrated between two metal layers.

Bart et al.[82] demonstrated that the gap of the stripline coil to contain the sample achieves better B_1 uniformity when the gap is smaller than the width of the narrow part of the stripline coil. In light of this, and considering a 1 mm gap distance, we conducted simulations with various widths of the fold-up stripline, ranging from 1 to 1.5 mm. Subsequently, we post-processed the B_1 strength acquired from each mesh element of the simulation model. The resulting histogram is depicted in Fig. 6.3. It was observed that B_1 uniformity improves with a higher width of the stripline, albeit with a trade-off in B_1 strength.

As indicated by the SNR figure-of-merit in NMR, the impedance (Z = R + jX) of an NMR coil is a critical electrical characteristic directly influencing excitation efficiency. An ideal NMR inductor (L) would exhibit nearly zero resistance and zero capacitance, ensuring minimal thermal noise and an exceptionally high self-resonance frequency. However, achieving this ideal coil is typically unattainable in the real world, as each coil inherently possesses parasitic resistance and capacitance, resulting in self-resonance (LC) with its self-capacitance.

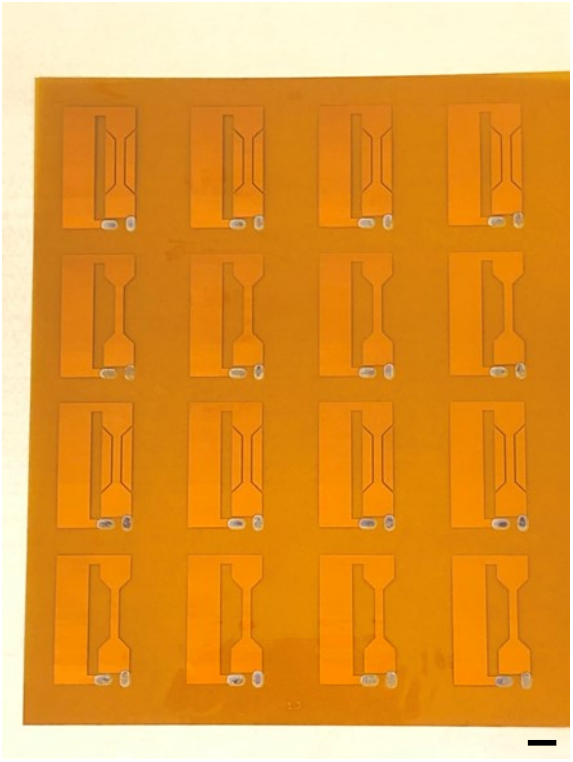

Figure 6.4: an array of fold-up stripline coils ordered from a vendor (MultiPCB, China) before folding. The coil consists of three sandwiched layers: 25 µm PI cover layer, 18 µm copper traces, and 25 µm PI substrate. (scale bar: 5mm)

The self-capacitance (C) and self-inductance (L) of the RF coil collectively determine the self-resonance frequency (SF = $1/2\pi\sqrt{LC}$). This is particularly relevant for structures like the stripline coil, characterized by a large surface area and a small separation distance from the ground plane. The significant self-capacitance, in combination with its inherent inductance, shifts the self-resonance frequency to a lower range. This is attributed to the expectation that the self-capacitance of a closely spaced stripline is likely to be larger than that of a typical solenoid coil with comparable dimensions.

Drawing from the aforementioned simulation outcomes and design considerations, multiple fold-up striplines of varying dimensions were manufactured on a flexible Polyimide substrate with a thickness of 25 µm, ensuring sufficient flexibility, as depicted in Fig. 6.4. Afterward, we conducted a comparative analysis of the electrical characteristics of the striplines, including those with and without side wings and narrow parts measuring 1.3 mm or 1.4 mm in width. These coils were then folded up to a spacer with a 1 mm distance and directly soldered with SMA connectors for impedance measurement. The measurement results, presented in Fig. 6.5, reveal that the inclusion of additional side wings downwardly shifts the self-resonance frequency by approximately 0.1 GHz. Furthermore, the strip with a 1.4 mm width is anticipated to exhibit a higher self-resonance frequency. The coil

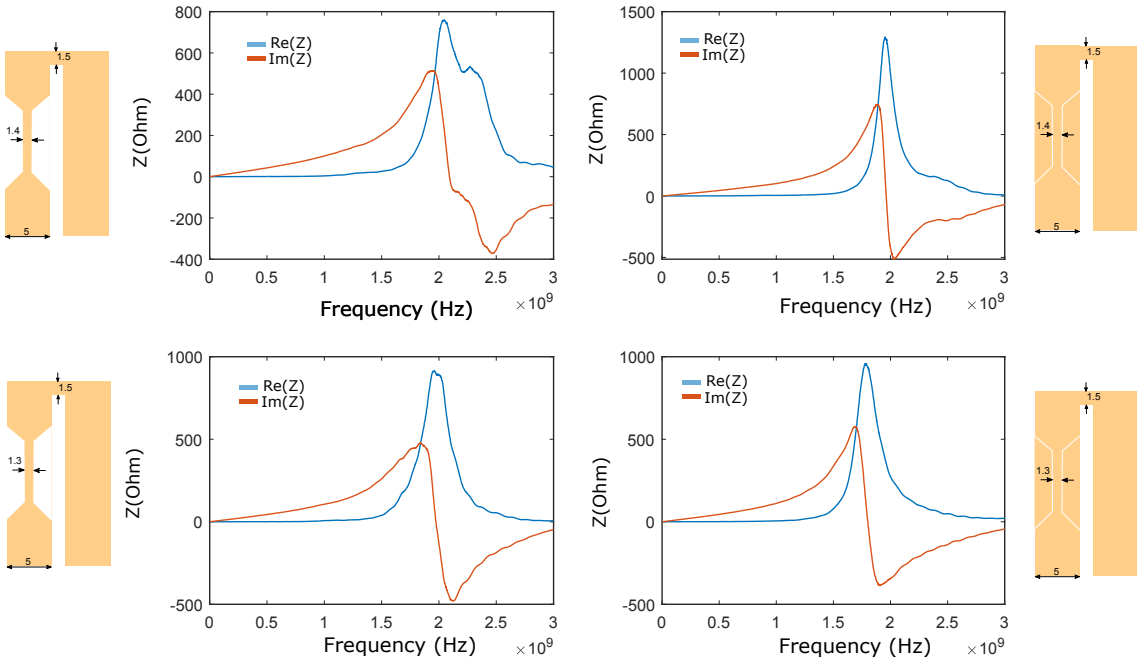

Figure 6.5: (a) Impedance curve of the fold-up stripline coil with respect to different frequencies, ranging from 0 to 3 GHz. Upper left: the width of the narrow part is 1.4 mm. Lower left: the width of the narrow part is 1.3 mm Upper right: the width of the narrow part is 1.4 mm with additional side wings. Lower left: the width of the narrow part is 1.3 mm with additional side wings.

with a 1.3 mm width of the narrow part and side wings demonstrated a Q factor of 42 at 650 MHz and an exceptionally high self-resonance frequency of 1.75 GHz, rendering the coils suitable for various commercial field magnets with frequencies below 1.5 GHz.

Circuit tune and match

Ensuring proper tuning and matching is crucial as it can enhance the sensitivity of the receivers and, consequently, reduce the averaging time for spectrum acquisition. One critical challenge in the design of the RF circuit for the fold-up coil lies in its inherently low inductance, as indicated by the impedance curve. To determine the required capacitance for a 650 MHz field magnet, we employed ADS optimization to identify a suitable value for designing our NMR probe. A common practice for NMR RF coil tune-and-match involves using a two-element L-section matching network, with one element for tuning and the other for matching. We adapted this approach to accommodate the low inductance of the stripline coil.

In Fig. 6.6a, the schematic of the electrical circuit in the NMR probe is depicted. C1 represents a pre-tune capacitor, positioned in close proximity to the coil. Trimmer capacitors C3 and C4, with a tuning range from 1 to 10pF, are utilized for tuning. Cp acts as a parasitic

capacitor to bridge the two trimmers. Additionally, consideration must be given to all parasitic inductive effects (Lp1 to Lp4) of the traces, encompassing those associated with placing the trimmers and extending the coils to the external circuit, as their size is typically comparable to the primary stripline coil.

To facilitate multi-nuclei parallel experiments, we optimized the values of the pre-tune capacitors (C1=3.5 pF) and (Cp=1.2 pF). This allows the coil to be tuned not only to the proton frequency but also to other frequencies, such as ^{19}F. Fig. 6.6b illustrates the tuning range of the circuit, spanning from 675 MHz to 575 MHz, while the matching capacitance ensures a -30dB RF reflection loss.

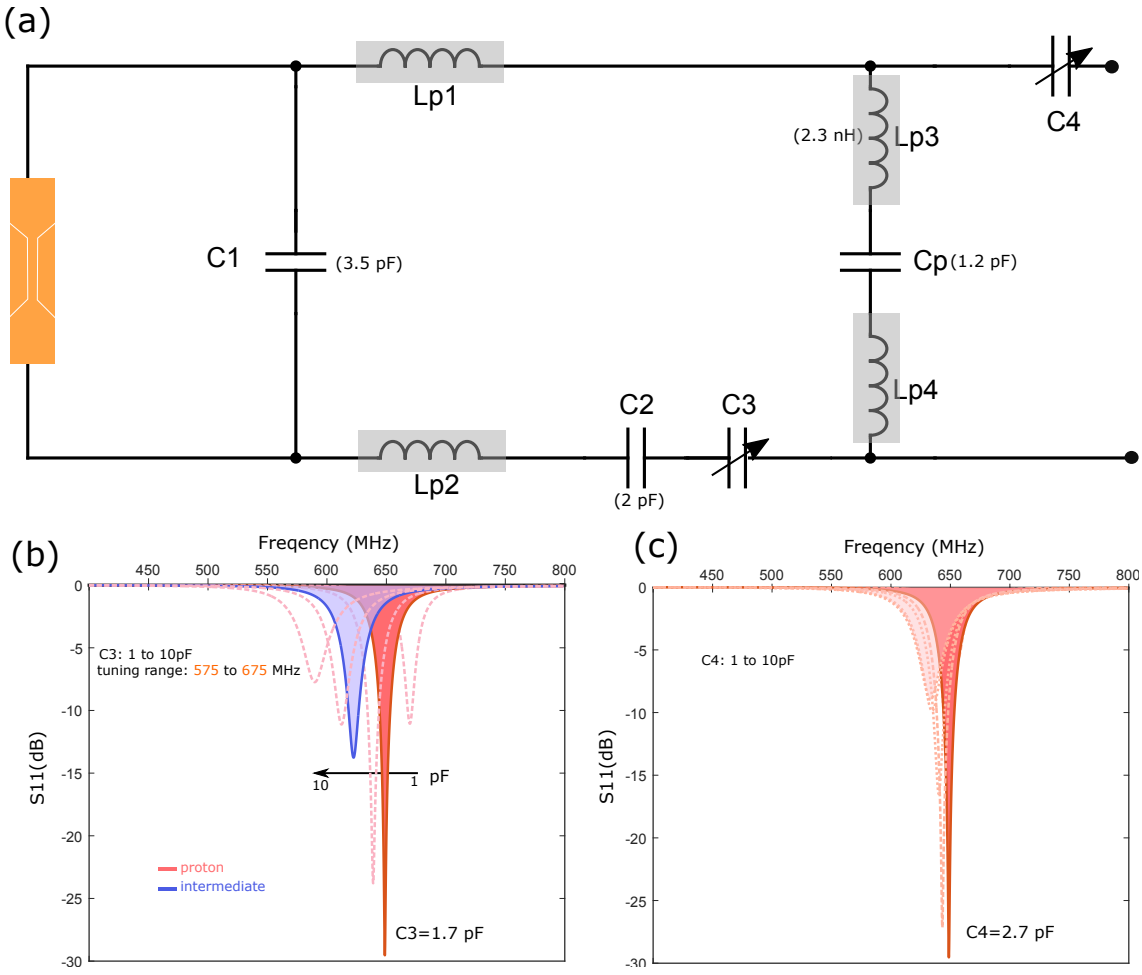

Figure 6.6: (a) Schematic of the equivalent circuit diagram for tuning and matching of fold-up coil. (b) Simulated tuning curve (S11) of the coil. C3 ranges from 1pF to 10pF. (c) Simulated tuning curve (S11) of the coil. C4 ranges from 1pF to 10pF.

6.1.2 Spatial inhomogeneity at high field motivated local shim design

As existing shim systems typically employ more than 20 SH shims to achieve satisfactory linewidths for diverse sample shapes, adapting such a system directly for localization introduces significant complexity to the probe head design. Specifically, the number of shim coils scales linearly with the number of RF coils present, and for a setup involving two samples, this would entail 40 shims, which is impractical. Therefore, there is a strong need to reduce the number of shim coils.

The distortion of the magnetic field on the sample is contingent on the sample's geometry within the sensitive region, arising from the magnetic susceptibility mismatch with its surroundings. In the case of a purely spherical-shaped sample, the field profile can be decomposed into several orthogonal pure SH functions. Based on the SH profile given in Fig. 2.7, we assume that the B_0 distortion in specific sample shapes has a higher weight function to some specific terms, and therefore field distortion can be simplified into a few terms. If this assumption holds true, we can tailor the distortion to be manageable by a minimal number of local shims. This approach facilitates shim system design without the need for a complex, multi-layered shim structure.

For example, a very high aspect ratio of sample volume is a 2D analogue of a wire, and we would expect the inhomogeneity of the high order SH function on the coronal slice to be negligible. This allows a reduction of the necessary amounts of shim coil to, especially for parallel shim arrays. We executed a B_0 simulation with COMSOL. The result shows that the majority of in-homogeneity comes from the Z direction, with up to 3000 Hz field differences, as seen in Fig. 6.7b. On the cross-sectional plane, it shows it is almost linearly distorted on the X-Y plane (500 Hz). The static magnetic response of the NC to B_0 field to reveal the B_0 homogeneity was performed with a 15.2 T magnetic flux density with an error tolerance of 10^{-3} ppb. The total number of mesh elements is 199k (Fig. 6.7a).

Meanwhile, we experimented with this assumption by putting two high aspect-ratio capillaries (2.4 mm x 40 mm) with two different samples in the magnet's isocenter to map the spatial field distortion. Sample dependent B_0 inhomogeneities in the parallel NMR experiments were demonstrated with the following B_0 map experiments. The experiments are performed on a 15.2 T ultra high field magnet(Bruker, Ettlingen, Germany) with a commercial probe equipped with a 35mm diameter birdcage coil tuned to 650 MHz for ^{1}H nuclei. The active length of the birdcage coil is 40 mm. Water and Isopropanol are used as samples inside a test tube of 2.4 mm inner diameter, and placed off-centre of the z-axis at a 30 mm distance from each other. B_0 map experiments have been carried out

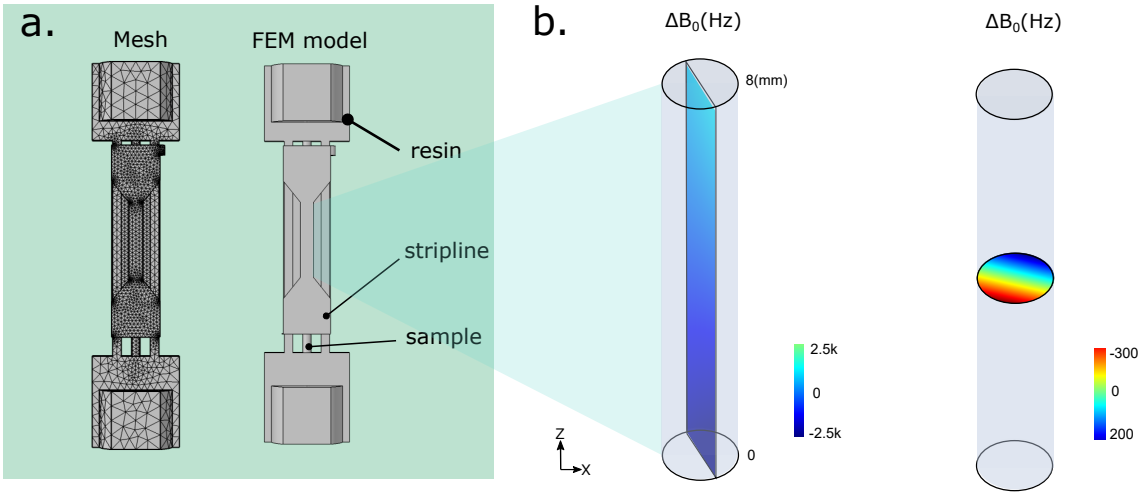

Figure 6.7: (a) CAD model of a stripline coil folded on a resin based support imported to COMSOL for FEM simulation. Magnetic susceptibility of each components are: $\chi_{resin} = -5.39x10^{-6}$,$\chi_{copper} = -9.63x10^{-6}$,$\chi_{water} = -9.05x10^{-6}$. (b)Simulated B_0 field map of Coranal and Transverse plane across a (1 mm OD X 8 mm) sample.

with a standard *FieldMap* sequence available with Paravision(Bruker, Ettlingen, Germany) software. We obtained a field map with a spatial resolution of 64x64x200 axial slices, over a field of view of 10x10 mm^2, repetition time of 35 s, and acquisition time of 7 minutes and 28 seconds for one experiment.

The B_0 map of the central axial slice of the two samples (2.4 mm ID x 40 mm, aspect ratio = 16.6) before and after automatic linear shimming is shown in Fig. 6.8. The mean ΔB_{0_z} of each axial slice is calculated and plotted for the 200 slices, which shows the coronal B_0 field variation with a characteristic higher order B_0 inhomogeneity. It is visible from the central axial slice that both samples had different ΔB_0 before shimming. B_0 inhomogeneity reduces after the automatic linear shim in the case of water sample, but it does not improve for Isopropanol. This occurs because the automatic linear shim algorithm is based on the narrowing of the FWHM of the 1D reconstruction of the signal and optimizing the area under FID, which is biased toward the signal with maximum intensity. This finding validates the fact that global shim is insufficient for shimming multiple samples. Meanwhile, the field exhibits a comparable pattern to the simulation outcome, indicating that the primary source of distortion originates from the SHs of X, Y, Z, and higher-order zonal functions. This observation motivated us to develop a shim set encompassing these terms.

Based on the above B_0 mapping results, we can conclude the following points:

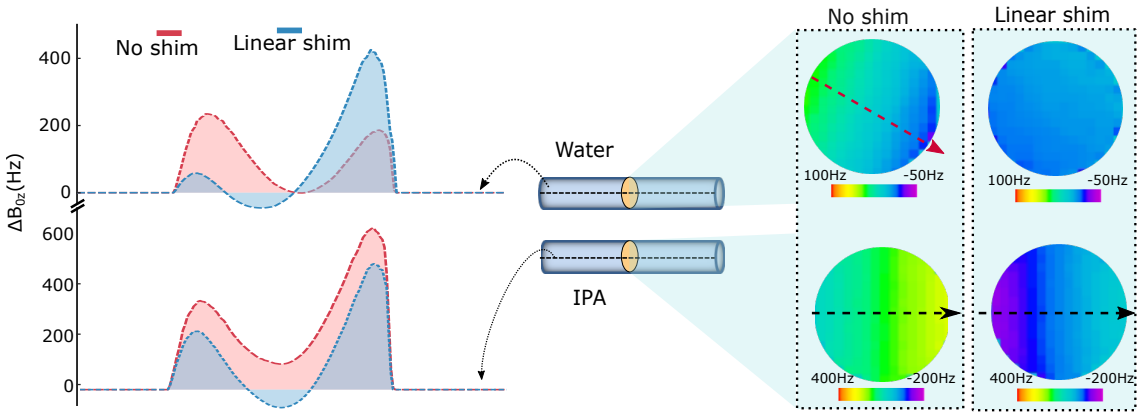

Figure 6.8: B_0 field map (Coronal and Transverse plane) acquired from a standard FieldMap sequence. Both samples (Water and IPA) are stored in a 2.4 mm glass capillary and located off-center with 30 mm distance.

- The spatial field distortion for an un-shimmed case is around the range of $\pm$ 100 Hz to 400 Hz, corresponding to $\pm$ 2.3 µT to 9.2 µT
- Due to the nature of SH harmonic shims, the global shim set is optimized for one coordinate, and not ideal for two coordinates.
- The on-plane distortion (X,Y) is less dominate compared with the zonal direction, and it's highly linear, implying the decomposition of the intrinsic field map is mainly composed of X, Y, Z, Z_2, Z_3, Z_4.
- The B_0 field map experiment consider the sample's magnetic susceptibility. The two samples show two similar B_0 field profile trends on the Z axis but different on the X-Y plan.

Based on the above findings, our objective is to create a pragmatic shim set for integration into an array designed for our customized stripline coil. Adhering to the NMR cell concept, where the sample-centered shim coil follows a SH configuration, each local shim set rectifies the field discrepancies to the coordinates defined by the sample. It is worth noting that we have determined to set a current limit, maintaining it below 300 mA, in order to avoid the utilization of high-current drivers.

Initially, when shrinking the RF coil size, careful consideration is necessary when selecting the dimensions for the shim coil, taking into account the sensitivity of the shim. As the sensitivity is directly proportional to the diameter of the shim coil, a smaller diameter for the sample-centered shim set generates a more potent correcting field with the same current input. The miniaturization of shim coils poses a challenge, especially given that most SH

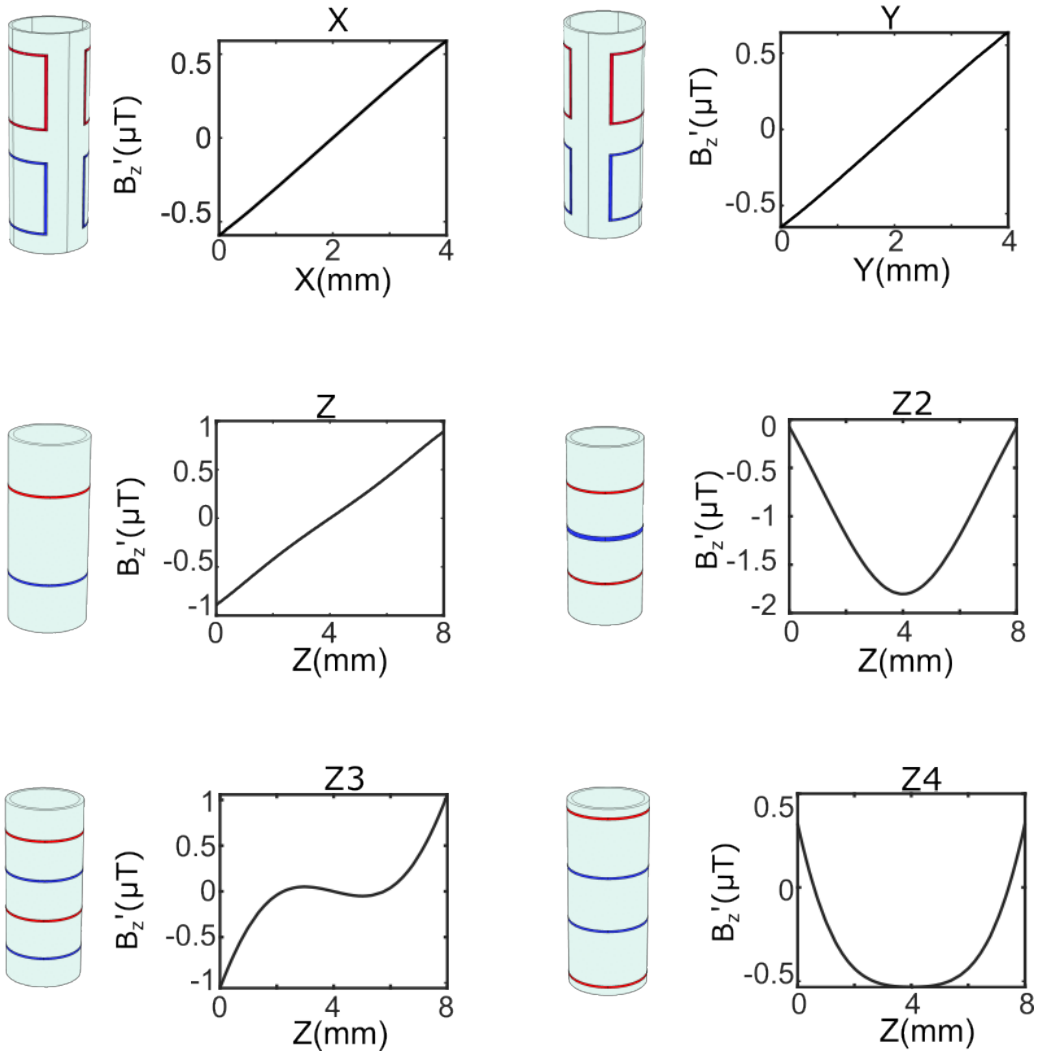

Figure 6.9: Correcting field profile (B_z') over the sample region of interest generated by local SH shims, corresponding to the X, Y, Z, Z_2, Z_3, Z_4. The value of the current was set to 10mA. The number of turns from top to bottom for each shim is: X(1,1), Y(1,1), Z(1,1), Z_2(1,2,1), Z_3(4,1,1,4), Z_4(9,1,1,9)

shim coils are typically designed as multi-looped structures. Nevertheless, as the number of shim coils increases, the fabrication process for the shim set becomes more intricate.

We have made modifications to a pair of SH shims, drawing inspiration from the same example featured in Chapter 3 and the article by Roemer et al. [11]. This decision was guided by the simplicity of the construction and the aim to maximize the desired gradient field. Through finite element method (FEM) simulations, we verified that these modified shims could be wound onto a cylindrical surface while retaining ample shimming capabilities. The shimming profile, denoted as B_z' , is illustrated in Fig. 6.9. Each looped coil is assigned a 10mA DC current, with different colors representing the current direction

(blue for clockwise, red for counter-clockwise). It is evident from the figure that the 2D shim profile of each shim coil serves as a representative model of SH expansion.

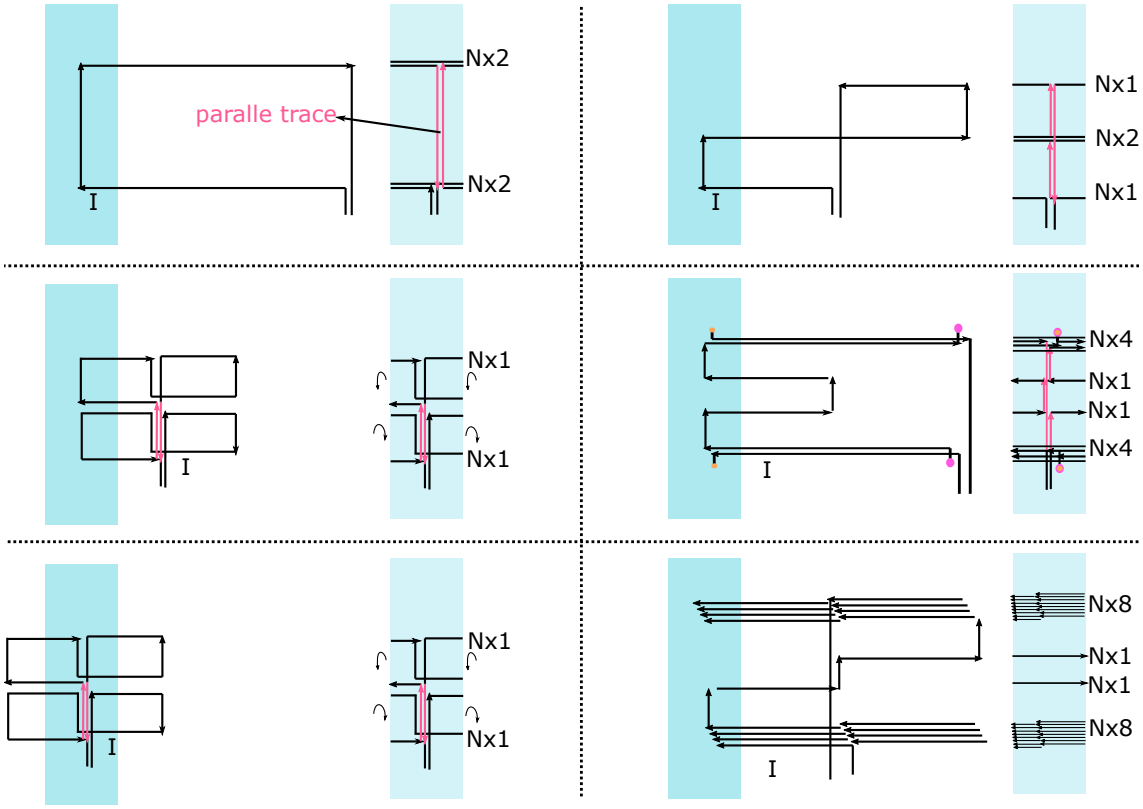

Figure 6.10: Schematics of the customized shims, corresponding to the Z, X, Y, Z_2, Z_3, Z_4, rolled to a cylindrical support. The traces are represented by the current vector. The number of turns for each shim is: Z(2,2), X(1,1), Z(1,1), Z_2(1,2,1), Z_3(4,1,1,4), Z_4(8,1,1,8).

Typical shim coils found in commercial NMR systems are often large enough to be directly wound with copper or superconducting wires. Therefore, the machine-wounded method is not ideal for small shim coils due to manufacturing errors. We utilized print circuit broad technology. The shim structure given in the simulation is discrete, so it is necessary to connect each loop of the coil to form a circuit. Nonetheless, enabling all the shims to form on one flexible substrate, the vias and traces for connecting the shim structure needs to be carefully arranged to avoid high-order distortion components. Fig. 6.10 depicts the layout of X, Y, Z, Z2, Z3, and Z4 shim coils unrolled from a planar substrate (left) to a cylindrical support (right). Here, N represents the number of turns. To address the issue of connection wires, we positioned the two connecting conductors (pink) closely in the vertical direction (Z). The vertical current direction creates a field stream on the X-Y plane. Since the parallel vertical traces have opposite current directions, the magnetic field is effectively cancelled. Owing to the necessity of more looped coils on the two sides of high-order shims, a one- or two-layered PCB is insufficient for vias and a significant

amount of parallel traces. We plotted the layout of the shim structure on a three-layered single substrate, as seen in Fig. 6.11.

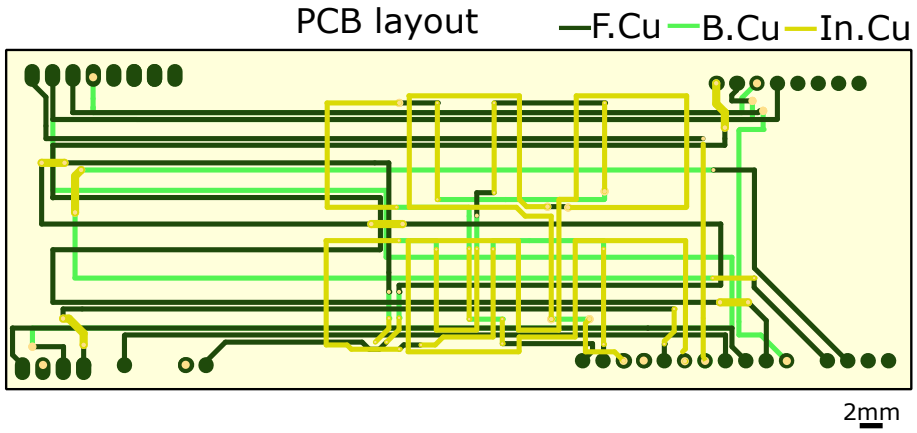

Figure 6.11: PCB layout of our customized local shim structure (X,Y,Z,Z1,Z2,Z3,Z4). PCB is a three-layered metal flexible PCB. (F.Cu: front copper layer, B.Cu: bottom copper layer, In.Cu: intermediate copper layer)

6.1.3 Constant current source

To efficiently manage high current (>100 mA)distribution within each shim coil, it is imperative to design effective shim drivers capable of providing multiple current outputs. Commercially available power supplies are typically limited in the number of output channels. Also, they are designed for a broader current output range, making them excessively powerful but expensive for our local shims. To address this, we established specific requirements:

- **Current Channels**: Given the necessity of acquiring spectra from four RF coils, each requiring six current inputs, we require at least 24 independent current channels.
- **Precise Bipolar Output Currents with Low Drift**: Ensuring stable spectra over the course of experiments is essential. Thus, the shim drivers should provide precise bipolar output currents with low drift (±0.1 mA).
- **NMR Compatibility**: Due to the sensitivity of NMR coils to environmental noise and the close proximity of the shim coil and RF coil, it is crucial to avoid introducing additional RF noise from the drivers. The shim drivers should be designed to be shielded and NMR-compatible.

To achieve multiple channels of DC current output with low drift (±0.1mA) within the range of ±200mA, we employed an enhanced Howland current pump with a buffer (Fig. 6.12).

This design incorporates two cascading operational amplifiers for improved performance [111]. We take advantages of the multiple analog outputs from the 96-channel 12-bit DAC evaluation module (DAC60096, Texas Instrument) and each output is directed to a current pump. The use of a commercial DAC board facilitates digital control of the output voltage. The circuit benefits from a feedback loop, ensuring a stable current with minimal drift and error. Additionally, the voltage across OP1 can be programmed by the DAC module and subsequently converted to current by OP1. The current is then amplified by the second operational amplifier with a gain of R2/R1=10. The feedback loop establishes a high output impedance, mitigating current errors arising from resistors. The power drive operational amplifier is linked with two parallel capacitors (C1 and C2) to reduce common mode noise.

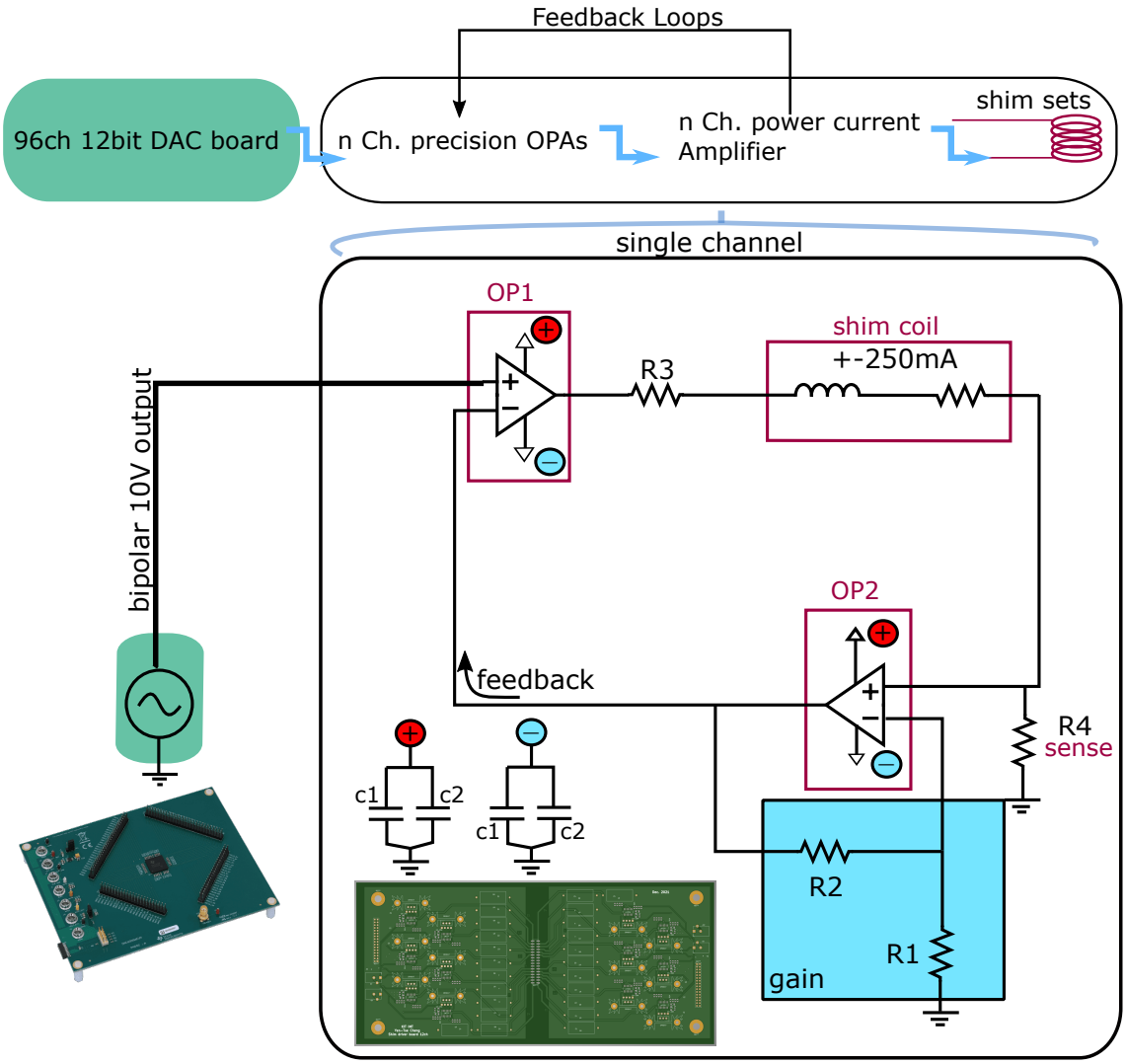

Figure 6.12: Schematic of the constant shim current source and the single-channel DC current generation based on cascaded operational amplifiers. The CAD layout of the current amplifier is included.

In theory, the current pump circuit should be capable of addressing the challenge of parallel shimming drivers, although there is limited available data on such a circuit specifically designed for NMR shimming. A test board on a PCB featuring a single Howland current pump was constructed. The input voltage can be adjusted and supplied from an external DAC board. The amplified current is then directed to the local shim set on the low-field NC-based parallel probe designed for a 1.05T field magnet. All shim wires are shielded to prevent the capture of external RF noise. The experimental setup is depicted in Fig. 6.13a. The results of shim-on and shim-off, as illustrated in Fig. 6.13b, demonstrate that the ^{1}H spectra of water can be shimmed effectively, reducing the linewidth from 120 Hz to 30 Hz without introducing additional noise. Also, it's noteworthy that the fluctuations in the DC output current are minimal, measuring below 0.1mA, corresponding to less than 0.1 Hz FWHM fluctuation.

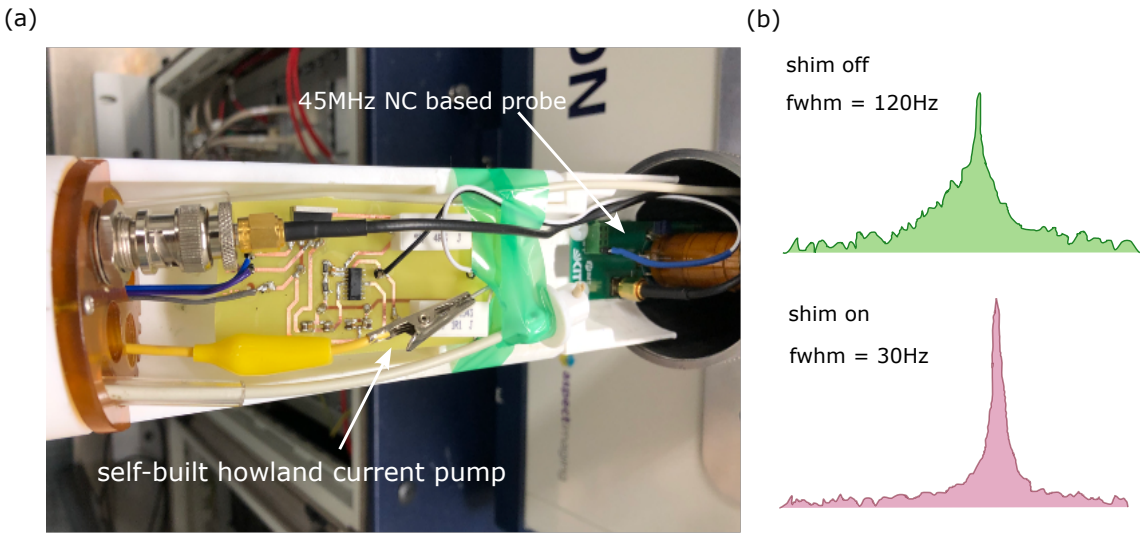

Figure 6.13: (a) A setup indicating a signal channel self-built howland current pump utilized in the low field NC-based parallel probe. The current pump is connected to the Z shim. (b) Shim-off and shim-on proton spectrum of pure water.

In Fig. 6.14a, the 24-channel shim driver circuit board is depicted, with efforts made to minimize the size of each amplified circuit. Given the requirement for high current output within the range of ±200mA, the power operational amplifier is equipped with a heat sink, and power resistors (5W) are employed as sense resistors to ensure low resistance drift. Each layer comprises a total of 12 shim channels and can be stacked vertically as needed. The gain can be adjusted using the ratio of two resistances, with a chosen value of 5 in our case. The V-I curve is presented in Fig. 6.14b. This setup facilitates bipolar current output (±100 mA/V).

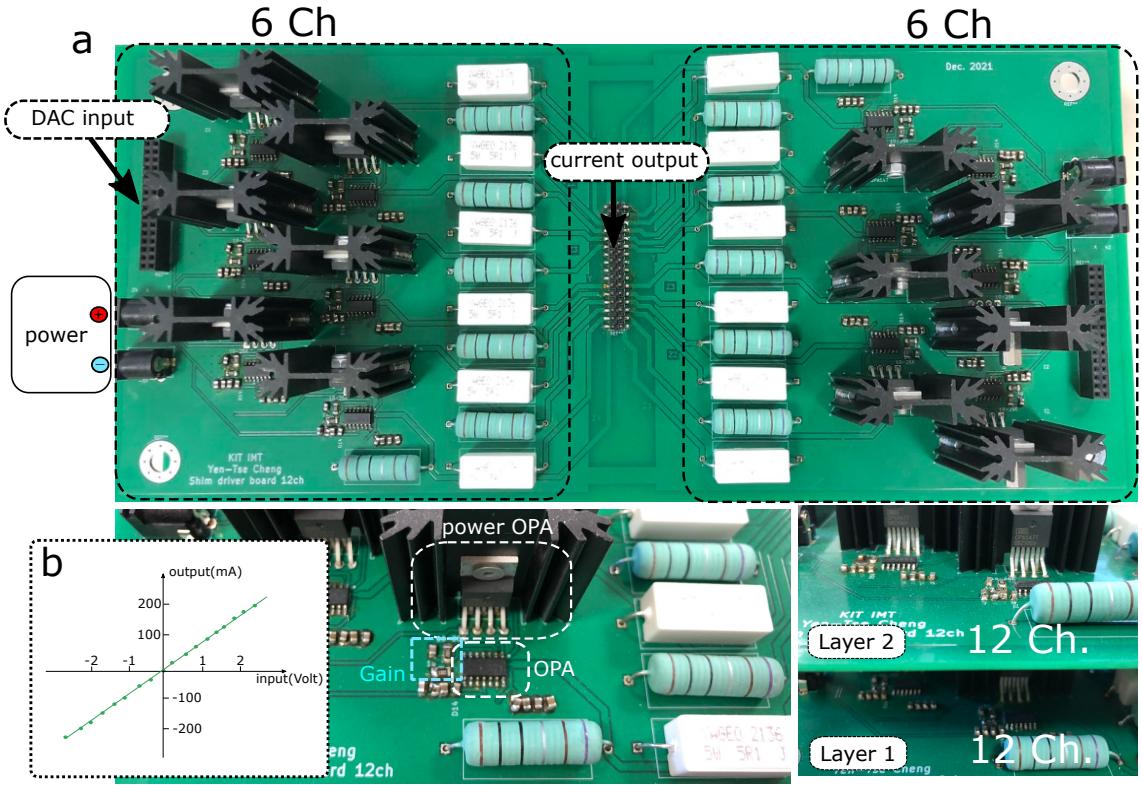

Figure 6.14: (a) Photo of the assembled 24 channel shim driver circuit based on the howland current pump for shimming applications. Each layer has 12 shim channels and can be vertically stacked to expand the number of current outputs where appropriate. (b) V-I curve of the DAC voltage input and current output. They are linearly correlated.

6.1.4 First version of four channels parallel probe

Here, we introduce a 4-channel probehead (Fig. 6.15a,c) utilizing the fold-up stripline designed for a 15.2 T MRI horizontal magnet. The aim is to maximize the number of NMR measurement sites within a single probehead. As a preliminary design, we initiated with a four-coil array. Although the inclusion of additional shim coils occupies space for more RF channels, it remains necessary, as discussed in Chap. 3.

Adhering to the NC concept, we modified and downsized the previous NMR cell, from a 5 mm sample handling tube to a flat 5 mm x 1 mm capillary supporting the folding of the stripline coil, see Fig. 6.15b. To ensure the ideal location of the NMR sample at the narrow part of the stripline, we designed a three-layer sample-holding chip. This chip comprises a PLA base substrate, a cut flow channel (PLA), and a top subtract (PLA) for open holes. The 1 mm-wide flow channel is laser-cut, and the three layers are thermally bonded in an oven at 80 °C for two hours. The thickness of each PLA layer from top to bottom is: 200 µm, 600 µm, 200 µm.

To account for the extended wire required to connect the RF coil to the tank circuit, a pre-tune circuit is included in proximity to the stripline coil, minimizing unwanted parasitic inductance from the wires. Given our prototype's focus on the ability to perform parallel experiments simultaneously from four NMR cells, targeting the same or different nuclei, we evenly distributed them on-site. Each NMR cell is equipped with two trimmer capacitors (1 to 10 pF) for tuning to proton and fluorine frequencies.

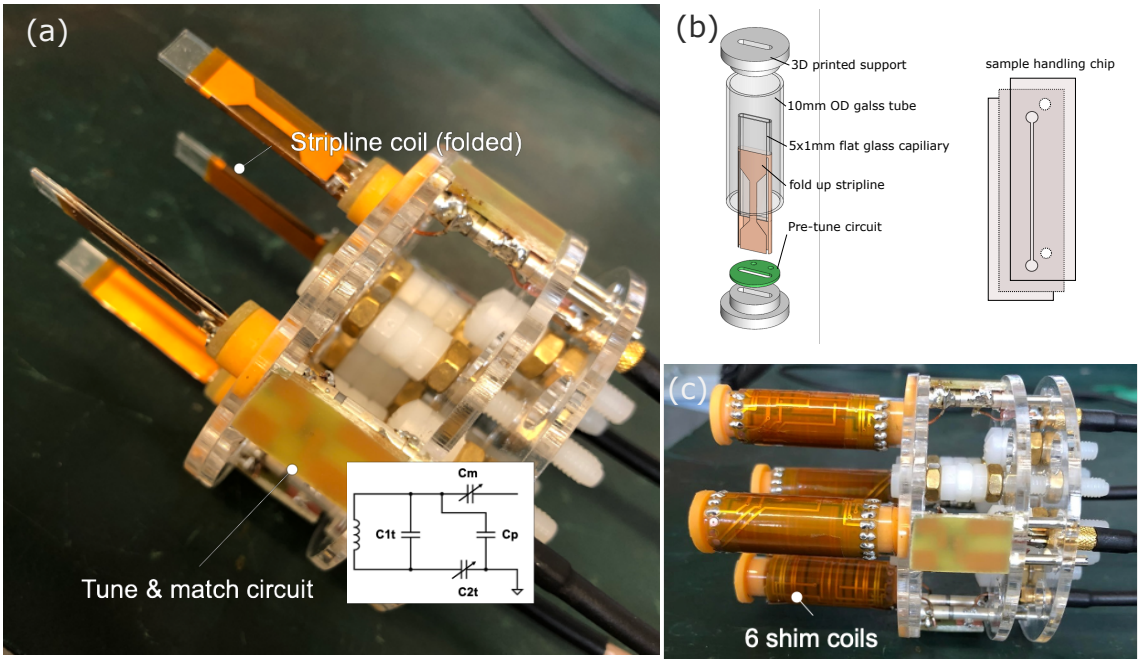

Figure 6.15: (a) Custom-built four channels stripline probe. All the striplines are misaligned with each other for RF decoupling. (b) CAD schematic of the unit stripline based NMR cell. (c) Four channels stripline parallel probe with custom-built shims.

Before commencing a formal NMR spectroscopic experiment, addressing RF coupling issues is essential. Following the misalignment technique concept, the four NMR cells are orthogonally misaligned to each other, as discussed in Chapter 3. Each coil is meticulously tuned and matched to the proton frequency, achieving an S11 below -20dB. Fig. 6.16 presents the measured S parameters (S_{ij}, $i\&j \in [1,2,3,4]$). The inter-coil couplings S_{ij} are in the range of -20dB to -50dB, ensuring acceptable RF signal isolation.

For NMR spectroscopy, we prepared two samples (5 mM sucrose in PBS solution and DI water) and conducted simple NMR single pulse experiments to assess the intrinsic linewidth. Firstly, we tuned and matched the RF coil to a 650 MHz frequency. Fig. 6.17a presents the tune and match curve, displaying a reflection coefficient (S11) of approximately 2%, which can be fine-tuned using mechanical trimmers. Subsequently, we placed droplets of the samples on the sample handling chips through capillary effect, sealing them with adhesive tape. The chips were then inserted into the flat capillary, ready for measurement.

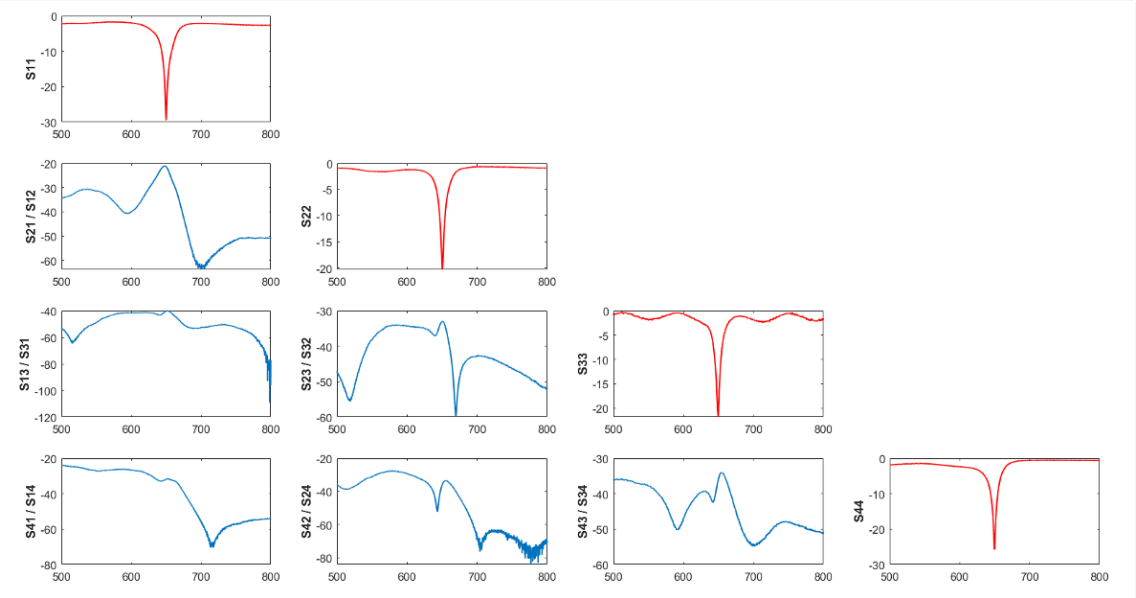

Figure 6.16: (a) S parameters of 4 coils array probe.

Fig. 6.17b,c depict the single pulse ^{1}H spectra of two identical samples. The intrinsic linewidth of sucrose, linearly and globally shimmed properly, is only around 50 Hz, while for DI water, it is around 70 Hz. Despite this, a reasonable SNR of 350 was observed for DI water. Several factors that might affect the intrinsic linewidth or impose limitations on our custom-built probehead are listed below. First, misalignment of the chip to the Z-axis could be a contributing factor, as the current design does not allow for proper alignment of the flat capillary to the Z-axis. Second, the low surface uniformity on the wall of the cut channel through laser cutting may cause high-order local B_0 distortion. Additionally, the proximity of the flow channel to the PLA layer can contribute to field nonuniformity. Third, the sample chip may not be ideal for long-term experiments due to its size, and inadequate sealing may lead to small bubbles entering the sample channel.

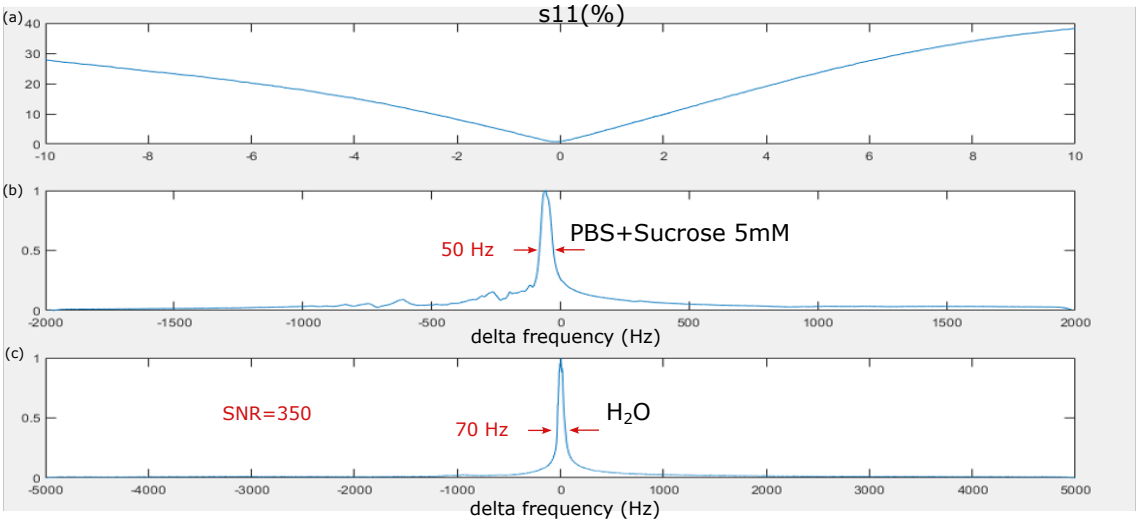

Figure 6.17: (a) S11 curve of the RF coil acquired in the spectrometer. The central frequency is at 650 MHz (b) ^{1}H spectrum of PBS and 5 mM sucrose solution (c) ^{1}H spectrum of DI water.

6.1.5 2nd version of two channels parallel flow probe

Addressing the limitations of the first version of the 4-coil probe, we have modified the unit NC to adapt it for continuous/stop flow NMR applications. We have developed a 2-Ch parallel probe, see in Fig. 6.18a. This design has same basic components, including RF coils, field correction coils, but coil support and sample handling chip are replaced with 3D printed support and glass capillary. The two RF coils were positioned and aligned with the static magnet field (Z) to generate RF fields perpendicular to it, like the first version parallel probe. The probe also features two inlet and two outlet ports for fluidic tubing, allowing continuous high-throughput screening measurements [27]. Sample inlet and outlet ports are connected to the top and bottom of the NC and securely connected to the pre-insert sample-handling glass capillary to prevent background signals from the tubing.

The construction of the parallel probe head proceeded as follows: First, the flexible PCB containing the shim and RF coils was procured from a vendor (multiPCB, Germany). A 700µm glass capillary (VitroTubes, VitroCom) was inserted into a 3D-printed support. Both coils were affixed to the supporting structures using instant glue (UHU Plus) and soldered to the tune-and-match circuit, incorporating high Q trimmer capacitors. All supporting structures were 3D printed in-house (PRUSA). The coil was carefully folded onto a 3D-printed support, aligned with a pre-designed frame with a thickness of 0.8 mm to mitigate susceptibility artifacts. A step-by-step depiction of the coil-folding process appears in Fig. 6.18b. A photo of the coil is seen in Fig. 6.18c.

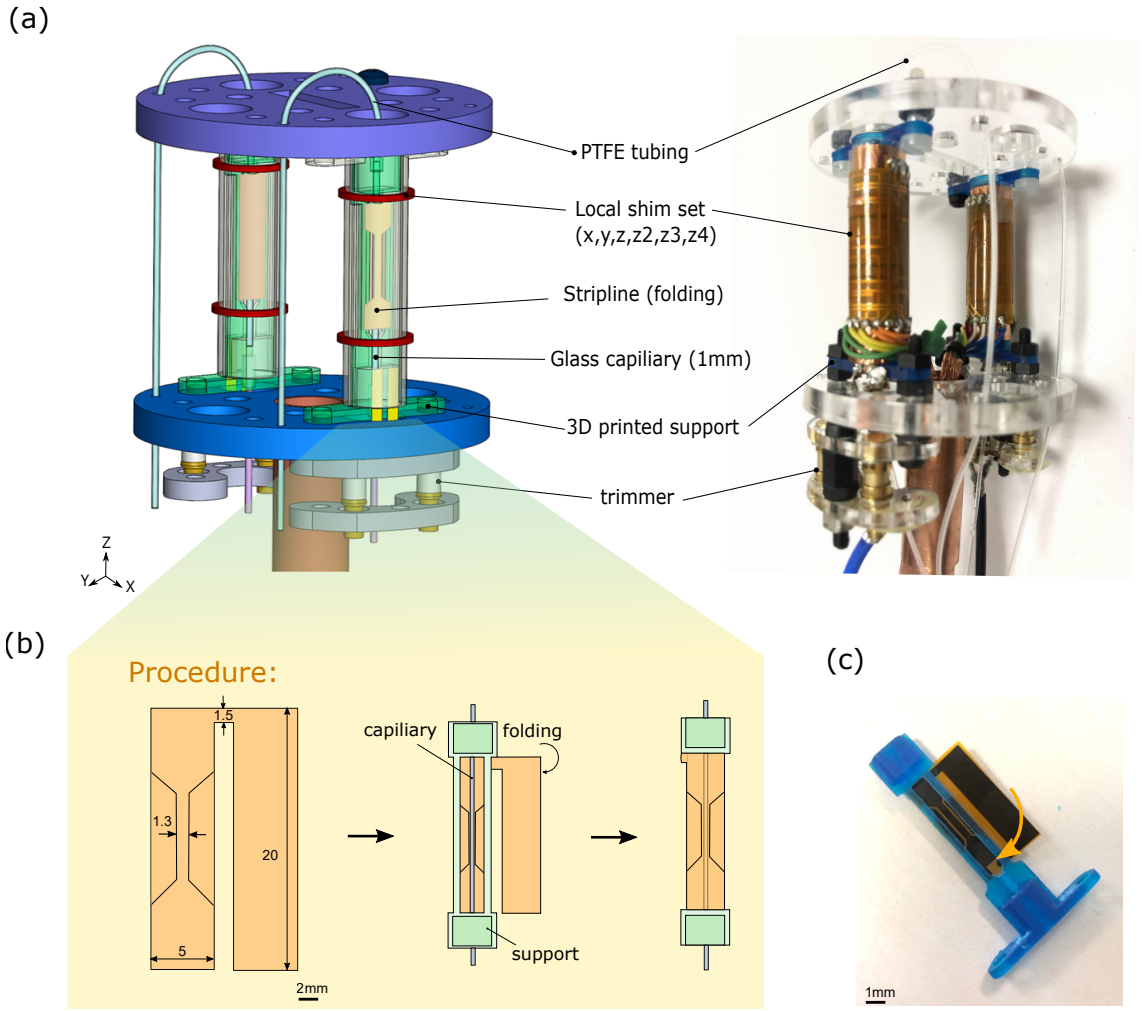

Figure 6.18: (a) A CAD model (left) and a photo of the probe head (right) (b) the schematic step-by-step procedure of folding the flexible stripline coil to a supporting structure (c) A photo showing the folding stripline coil to the support.

The background signal is a common issue because the RF coil catches the signal from the proton in the material used in the the probe. This problem usually results from improper design, for example, using the materials that causing strong susceptibility mismatch. The background signal's intensity is influenced by the proximity of these protons to the RF coils and their quantity relative to the proton concentration in the sample. In our NC design, the 3D-printed support is framed, to ensure a distance from the support to the sensitive region of the stripline coil. To evaluate this design, we compared two proton NMR spectra, one obtained with (90 v/v%) D_2O/H_2O and the other without a sample. The spectrum in Fig. 6.19 illustrates a significantly reduced signal acquired from protons in the probehead. Both channels were thoroughly examined.

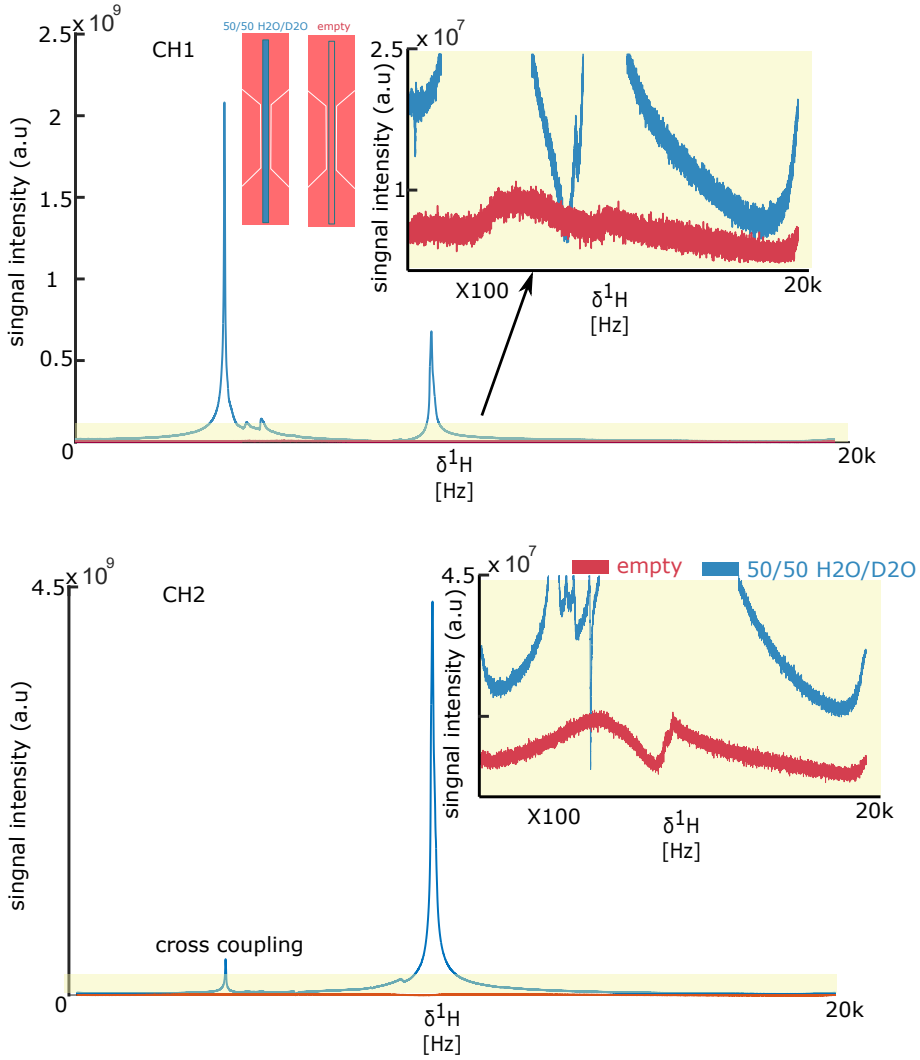

Figure 6.19: NMR signal intensity of the proposed NMR cell with 90 v/v% H_2O/D_2O sample filled (blue curve) and background signal (red curve). The upper plot figure is acquired in channel 1, and the lower one is in channel 2.

Fig. 6.20a presents the experiment setup of our parallel probe with the operating procedure shown in Fig. 6.20b. Operating the parallel spectroscopy probe starts with positioning at the isocenter of the horizontal magnet. The shim set is connected to a custom-built shim driver capable of accommodating bipolar 200 mA for each channel. Then, The samples are transferred to the sensitive region of the stripline coil through the PTFE tube, allowing subsequent parallel NMR detection (Fig. 6.20c).

In the next section, we report the shimming results of our parallel probehead, including shimming stability for a long experiment time (in days), shimming performance compared with global shimming.

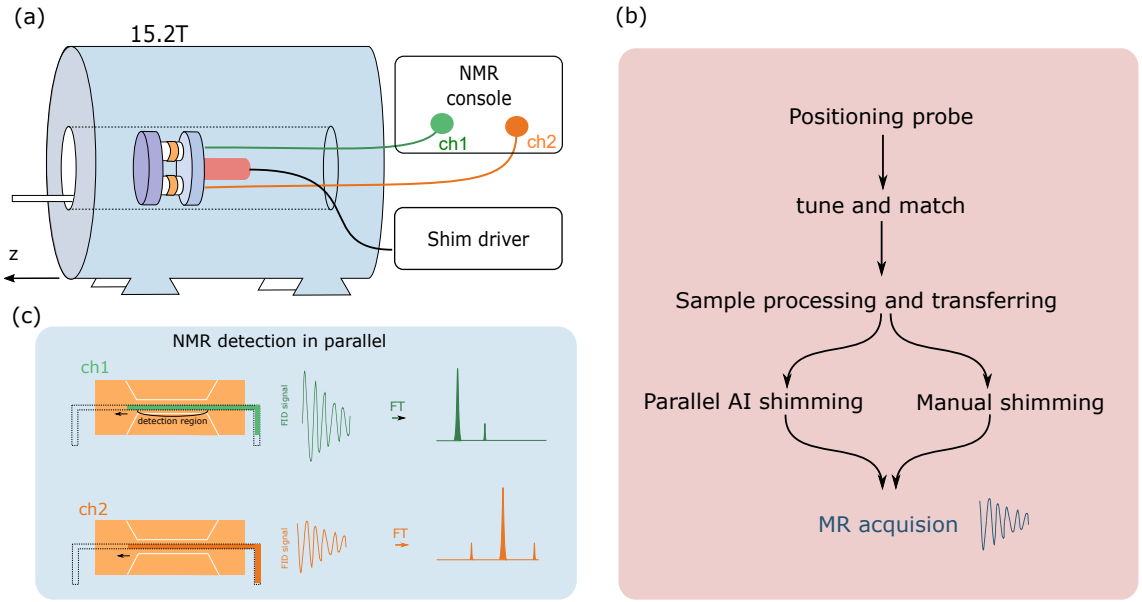

Figure 6.20: (a) An overview schematic of the experiment setup for parallel nmr spectroscopy utilizing a costume-built parallel NMR probe for 15.2 T horizontal magnet. (b) The procedure of operating the parallel probe starts with probe positioning, coil tune and match, sample processing and transferring, shimming (AI or manual), and MR acquisition. (c) NMR detection in parallel. Samples are transferred from outside the probe head to the narrow part of striplines and detected.

Usually, the shimming is done manually and takes up a lot of measurement time. Also, conventional automatic shimming is prone to having many redundant steps. Especially for an array of shims, the stray shimming field generated by the local shims couples to the others, and the experiment time exponentially increases with the number of NCs. Therefore, in the Sec. 6.2, we introduce an AI method to handle the shimming process. In short, a trained AI model is employed to predict the required shim current for each local shim channel.

Shimming preformance

Before delving into the heart of AI-driven shimming, we conducted an NMR experiment using different global and local shim values for two NCs. Drawing insights from Chapter 3, interpolation is an effective method for identifying the local optimal shim settings for two coils. However, the optimal spectroscopic resolution is not achieved. In this context, we adopted this approach and tested it in a 15.2 T magnet. The 650 MHz magnet is equipped with 20 global shims, providing adequate shimming capabilities. As depicted in Fig. 6.21a and Fig. 6.21b, the automatic linear shimming of one channel while leaving the other with up to a 200 Hz linewidth revealed that the spectrum exhibited more than mere linear distortions. This suggests the necessity of high-order local shims. With a moderate application of local shimming, both water spectra achieved a commendable linewidth (Ch1:

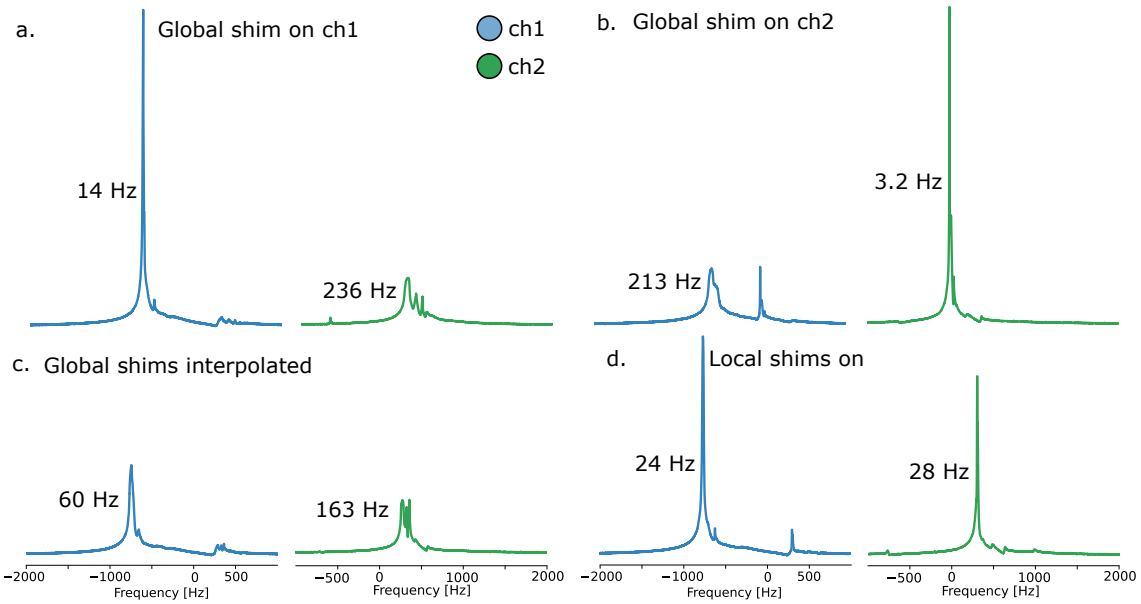

Figure 6.21: (a)+(b) Global automatic shimming of a single channel will leave the other channels with poor linewidths. (c) Interpolating the optimum shims will reduce both peaks' linewidths but not to spectroscopic resolution. (d) After mild (quick testing) local shimming, both channels show decent linewidths. The linewidths are measured on a Voigt-fit if the peak shows splitting. Both channels are filled with pure H_2O for comparison.

24 Hz/Ch2: 28 Hz). After manually high-order local shimming, an optimal linewidth, 4 Hz for Ch1 and 7 Hz for Ch2, can be achieved, seen in Fig. 6.22.

Besides, we also emphasized the stability when operating the local shim set, especially for a long-time experiment. Stability, in this context, refers to the consistency of the NMR spectrum over time without necessitating frequent adjustments to the current supplied by the power source. In prolonged operations, certain issues may arise, such as the displacement of the shimming coil, current drift from the power supply, and the joule heating effect on the coils. An ideal shimming coil or structure should not only exhibit robust shimming strength but also maintain a stable output of the shimming field.

Here we conduct a long-time single pulse ^{1}H experiment with both channels filled with pure water. Each channel is shimmed down to the optimal linewidth, globally and locally. Fig. 6.23 reports the shimming stability over two days. The report includes 160 reference-shimmed spectra, and every five reference spectra are averaged in one data set. These data are acquired in 8799 data which are utilized for AI model training, see Sec. 6.2. Here we replaced the actual linewidth (FWHM) with the difference of the linewidth to a mean value (Δf). The results indicate that both channels have less than ($\pm$1 Hz) linewidth fluctuation. It is noteworthy that both spectra exhibit fluctuations with a certain degree of similarity, following a similar trend. This could come from the frequency drift of the magnet system.

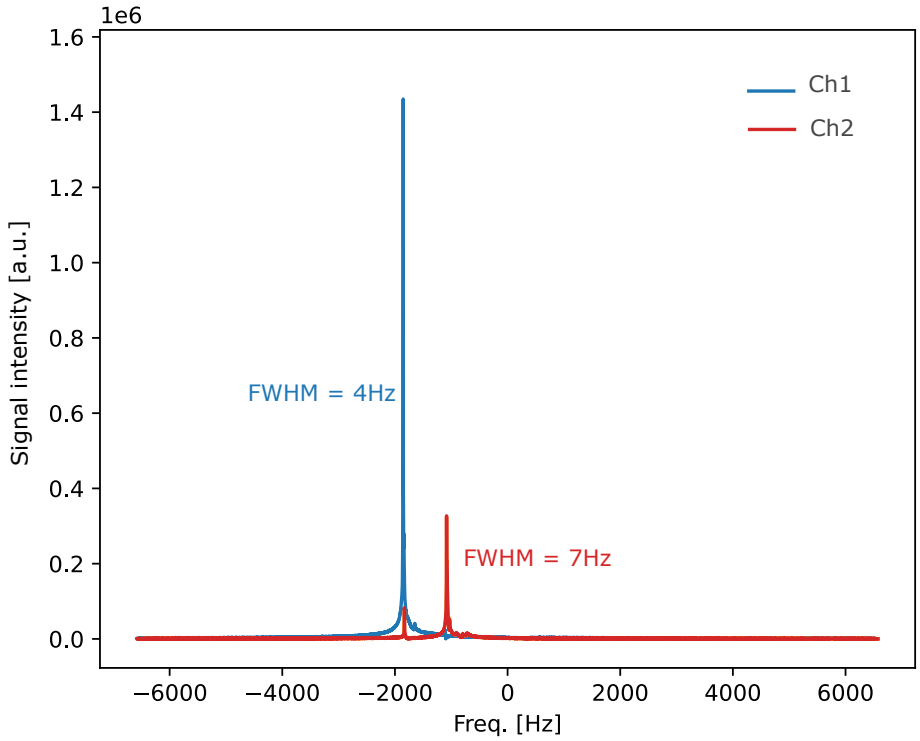

Figure 6.22: Parallel water spectrum after adequate high-order manual shimming. The optimal linewidth for each channel is 4 Hz and 7 Hz respectively.

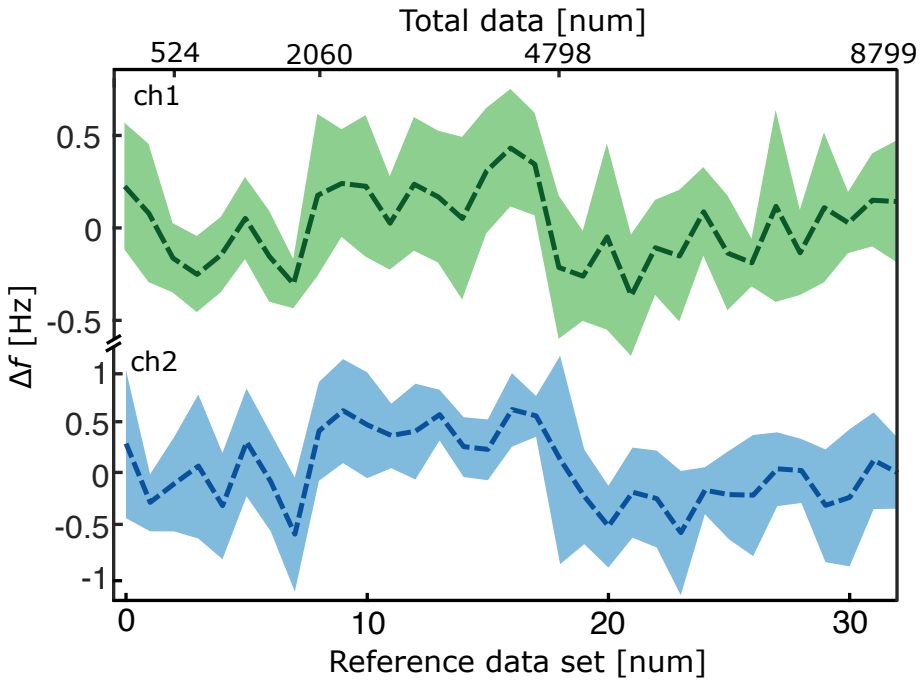

Figure 6.23: Shimming stability of two channels over two days, reported via 160 reference-shimmed spectra that were sampled after intervals of 50 spectra in the datasets. (green: Channel 1, blue: Channel 2)

high field parallel heternuclei and homoneuculi spectrum

The parallel 1D ^{1}H NMR homonuclear (experiments e1 and e2) spectra of two samples are presented in Fig. 6.24 measured in parallel by two stripline coils: (e1), where channel 1 is filled with a 0.4 M Niacinamide solution and channel 2 is filled with 17.4 M Acetic acid, and (e2), where channel 1 is a 0.16 M D-(+)-maltose solution and channel 2 is a 0.3 M Tris(hydroxymethyl)aminomethane acetate (Trizma) solution. As demonstrated in the figure, each proton is labelled with respect to its chemical shift. The spectra are averaged from 256 scans. Because of the signal cross-talk resulting primarily from the RF coils and coaxial cables in both channels, we performed signal subtraction during post-processing on the two raw spectra. Details of the spectrum decoupling and signal subtraction will be provided in the Sec. 6.3. All the necessary main peaks are resolved in the measurement results.

While homonuclear parallel NMR offers the advantage of directly comparing signals from same nucleui, it introduces the issue of signal coupling between the two channels. This occurs because both coils simultaneously excite and receive signals at the same frequency. Here, we tested the probe in heteronuclear mode, performing parallel spectroscopy simultaneously at different striplines, one tuned to ^{1}H, and the other to ^{19}F. We transferred two samples of water and FC-770 ($C_{10}F_{22}$) and measured them accordingly (see Fig. 6.24 experiment e3).

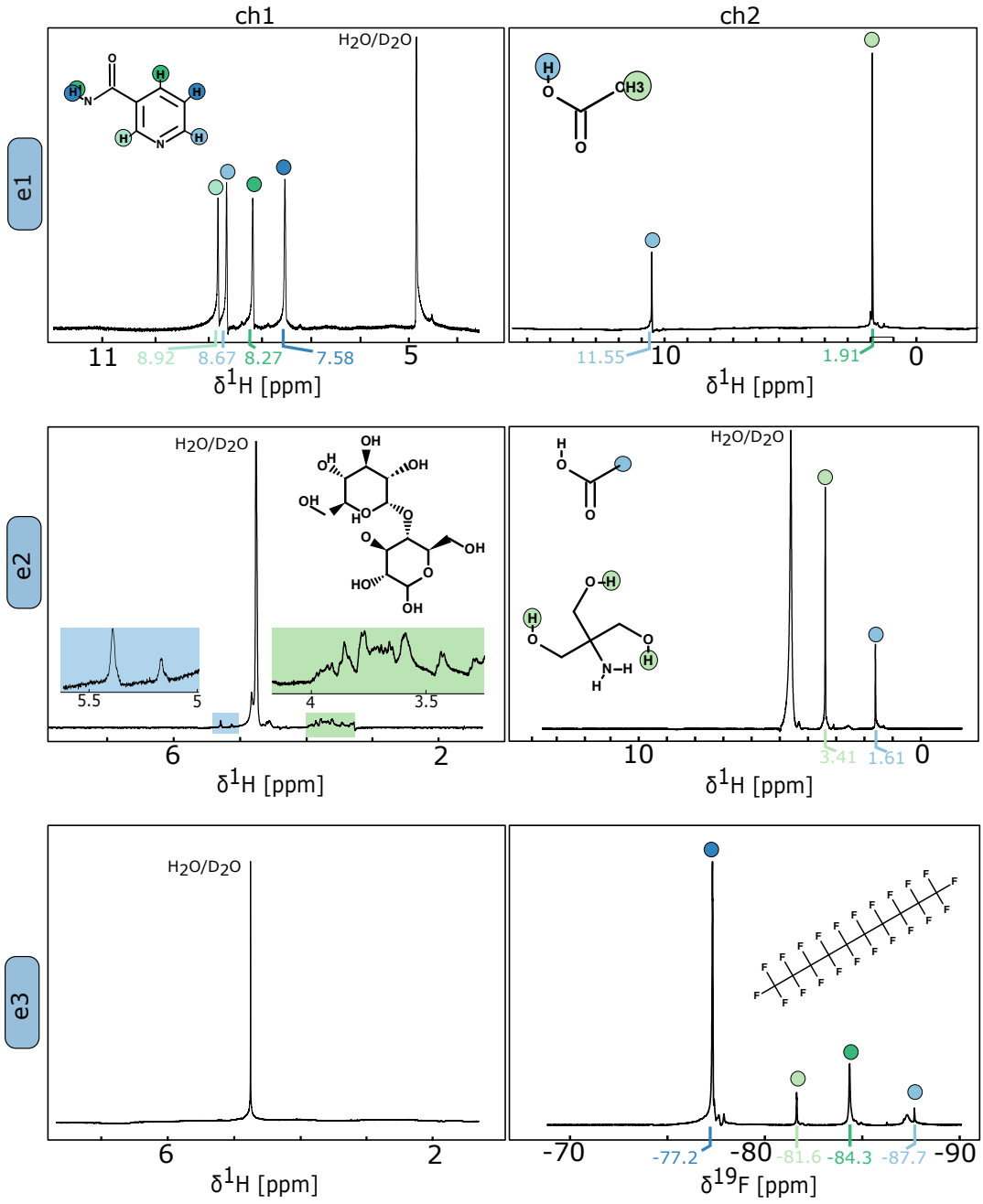

Figure 6.24: NMR spectra recorded with synchronized excitation and reception acquired in the two-channel probehead. (e1) ^{1}H NMR spectra of niacinamide and acetic acid. (e2) ^{1}H NMR spectra of D-maltose and trizma acetate. (e3) ^{1}H NMR spectrum of 50% (v/v) H_2O/D_2O and ^{19}F NMR spectrum of FC770

6.2 Parallel AI shimming

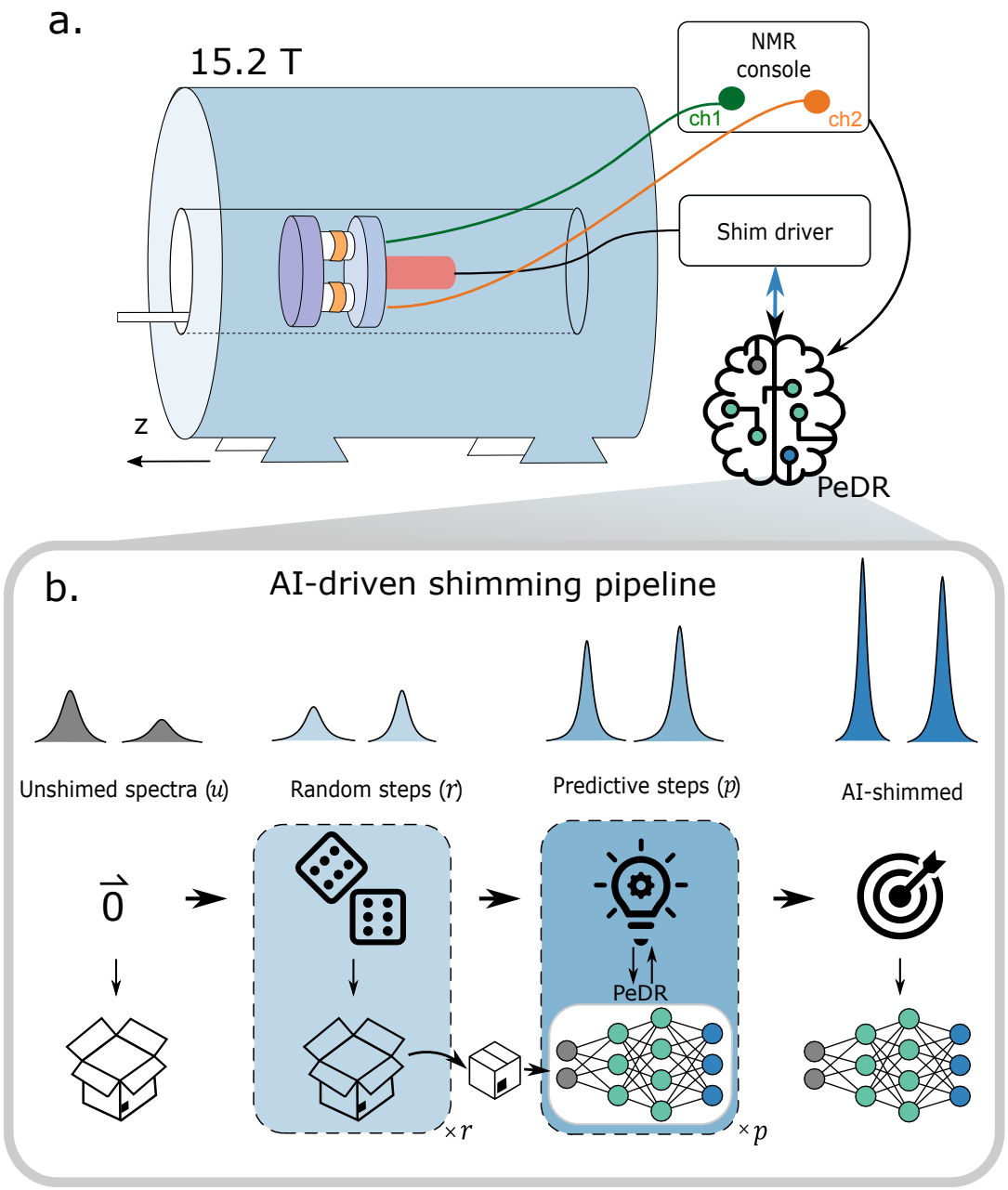

Figure 6.25: Concept of parallel NMR and AI-driven shimming. (a) Experimental setup and routing for parallel shimming utilizing a neural network model. (b) Parallel enhanced deep regression (PeDR) pipeline with random and predictive shim offset steps.

Shimming becomes a challenging task in parallel spectroscopy, where multiple channels are used to acquire signals from different regions of interest. Unlike single-channel spectroscopy, where a single set of orthogonal shim coils can be used to correct the field inhomogeneity, parallel shimming requires a more sophisticated approach that considers shim interactions and RF couplings between the channels. Moreover, our custom hardware

shows non-idealities due to manual assembly, resulting in non-orthogonal shim fields that complicate the optimization problem. Even though the shim coils may be orthogonal for each channel taken separately, they are not necessarily simultaneously so for two or more coils, leaving classical algorithms such as the simplex prone to performing many redundant actions. We study shimming supported by AI, i.e., AI-driven shimming. We argue that AI can handle the high-dimensional and non-linear nature of the shimming problem, and can learn from the complex cross-sensitivity among the channels. We also show that AI can adapt to the non-orthogonal shim fields and find good shim settings for each channel.

Fig. 6.25a shows the experimental setup and the routing for AI-driven parallel shimming on two localized shimming sets. Each RF channel is separately connected to the NMR console, where the parallel NMR spectrum is acquired and stored. The local shim sets are connected to the shim drivers. The shimming setting and the NMR spectrum are stored and trained in the Parallel enable Deep Regression (PeDR) model for the shimming experiment. Fig. 6.25b presents the parallel shimming pipeline, for which we initially acquired an unshimed spectra (u), and a fixed number of dataset (r) that are randomly determined, which is located in the model-internal shimming history. All the above datasets help the PeDR model to orientate itself in the shimming space. Then some predictive steps (p) are applied to guide the unshimed spectra to the right location (which is properly shimmed). Two properly shimmed NMR spectra will be done in the total amount ($r + p$) of steps. More detailed information on the AI model and related DL training procedures can be found in our previously published article [J3].

Fig. 6.26a,b reports the exemplary result based on the AI-driven shimming on two channels probehead. The figure demonstrates the transformation of the spectrum from unshimmed (gray), a couple of random spectra acquired in the random steps (light blue), and an AI-shimmed spectrum. We examine this method on different samples, acetic acid, which intrinsically has different susceptibilities from the training data. The result explains the generalization of this method, which can potentially be utilized in different chemicals.

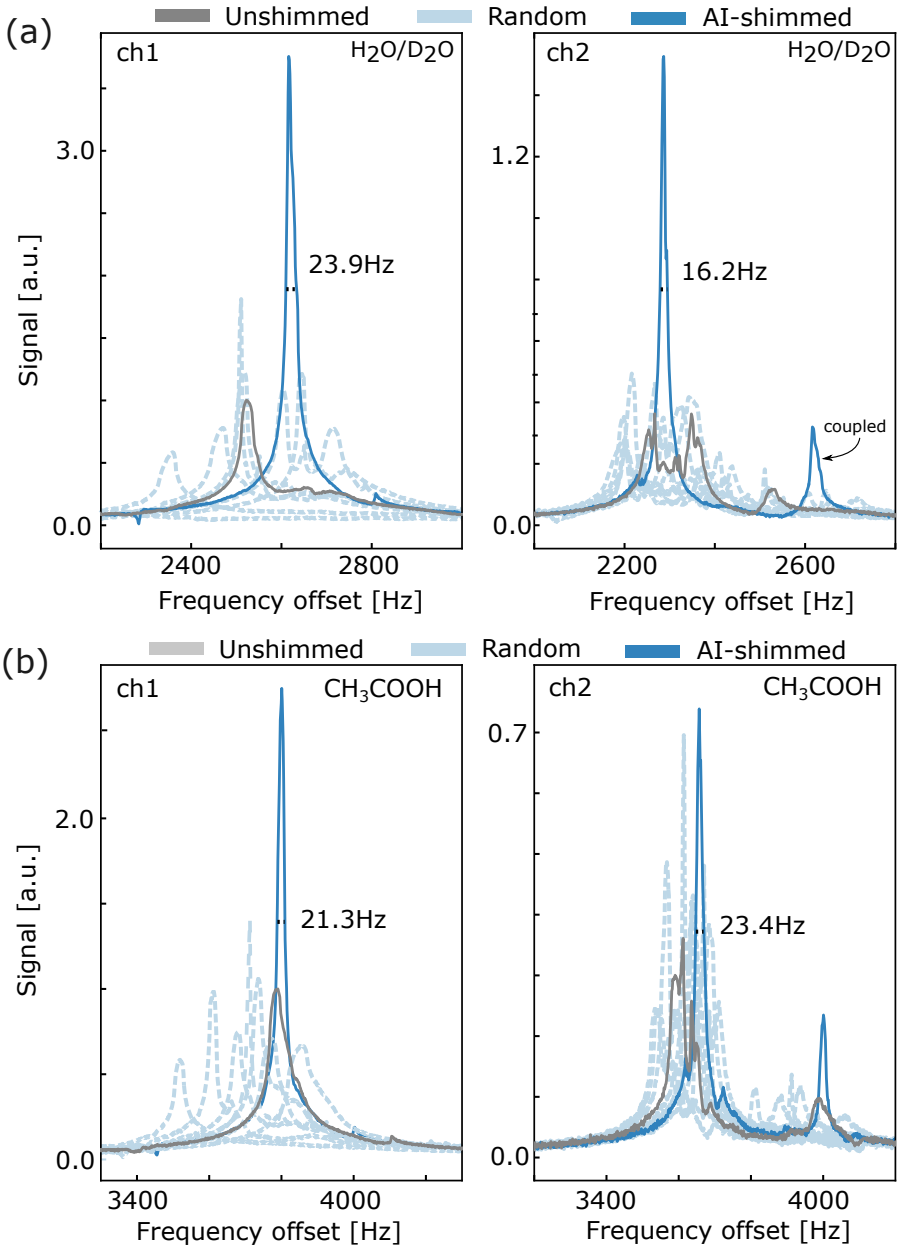

Figure 6.26: AI driven shimming result on a parallel probe. Both the two samples are (a) DI water or (b) Acetic acid solution.

6.3 Parallel spectrum decomposition and post-processing

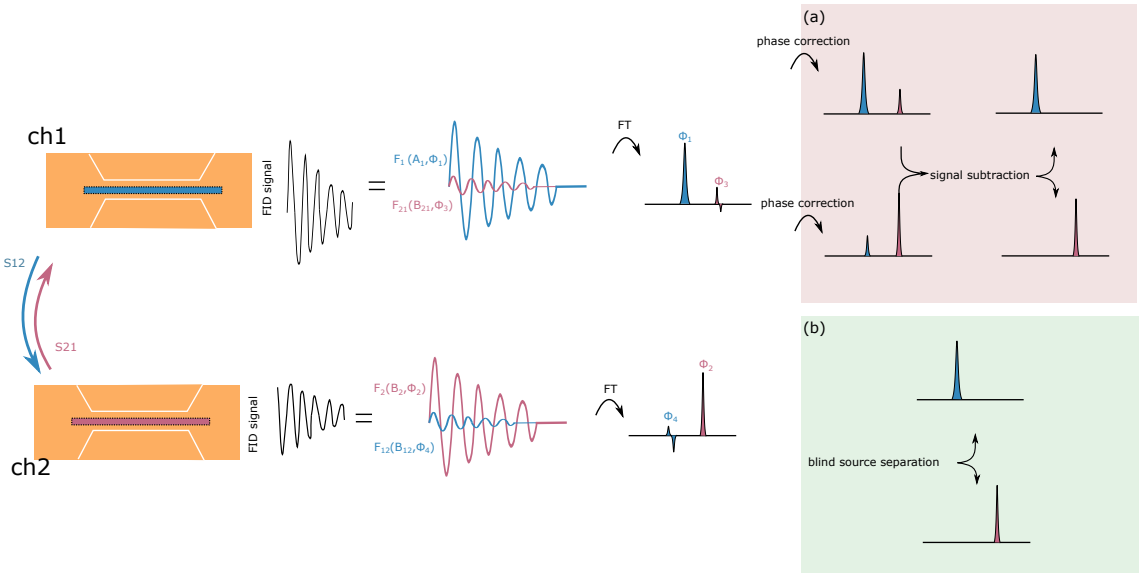

Figure 6.27: Workflow of isolating two parallel NMR spectra through (a) empirical method, including FID phase alignment, spectrum alignment, and direct subtraction. (b) blind source separation

Based on the results of electrical characterization, it was observed that geometric decoupling, relying on the field map of the coils, is effective in reducing the coupling coefficient to the range of -20dB to -50dB. However, during NMR experiments, the cables used for connection to NMR consoles and the built-in circuit are not sufficiently shielded, resulting in signal cross-talk between channels being unaddressed. Also, in the case of a high degree or number of array, this method has its limitations. As a result, we explore post-processing methods to achieve a clean and well-defined spectrum from the measurement results.

Subtracting spectra is a well-established method in Raman spectroscopy for eliminating background signals [112]. This approach may appear to be a convenient and efficient solution for parallel NMR. However, when it comes to eliminating the coupling peak, there are certain distinctions from the background signal subtraction methods. Firstly, the NMR peaks typically exhibit narrow linewidths, falling within the sub-Hz to tens of Hz range. Secondly, the phase of the detected magnetization from different samples in different channels introduces variability in the final-phase correction coefficient for each channel. Thirdly, the removal peaks are coupled from one channel to another at a specific coupling ratio, resulting in differing signal intensities at the same frequency.

In this scenario, we examine a straightforward case involving two channels, each containing distinct samples (Fig. 6.27). The RF coupling, characterized by a coefficient denoted as S21,

induces peak coupling. Following the excitation of an RF pulse, each channel exhibits its own Free Induction Decay (FID), and the magnetization differs between the two channels. We assume that both channels transmit and receive RF pulses simultaneously, and each sample has only one prominent peak.

For channel one, the FID can be decomposed as $FID_1 = F_1(A_1,\Phi_1) + F_{21}(B_{21},\Phi_3)$. Here, F_1 represents the original FID acquired solely from the protons of channel 1, characterized by the intensity A_1 and phase Φ_1. F_{21} denotes the coupled peaks, featuring the intensity B_{21} and phase Φ_3. Similarly, for channel 2, the FID_2 obtained is the sum of $F_2(B_2,\Phi_2)$ and $F_{12}(B_{12},\Phi_4)$. After Fourier transformation, the spectrum acquired in CH1 or CH2 comprises a major peak and a coupling peak.

Here, we present two post-processing methods to disentangle and separate two spectra, as illustrated in Fig. 6.27a,b. The first proposed approach is grounded in an empirical rule. Given that the coupled peak, stemming from RF coupling, shares the same frequency as the original main peak, we initially align the two spectra on the same frequency range, making the coupling peak easily distinguishable. Before performing signal subtraction in the frequency-domain spectra, we identify the phase difference between the coupled peak and the major peak. Following the determination of the phase for each peak in the spectrum, we adjust the phase of the major peak in Ch2 and the coupled peak in Ch1 to the same phase. Consequently, the spectrum after phase correction is obtained.

$$\begin{aligned} S1_{corrected} &= FFT(F_1(A_1,\Phi_1+\Phi_{n1})+F_{21}(B_{21},\Phi_3+\Phi_{n1})) \\ S2_{corrected} &= FFT(F_2(B_2,\Phi_2+\Phi_{n2})+F_{12}(B_{12},\Phi_4+\Phi_{n2})) \end{aligned} \tag{6.1}$$

where Φ_{n1} and Φ_{n2} are denoted as the required additional phase to align the two phase signals of the same molecules in two spectra to the same phase. Afterward, we can subtract the two spectra ($S1_{corrected}$ & $S2_{corrected}$) by the RF coupling coefficient (S_{21}). The post-processed spectrum in channel one after subtraction can be written as $S1_{corrected} - S_{21}$ x $S2_{corrected}$, and vice versa. Fig. 6.28 presents the initial outcomes of experimental data acquired from our two-channel array before signal subtraction. Ch1 is loaded with D-maltose, and Ch2 contains Trizma acetate. Upon aligning the two spectra within the same frequency range, the coupled peak (F21 or F12) exhibits a notably distinct phase compared to the major peak. Fig. 6.29 illustrates the post-processed results for the example depicted in Fig. 6.28. In comparison to the original spectrum, the direct subtraction effectively eliminated over 80% of the coupled components while preserving the individual signals. However, this technique has certain limitations: (i) The subtraction method inevitably leads to a reduction in SNR. (ii) Overlapping peaks at the same frequency makes it challenging

to distinguish between original and coupled peaks. (iii) The coupling coefficient is directly calculated from the spectrum.

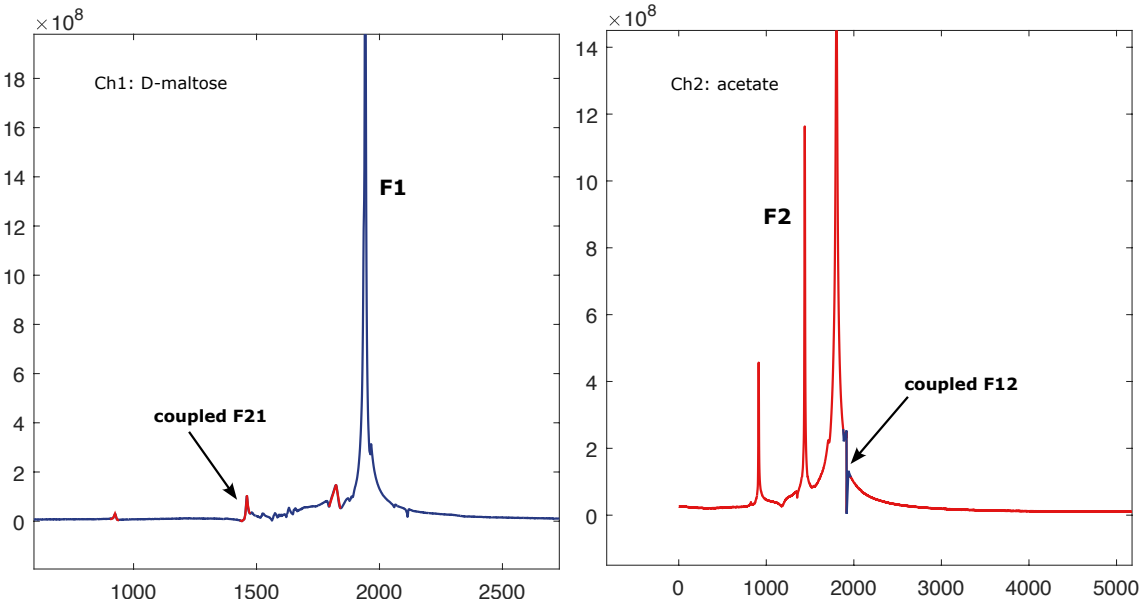

Figure 6.28: Parallel NMR spectrum before signal subtraction. Channel 1 contains D-maltose, and channel 2 contains acetate.

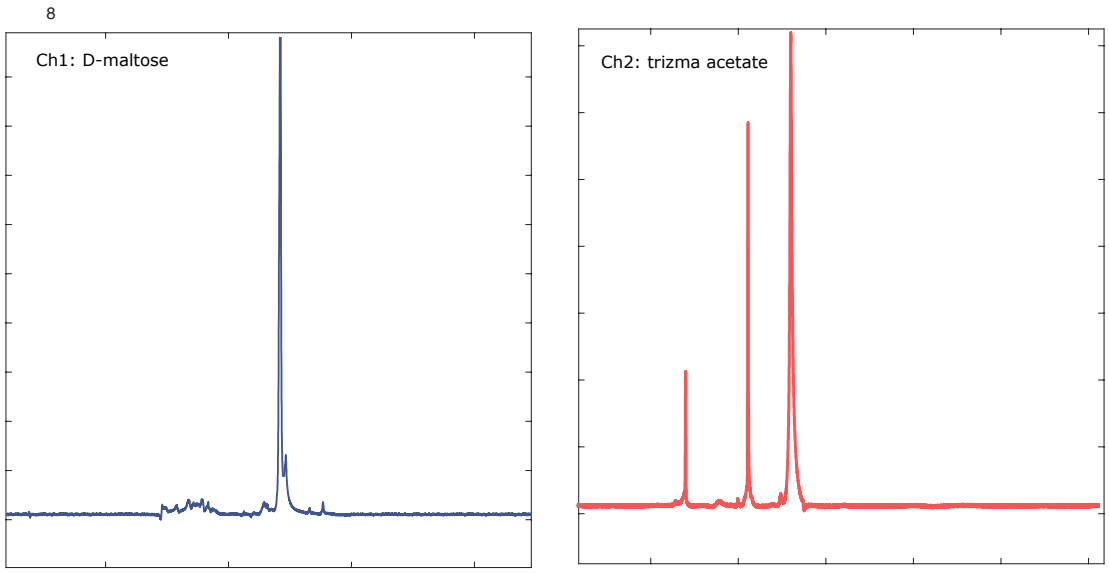

Figure 6.29: Parallel NMR spectrum after signal subtraction in the case of Fig. 6.28.

We also investigate blind source separation, specifically utilizing the second-order blind identification (SOBI) algorithm [113]. This approach revolves around the joint diagonalization of a set of covariance matrices, making it adaptable to challenging scenarios such as low SNR and sources with minimal spectral differences. Additional details about the method can be found in our previously published article [J4]. In summary, this method successfully eliminates over 90% of the coupled components in both channels, as illustrated

in Fig. 6.30. The red lines represent the original spectrum, while the blue lines depict the separated operation. This process preserves the SNR and lineshape of the spectrum. The separation method proves to be highly effective in isolating two spectra.

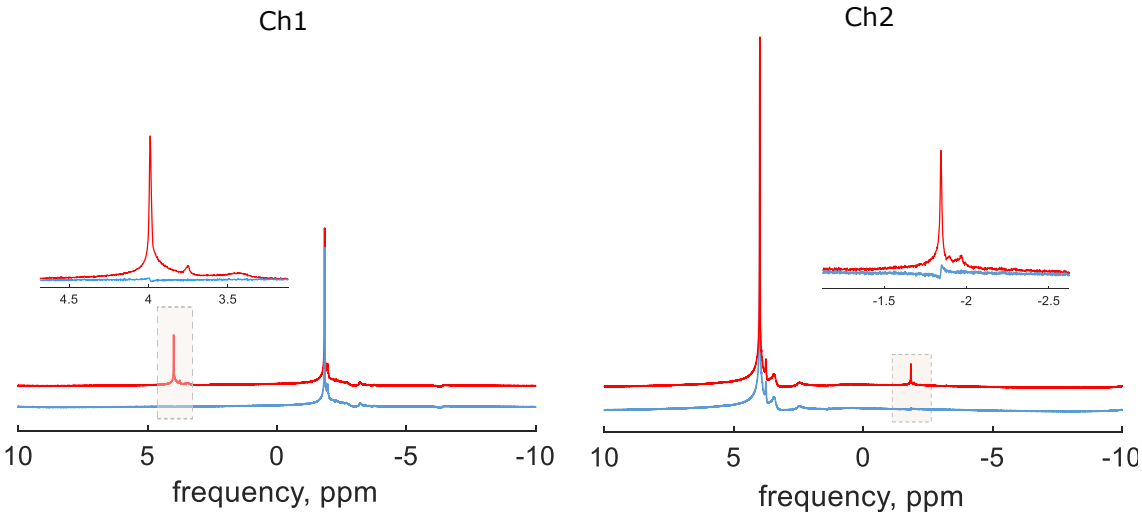

Figure 6.30: Post-processing parallel NMR spectra using blind source separation method. (adopted from He et al. [J4])

7 Conclusions

In this thesis, four significant contributions are made toward advancing parallel NMR spectroscopy. The first contribution introduces a prototype of a multiple-coil system based on an integrated NC designed for parallel NMR spectroscopy, offering potential extensions to current high-throughput techniques. Challenges such as achieving shimming on multiple samples and ensuring geometrical inter-coil inductive decoupling are carefully addressed. The system operates at a 1.05T field magnet, demonstrating the simultaneous acquisition of two samples without penalties in B_0 distortion and SNR degradation. Geometrical decoupling efficiently isolates two NCs, revealing no signal bleeding in experimental results.

The second contribution involves the development of a new type of stripline coil known as the butterfly coil, showcasing potential applications in parallel spectroscopy. The design focuses on enhanced current density, resulting in a stronger B1 field and improved SNR. Despite a slight penalty in B1 homogeneity (20%), the butterfly coil design demonstrates approximately twice the SNR enhancement for a mass-limited sample and exhibits better shielding performance compared to regular stripline coils.

The third contribution implements the SABRE hyperpolarization technique in a low-field parallel probehead, enabling continuous SABRE experiments. Signal enhancement is examined with varying flow rates, revealing saturation of signal enhancement due to relaxation time. The probehead demonstrates the capability to run SABRE experiments in two channels, with both channels exhibiting the SABRE effect.

In the final contribution, aiming to address the identified insufficient linewidth (0.5ppm) highlighted in Chapter 3, the NMR cell (NC) concept undergoes adaptation for a high-field environment at 15.6T. This adaptation involves the introduction of miniaturized RF and shim coils, featuring a compact stripline coil inspired by origami. The designed stripline coil achieves an exceptionally high self-resonance frequency (SF), an acceptable Q factor of 42, and effective signal isolation. Two versions of the probehead are proposed, with a detailed comparison provided.

Despite utilizing only six local shims per channel, the study successfully mitigates major distortions, achieving a 4Hz linewidth (corresponding to 6 ppb). The wrapped local shim set demonstrates remarkable stability over a two-day experiment, exhibiting negligible linewidth fluctuation. Homonuclear (^{1}H, ^{1}H) and heteronuclear (^{1}H, ^{19}F) parallel NMR experiments are conducted successfully. In the latter part of the chapter, using a water-only dataset in our study allows for a focused evaluation of an AI-driven shimming approach, providing a faster shimming process than traditional automatic shimming. This approach paves the way to address the complexity of the shimming process in parallel spectroscopy. In the last part of the contribution, two spectra isolation methods are investigated to efficiently eliminate 80 to 90% of coupled components in parallel spectra.

An outlook of this NC based probehead is in the field of metabolomics, which studies enormous numbers of samples in biological systems. And our prototype has demonstrated the feasibility of utilizing four NC coils, with a tuning range covering both ^{1}H and ^{19}F nuclei. Particularly, ^{19}F NMR has offered valuable insights into exploring protein structure and dynamics [114] for drug design purposes. The four-coil parallel probehead could be further expanded to an array of eight coils. Moreover, the size of the NC could be scaled down further by leveraging clean-room microfabrication techniques.

Pulsed field gradients are used for a variety of tasks, from temporary suppression of solvent signals, to accessing diffusion parameters, and so would be desirable within an arrayed detector system. The concentric design of the NC offers the potential for integrating gradient coils, provided proper shielding is implemented. Additionally, employing parallelized experiments in conjunction with ultra-fast supersequences [115] shows promise in monitoring time-dependent processes like chemical reactions.

The integration of impedance sensing techniques [27] allows for the sequential measurement of multiple samples in a short time frame, enabling the analysis of 9 samples done in just 3.6 minutes. Our setup incorporates a sample flow channel, facilitating easy sample transportation. By concurrently and sequentially running several samples, the time required for metabolic experiments could be significantly reduced.

Publications

Journal Articles

[J1] **Yen-Tse Cheng**, Mazin Jouda, and Jan G Korvink. Sample-centred shimming enables independent parallel NMR detection. *Scientific Reports*, 12(1):1–9, 2022.

[J2] **Yen-Tse Cheng**, Jan G Korvink, and Mazin Jouda. A field focusing butterfly stripline detects nmr at higher signal-to-noise ratio. *Journal of Magnetic Resonance*, 353:107517, 2023.

[J3] Moritz Becker, **Yen-Tse Cheng**, Achim Voigt, Ajmal Chenakkara, Mengjia He, Sören Lehmkuhl, Mazin Jouda, and Jan G Korvink. Artificial intelligence-driven shimming for parallel high field nuclear magnetic resonance. *Scientific Reports*, 13(1):17983, 2023. (**Shared first authorship**)

[J4] Mengjia He, Dilara Faderl, Neil MacKinnon, **Yen-Tse Cheng**, Dominique Buyens, Mazin Jouda, Burkhard Luy, and Jan G Korvink. A digital twin for parallel liquid-state nuclear magnetic resonance spectroscopy. *Communications Engineering*, 3(1):90, 2024.

[J5] Jing Yang, **Yen-Tse Cheng**, Jan G Korvink, and Mazin Jouda. (2024) Continuous flow high throughput parallel SABRE. (**Shared first authorship**, **In preparation**)

Conference contributions

[C1] **Yen-Tse Cheng**, Mazin Jouda, Jan G Korvink. Localized shim system for improving NMR spectral resolution. Experimental Nuclear Magnetic Resonance Conference (ENC), Orlando, USA, 2022. Poster Presentation.

[C2] **Yen-Tse Cheng**, Mazin Jouda, Jan G Korvink. Integrated shimming for NMR parallelism. 43rd FGMR Annual Discussion Meeting, Karlsruhe, Germany, 2022. Poster Presentation

Bibliography

[1] Brian B Haab, Maitreya J Dunham, and Patrick O Brown. Protein microarrays for highly parallel detection and quantitation of specific proteins and antibodies in complex solutions. *Genome biology*, 2:1–13, 2001.

[2] Amiram Grinvald, RD Frostig, EDMUND Lieke, and RINA Hildesheim. Optical imaging of neuronal activity. *Physiological reviews*, 68(4):1285–1366, 1988.

[3] M Bigas, Enric Cabruja, Josep Forest, and Joaquim Salvi. Review of cmos image sensors. *Microelectronics journal*, 37(5):433–451, 2006.

[4] Pedro Silva Girão, Pedro Miguel Pinto Ramos, Octavian Postolache, and José Miguel Dias Pereira. Tactile sensors for robotic applications. *Measurement*, 46(3):1257–1271, 2013.

[5] Robin M Heidemann, Özkan Özsarlak, Paul M Parizel, Johan Michiels, Berthold Kiefer, Vladimir Jellus, Mathias Müller, Felix Breuer, Martin Blaimer, Mark A Griswold, et al. A brief review of parallel magnetic resonance imaging. *European radiology*, 13:2323–2337, 2003.

[6] Isidor Isaac Rabi, Jerrold R Zacharias, Sidney Millman, and Polykarp Kusch. A new method of measuring nuclear magnetic moment. *Physical review*, 53(4):318, 1938.

[7] Felix Bloch. Nuclear induction. *Physical review*, 70(7-8):460, 1946.

[8] Edward M Purcell, Henry Cutler Torrey, and Robert V Pound. Resonance absorption by nuclear magnetic moments in a solid. *Physical review*, 69(1-2):37, 1946.

[9] Paul C Lauterbur. Image formation by induced local interactions: examples employing nuclear magnetic resonance. *nature*, 242(5394):190–191, 1973.

[10] Allen N Garroway, Peter K Grannell, and Peter Mansfield. Image formation in nmr by a selective irradiative process. *Journal of Physics C: Solid State Physics*,

7(24):L457, 1974.

[11] Peter B Roemer, William A Edelstein, Cecil E Hayes, Steven P Souza, and Otward M Mueller. The NMR phased array. *Magnetic resonance in medicine*, 16(2):192–225, 1990.

[12] David I Hoult and RE Richards. The signal-to-noise ratio of the nuclear magnetic resonance experiment. *Journal of Magnetic Resonance (1969)*, 24(1):71–85, 1976.

[13] Sergio Pissanetzky. Structured coils for nmr applications. *IEEE transactions on magnetics*, 28(4):1961–1968, 1992.

[14] Jeffrey L Evelhoch, Michael G Crowley, and Joseph JH Ackerman. Signal-to-noise optimization and observed volume localization with circular surface coils. *Journal of Magnetic Resonance (1969)*, 56(1):110–124, 1984.

[15] Kevin R Minard and Robert A Wind. Solenoidal microcoil design—part ii: Optimizing winding parameters for maximum signal-to-noise performance. *Concepts in Magnetic Resonance*, 13(3):190–210, 2001.

[16] H Wang, L Ciobanu, AS Edison, and AG Webb. An eight-coil high-frequency probehead design for high-throughput nuclear magnetic resonance spectroscopy. *Journal of Magnetic Resonance*, 170(2):206–212, 2004.

[17] Ka-Meng Lei, Dongwan Ha, Yi-Qiao Song, Robert M Westervelt, Rui Martins, Pui-In Mak, and Donhee Ham. Portable NMR with parallelism. *Analytical Chemistry*, 92(2):2112–2120, 2020.

[18] Timothy L Peck, Richard L Magin, and Paul C Lauterbur. Design and analysis of microcoils for nmr microscopy. *Journal of Magnetic Resonance, Series B*, 108(2):114–124, 1995.

[19] Dean L Olson, Timothy L Peck, Andrew G Webb, Richard L Magin, and Jonathan V Sweedler. High-resolution microcoil 1h-nmr for mass-limited, nanoliter-volume samples. *Science*, 270(5244):1967–1970, 1995.

[20] Klaus Ehrmann, Nicolas Saillen, Franck Vincent, Matthieu Stettler, Martin Jordan, Florian Maria Wurm, Pierre-André Besse, and Radivoje Popovic. Microfabricated solenoids and helmholtz coils for nmr spectroscopy of mammalian cells. *Lab on a Chip*, 7(3):373–380, 2007.

[21] K Kratt, V Badilita, T Burger, JG Korvink, and U Wallrabe. A fully mems-compatible process for 3d high aspect ratio micro coils obtained with an automatic wire bonder. *Journal of Micromechanics and Microengineering*, 20(1):015021, 2009.

[22] DM Ginsberg and Melvin J Melchner. Optimum geometry of saddle shaped coils for generating a uniform magnetic field. *Review of Scientific Instruments*, 41(1):122–123, 1970.

[23] Andreas Ostendorf and Boris N Chichkov. Two-photon polymerization: a new approach to micromachining. *Photonics spectra*, 40(10):72, 2006.

[24] Mingwei Li, Rustom B Bhiladvala, Thomas J Morrow, James A Sioss, Kok-Keong Lew, Joan M Redwing, Christine D Keating, and Theresa S Mayer. Bottom-up assembly of large-area nanowire resonator arrays. *Nature Nanotechnology*, 3(2):88–92, 2008.

[25] Haoran Fu, Kewang Nan, Paul Froeter, Wen Huang, Yuan Liu, Yiqi Wang, Juntong Wang, Zheng Yan, Haiwen Luan, Xiaogang Guo, et al. Mechanically-guided deterministic assembly of 3d mesostructures assisted by residual stresses. *small*, 13(24):1700151, 2017.

[26] Nan Wang, Aleksandr Egunov, Nils Spengler, Nikolaus Nestle, Valeriy Luchnikov, Dario Mager, and Jan G Korvink. Inkjet printed micro saddle coil for mr imaging. In *NIP & Digital Fabrication Conference*, volume 32, pages 339–342. Society for Imaging Science and Technology, 2016.

[27] Omar Nassar, Mazin Jouda, Michael Rapp, Dario Mager, Jan G Korvink, and Neil MacKinnon. Integrated impedance sensing of liquid sample plug flow enables automated high throughput NMR spectroscopy. *Microsystems & Nanoengineering*, 7(1):1–17, 2021.

[28] Vijay Sharma et al. Microstrip antenna-inception, progress and current-state of the art review. *Recent Advances in Electrical & Electronic Engineering (Formerly Recent Patents on Electrical & Electronic Engineering)*, 13(6):769–794, 2020.

[29] PJM Van Bentum, JWG Janssen, APM Kentgens, J Bart, and Johannes GE Gardeniers. Stripline probes for nuclear magnetic resonance. *Journal of Magnetic Resonance*, 189(1):104–113, 2007.

[30] Ying Chen, Hardeep S Mehta, Mark C Butler, Eric D Walter, Patrick N Reardon, Ryan S Renslow, Karl T Mueller, and Nancy M Washton. High-resolution microstrip nmr detectors for subnanoliter samples. *Physical Chemistry Chemical Physics*, 19(41):28163–28174, 2017.

[31] Graeme Finch, Ali Yilmaz, and Marcel Utz. An optimised detector for in-situ high-resolution NMR in microfluidic devices. *Journal of Magnetic Resonance*, 262:73–80, 2016.

[32] C Massin, F Vincent, A Homsy, K Ehrmann, G Boero, P-A Besse, A Daridon, E Verpoorte, NF De Rooij, and RS Popovic. Planar microcoil-based microfluidic nmr probes. *Journal of Magnetic Resonance*, 164(2):242–255, 2003.

[33] L Renaud, M Armenean, L Berry, P Kleimann, P Morin, M Pitaval, J O'Brien, M Brunet, and H Saint-Jalmes. Implantable planar rf microcoils for nmr microspectroscopy. *Sensors and Actuators A: Physical*, 99(3):244–248, 2002.

[34] Tim L Peck, Richard L Magin, J Kruse, and M Feng. Nmr microspectroscopy using 100/spl mu/m planar rf coils fabricated on gallium arsenide substrates. *IEEE transactions on biomedical engineering*, 41(7):706–709, 1994.

[35] James S. Hyde, Andrzej Jesmanowicz, Wojciech Froncisz, J. Bruce Kneeland, Thomas M. Grist, and Nicholas F. Campagna. Parallel image acquisition from noninteracting local coils. *Journal of Magnetic Resonance*, 70:512–517, 1986.

[36] Yudong Zhu, Christopher J Hardy, Daniel K Sodickson, Randy O Giaquinto, Charles L Dumoulin, Gontran Kenwood, Thoralf Niendorf, Hubert Lejay, Charles A McKenzie, Michael A Ohliger, et al. Highly parallel volumetric imaging with a 32-element rf coil array. *Magnetic Resonance in Medicine: An Official Journal of the International Society for Magnetic Resonance in Medicine*, 52(4):869–877, 2004.

[37] Graham C Wiggins, Jonathan R Polimeni, Andreas Potthast, Melanie Schmitt, Vijay Alagappan, and Lawrence L Wald. 96-channel receive-only head coil for 3 tesla: design optimization and evaluation. *Magnetic Resonance in Medicine: An Official Journal of the International Society for Magnetic Resonance in Medicine*, 62(3):754–762, 2009.

[38] Christopher J Hardy, Randy O Giaquinto, Joseph E Piel, Kenneth W Rohling AAS, Luca Marinelli, Daniel J Blezek, Eric W Fiveland, Robert D Darrow, and Thomas KF

Foo. 128-channel body MRI with a flexible high-density receiver-coil array. *Journal of Magnetic Resonance Imaging: An Official Journal of the International Society for Magnetic Resonance in Medicine*, 28(5):1219–1225, 2008.

[39] Oliver G Gruschke, Nicoleta Baxan, Lars Clad, Kai Kratt, Dominik von Elverfeldt, Andreas Peter, Jürgen Hennig, Vlad Badilita, Ulrike Wallrabe, and Jan G Korvink. Lab on a chip phased-array mr multi-platform analysis system. *Lab on a Chip*, 12(3):495–502, 2012.

[40] Jens Anders, Giuseppe Chiaramonte, Paul SanGiorgio, and Giovanni Boero. A single-chip array of nmr receivers. *Journal of Magnetic Resonance*, 201(2):239–249, 2009.

[41] Klaas P Pruessmann, Markus Weiger, Markus B Scheidegger, and Peter Boesiger. Sense: sensitivity encoding for fast mri. *Magnetic Resonance in Medicine: An Official Journal of the International Society for Magnetic Resonance in Medicine*, 42(5):952–962, 1999.

[42] Mark A Griswold, Peter M Jakob, Robin M Heidemann, Mathias Nittka, Vladimir Jellus, Jianmin Wang, Berthold Kiefer, and Axel Haase. Generalized autocalibrating partially parallel acquisitions (grappa). *Magnetic Resonance in Medicine: An Official Journal of the International Society for Magnetic Resonance in Medicine*, 47(6):1202–1210, 2002.

[43] Jerzy Bodurka, Patrick J Ledden, Peter van Gelderen, Renxin Chu, Jacco A de Zwart, Doug Morris, and Jeff H Duyn. Scalable multichannel mri data acquisition system. *Magnetic Resonance in Medicine: An Official Journal of the International Society for Magnetic Resonance in Medicine*, 51(1):165–171, 2004.

[44] Salvatore Celozzi, Rodolfo Araneo, Paolo Burghignoli, and Giampiero Lovat. *Electromagnetic Shielding: Theory and Applications*. John Wiley & Sons, 2023.

[45] LF Fuks, FSC Huang, CM Carter, WA Edelstein, and PB Roemer. Susceptibility, lineshape, and shimming in high-resolution NMR. *Journal of Magnetic Resonance (1969)*, 100(2):229–242, 1992.

[46] Christoph Juchem and Robin A de Graaf. B0 magnetic field homogeneity and shimming for in vivo magnetic resonance spectroscopy. *Analytical biochemistry*, 529:17–29, 2017.

[47] Wei-Chih Wang. Electromagnetic wave theory. *Google Scholar*, 1986.

[48] Gwendolyn N Chmurny and David I Hoult. The ancient and honourable art of shimming. *Concepts in Magnetic Resonance*, 2(3):131–149, 1990.

[49] Tian Xia, Zhiying Miao, Shanshan Chen, Hongzhi Wang, and Yefeng Yao. Theory and development of biplanar active shim coils for a permanent nmr analyzer. *Plos one*, 12(7):e0181552, 2017.

[50] Jason P Stockmann and Lawrence L Wald. In vivo b0 field shimming methods for mri at 7 t. *Neuroimage*, 168:71–87, 2018.

[51] Françoise Roméo and DI Hoult. Magnet field profiling: analysis and correcting coil design. *Magnetic resonance in medicine*, 1(1):44–65, 1984.

[52] James L Wilson, Mark Jenkinson, and Peter Jezzard. Optimization of static field homogeneity in human brain using diamagnetic passive shims. *Magnetic Resonance in Medicine: An Official Journal of the International Society for Magnetic Resonance in Medicine*, 48(5):906–914, 2002.

[53] Rhodri Cusack, Benedict Russell, Sylvia ML Cox, Claudia De Panfilis, Christian Schwarzbauer, and Richard Ansorge. An evaluation of the use of passive shimming to improve frontal sensitivity in fMRI. *Neuroimage*, 24(1):82–91, 2005.

[54] Kevin M Koch, Peter B Brown, Douglas L Rothman, and Robin A de Graaf. Sample-specific diamagnetic and paramagnetic passive shimming. *Journal of magnetic resonance*, 182(1):66–74, 2006.

[55] Arnon Neufeld, Yaniv Assaf, Moshe Graif, Talma Hendler, and Gil Navon. Susceptibility-matched envelope for the correction of epi artifacts. *Magnetic resonance imaging*, 23(9):947–951, 2005.

[56] Sejung Yang, Hahnsung Kim, Min-Oh Ghim, Byung-Uk Lee, and Dong-Hyun Kim. Local in vivo shimming using adaptive passive shim positioning. *Magnetic resonance imaging*, 29(3):401–407, 2011.

[57] Herbert Ryan, Alison Smith, and Marcel Utz. Structural shimming for high-resolution nuclear magnetic resonance spectroscopy in lab-on-a-chip devices. *Lab on a Chip*, 14(10):1678–1685, 2014.

[58] JJ Hsu and GH Glover. Mitigation of susceptibility-induced signal loss in neuroimaging using localized shim coils. *Magnetic Resonance in Medicine*, 53(2):243–248, 2005.

[59] SGJ van Meerten, P Jan M van Bentum, and Arno PM Kentgens. Shim-on-chip design for microfluidic NMR detectors. *Analytical chemistry*, 90(17):10134–10138, 2018.

[60] Gabriele Varani and Ignacio Tinoco. RNA structure and NMR spectroscopy. *Quarterly reviews of biophysics*, 24(4):479–532, 1991.

[61] John Cavanagh, Wayne J Fairbrother, Arthur G Palmer III, and Nicholas J Skelton. *Protein NMR spectroscopy: principles and practice*. Elsevier, 1995.

[62] Timothy DW Claridge. *High-resolution NMR techniques in organic chemistry*, volume 27. Elsevier, 2016.

[63] Ulrich Haeberlen. *High Resolution NMR in solids selective averaging: supplement 1 advances in magnetic resonance*, volume 1. Elsevier, 2012.

[64] Gunter Engelhardt and Dieter Michel. *High-resolution solid-state NMR of silicates and zeolites*. John Wiley and Sons, New York, NY, 1987.

[65] Roger A Kautz, Wolfgang K Goetzinger, and Barry L Karger. High-throughput microcoil NMR of compound libraries using zero-dispersion segmented flow analysis. *Journal of combinatorial chemistry*, 7(1):14–20, 2005.

[66] Paul A Keifer. High-resolution NMR techniques for solid-phase synthesis and combinatorial chemistry. *Drug Discovery Today*, 2(11):468–478, 1997.

[67] S Kan, M Fan, and J Courtieu. A single-coil triple resonance probe for NMR experiments. *Review of Scientific Instruments*, 51(7):887–890, 1980.

[68] Marco Grisi, Gabriele Gualco, and Giovanni Boero. A broadband single-chip transceiver for multi-nuclear NMR probes. *Review of Scientific Instruments*, 86(4):044703, 2015.

[69] Hossein Davoodi, Nurdiana Nordin, Hirokazu Munakata, Jan G Korvink, Neil MacKinnon, and Vlad Badilita. Untuned broadband spiral micro-coils achieve sensitive multi-nuclear NMR TX/RX from microfluidic samples. *Scientific reports*, 11(1):1–12, 2021.

[70] F Hwang and DI Hoult. Automatic probe tuning and matching. *Magnetic resonance in medicine*, 39(2):214–222, 1998.

[71] Mazin Jouda, Saraí M Torres Delgado, Mehrdad Alinaghian Jouzdani, Dario Mager, and Jan G Korvink. ArduiTaM: accurate and inexpensive NMR auto tune and match system. *Magnetic Resonance*, 1(1):105–113, 2020.

[72] Michael A Ohliger and Daniel K Sodickson. An introduction to coil array design for parallel MRI. *NMR in Biomedicine: An International Journal Devoted to the Development and Application of Magnetic Resonance In vivo*, 19(3):300–315, 2006.

[73] Leslie Ying and Zhi-Pei Liang. Parallel MRI using phased array coils. *IEEE Signal Processing Magazine*, 27(4):90–98, 2010.

[74] Boris Keil, James N Blau, Stephan Biber, Philipp Hoecht, Veneta Tountcheva, Kawin Setsompop, Christina Triantafyllou, and Lawrence L Wald. A 64-channel 3T array coil for accelerated brain MRI. *Magnetic resonance in medicine*, 70(1):248–258, 2013.

[75] J Bruce Kneeland and James S Hyde. High-resolution MR imaging with local coils. *Radiology*, 171(1):1–7, 1989.

[76] James S Hyde, A Jesmanowicz, W Froncisz, J Bruce Kneeland, Thomas M Grist, and Nicholas F Campagna. Parallel image acquisition from noninteracting local coils. *Journal of Magnetic Resonance (1969)*, 70(3):512–517, 1986.

[77] X Zhang, JV Sweedler, and AG Webb. A probe design for the acquisition of homonuclear, heteronuclear, and inverse detected nmr spectra from multiple samples. *Journal of Magnetic Resonance*, 153(2):254–258, 2001.

[78] Ye Li, Zhentian Xie, Yong Pang, Daniel Vigneron, and Xiaoliang Zhang. ICE decoupling technique for RF coil array designs. *Medical physics*, 38(7):4086–4093, 2011.

[79] Ray F Lee, Randy O Giaquinto, and Christopher J Hardy. Coupling and decoupling theory and its application to the MRI phased array. *Magnetic Resonance in Medicine: An Official Journal of the International Society for Magnetic Resonance in Medicine*, 48(1):203–213, 2002.

[80] Roberta Kriegl, Jean-Christophe Ginefri, Marie Poirier-Quinot, Luc Darrasse, Sigrun Goluch, Andre Kuehne, Ewald Moser, and Elmar Laistler. Novel inductive

decoupling technique for flexible transceiver arrays of monolithic transmission line resonators. *Magnetic resonance in medicine*, 73(4):1669–1681, 2015.

[81] Xinqiang Yan, John C Gore, and William A Grissom. Self-decoupled radiofrequency coils for magnetic resonance imaging. *Nature communications*, 9(1):1–12, 2018.

[82] Moritz Becker, Mazin Jouda, Anastasiya Kolchinskaya, and Jan G Korvink. Deep regression with ensembles enables fast, first-order shimming in low-field NMR. *Journal of Magnetic Resonance*, page 107151, 2022.

[83] Yael Maguire, Isaac L Chuang, Shuguang Zhang, and Neil Gershenfeld. Ultra-small-sample molecular structure detection using microslot waveguide nuclear spin resonance. *Proceedings of the National Academy of Sciences*, 104(22):9198–9203, 2007.

[84] Eric G Sorte, Nathan A Banek, Michael J Wagner, Todd M Alam, and YuYe J Tong. In situ stripline electrochemical NMR for batteries. *ChemElectroChem*, 5(17):2336–2340, 2018.

[85] Anna Jo Oosthoek-de Vries, Pieter J Nieuwland, Jacob Bart, Kaspar Koch, Johannes WG Janssen, P Jan M van Bentum, Floris PJT Rutjes, Han JGE Gardeniers, and Arno PM Kentgens. Inline reaction monitoring of amine-catalyzed acetylation of benzyl alcohol using a microfluidic stripline nuclear magnetic resonance setup. *Journal of the American Chemical Society*, 141(13):5369–5380, 2019.

[86] Pedro F Silva, Mazin Jouda, and Jan G Korvink. Geometrically-differential NMR in a stripline front-end. *Journal of Magnetic Resonance*, 310:106659, 2020.

[87] Gregor Adriany, Pierre-Francois Van de Moortele, Florian Wiesinger, Steen Moeller, John P Strupp, Peter Andersen, Carl Snyder, Xiaoliang Zhang, Wei Chen, Klaas P Pruessmann, et al. Transmit and receive transmission line arrays for 7 Tesla parallel imaging. *Magnetic Resonance in Medicine: An Official Journal of the International Society for Magnetic Resonance in Medicine*, 53(2):434–445, 2005.

[88] CJ Snyder, L Delabarre, S Moeller, J Tian, C Akgun, P-F Van de Moortele, PJ Bolan, K Ugurbil, JT Vaughan, and GJ Metzger. Comparison between eight-and sixteen-channel TEM transceive arrays for body imaging at 7 T. *Magnetic resonance in medicine*, 67(4):954–964, 2012.

[89] Robert Ch Meier, Jens Höfflin, Vlad Badilita, Ulrike Wallrabe, and Jan G Korvink. Microfluidic integration of wirebonded microcoils for on-chip applications in nuclear magnetic resonance. *Journal of Micromechanics and Microengineering*, 24(4):045021, 2014.

[90] J Bart, JWG Janssen, PJM Van Bentum, APM Kentgens, and Johannes GE Gardeniers. Optimization of stripline-based microfluidic chips for high-resolution NMR. *Journal of magnetic resonance*, 201(2):175–185, 2009.

[91] Sunderarajan S Mohan, Maria del Mar Hershenson, Stephen P Boyd, and Thomas H Lee. Simple accurate expressions for planar spiral inductances. *IEEE Journal of solid-state circuits*, 34(10):1419–1424, 1999.

[92] Mikhail Kozlov and Robert Turner. Analysis of RF transmit performance for a 7T dual row multichannel MRI loop array. In *2011 Annual International Conference of the IEEE Engineering in Medicine and Biology Society*, pages 547–553. IEEE, 2011.

[93] S. G.J. van Meerten, K. C.H. Tijssen, P. J.M. van Bentum, and A. P.M. Kentgens. B1 gradient coherence selection using a tapered stripline. *Journal of Magnetic Resonance*, 286:60–67, 2018.

[94] Malcolm H Levitt. *Spin dynamics: basics of nuclear magnetic resonance*. John Wiley & Sons, 2013.

[95] Seungyong Hahn, Kwanglok Kim, Kwangmin Kim, Xinbo Hu, Thomas Painter, Iain Dixon, Seokho Kim, Kabindra R Bhattarai, So Noguchi, Jan Jaroszynski, et al. 45.5-tesla direct-current magnetic field generated with a high-temperature superconducting magnet. *Nature*, 570(7762):496–499, 2019.

[96] Philip J Hajduk, Tobias Gerfin, Jean-Marc Boehlen, Markus Häberli, Daniel Marek, and Stephen W Fesik. High-throughput nuclear magnetic resonance-based screening. *Journal of medicinal chemistry*, 42(13):2315–2317, 1999.

[97] Yen-Tse Cheng, Mazin Jouda, and Jan Korvink. Sample-centred shimming enables independent parallel NMR detection. *Scientific Reports*, 12(1):1–9, 2022.

[98] Thomas C Eisenschmid, Rein U Kirss, Paul P Deutsch, Sven I Hommeltoft, Richard Eisenberg, Joachim Bargon, Ronald G Lawler, and Alan L Balch. Para hydrogen induced polarization in hydrogenation reactions. *Journal of the American Chemical*

Society, 109(26):8089–8091, 1987.

[99] Jan H Ardenkjær-Larsen, Björn Fridlund, Andreas Gram, Georg Hansson, Lennart Hansson, Mathilde H Lerche, Rolf Servin, Mikkel Thaning, and Klaes Golman. Increase in signal-to-noise ratio of> 10,000 times in liquid-state nmr. *Proceedings of the National Academy of Sciences*, 100(18):10158–10163, 2003.

[100] Thad G Walker and William Happer. Spin-exchange optical pumping of noble-gas nuclei. *Reviews of modern physics*, 69(2):629, 1997.

[101] Albert W Overhauser. Polarization of nuclei in metals. *Physical Review*, 92(2):411, 1953.

[102] Bertrand Plainchont, Pierrick Berruyer, Jean-Nicolas Dumez, Sami Jannin, and Patrick Giraudeau. Dynamic nuclear polarization opens new perspectives for nmr spectroscopy in analytical chemistry, 2018.

[103] Danila A Barskiy, Aaron M Coffey, Panayiotis Nikolaou, Dmitry M Mikhaylov, Boyd M Goodson, Rosa T Branca, George J Lu, Mikhail G Shapiro, Ville-Veikko Telkki, Vladimir V Zhivonitko, et al. Nmr hyperpolarization techniques of gases. *Chemistry–A European Journal*, 23(4):725–751, 2017.

[104] C Russell Bowers and Daniel P Weitekamp. Parahydrogen and synthesis allow dramatically enhanced nuclear alignment. *Journal of the American Chemical Society*, 109(18):5541–5542, 1987.

[105] Ralph W Adams, Juan A Aguilar, Kevin D Atkinson, Michael J Cowley, Paul IP Elliott, Simon B Duckett, Gary GR Green, Iman G Khazal, Joaquín López-Serrano, and David C Williamson. Reversible interactions with para-hydrogen enhance nmr sensitivity by polarization transfer. *Science*, 323(5922):1708–1711, 2009.

[106] Lyrelle S Lloyd, Ralph W Adams, Michael Bernstein, Steven Coombes, Simon B Duckett, Gary GR Green, Richard J Lewis, Ryan E Mewis, and Christopher J Sleigh. Utilization of sabre-derived hyperpolarization to detect low-concentration analytes via 1d and 2d nmr methods. *Journal of the American Chemical Society*, 134(31):12904–12907, 2012.

[107] Petr Štěpánek, Clara Sanchez-Perez, Ville-Veikko Telkki, Vladimir V Zhivonitko, and Anu M Kantola. High-throughput continuous-flow system for sabre hyperpolarization. *Journal of Magnetic Resonance*, 300:8–17, 2019.

[108] Ralph W Adams, Simon B Duckett, Richard A Green, David C Williamson, and Gary GR Green. A theoretical basis for spontaneous polarization transfer in non-hydrogenative parahydrogen-induced polarization. *The Journal of chemical physics*, 131(19), 2009.

[109] Piotr Lepucki, Adam P Dioguardi, Daniil Karnaushenko, Oliver G Schmidt, and Hans-Joachim Grafe. The normalized limit of detection in nmr spectroscopy. *Journal of Magnetic Resonance*, 332:107077, 2021.

[110] Marek Plata, Manvendra Sharma, Marcel Utz, and Joorn M Werner. Fully automated characterization of protein–peptide binding by microfluidic 2d nmr. *Journal of the American Chemical Society*, 145(5):3204–3210, 2023.

[111] Ignacio Vazquez Lam. Analysis of improved howland current pump configurations. *Texas Instruments. https://www. ti. com/lit/an/sboa437/sboa437. pdf*, 2023.

[112] Brooke D Beier and Andrew J Berger. Method for automated background subtraction from raman spectra containing known contaminants. *Analyst*, 134(6):1198–1202, 2009.

[113] Christian Jutten and Jeanny Herault. Blind separation of sources, part i: An adaptive algorithm based on neuromimetic architecture. *Signal processing*, 24(1):1–10, 1991.

[114] Julianne L Kitevski-LeBlanc and R Scott Prosser. Current applications of 19f nmr to studies of protein structure and dynamics. *Progress in nuclear magnetic resonance spectroscopy*, 62:1–33, 2012.

[115] Ēriks Kupče, Lucio Frydman, Andrew G Webb, Jonathan RJ Yong, and Tim DW Claridge. Parallel nuclear magnetic resonance spectroscopy. *Nature Reviews Methods Primers*, 1(1):27, 2021.

Acknowledgments

Completing this thesis marks a challenging yet rewarding journey, and I extend my sincere appreciation to all those who have contributed to its success.

I express my deep appreciation to Prof. Jan Korvink for providing me with the opportunity to conduct research within the group. Over the four-year journey, I have gained a wealth of knowledge under his guidance. Without his support, accomplishing such a challenging project wouldn't have been possible.

Special thanks to my group leader, Dr. Mazin Jouda, whose guidance and support played a crucial role in shaping my academic and research experiences. I have learned a lot of skills and knowledge in RF and NMR from him. I'm thankful for all the moments we have in the discussion of our research.

I am grateful to the IMT at Karlsruhe Institute of Technology for providing a safe and comfortable research environment and essential resources during pandemic.

Appreciation extends to my room colleagues, Jingyi and Mengjia, for the companionship and enjoyable study times we shared. And all the countless discussions we had on NMR.

Many thanks go to research colleague Moritz Becker for collaboration and fruitful discussions, enriching this research experience. Beyond academia, the moments we shared during the three years are unforgettable.

Acknowledgment goes to countless individuals, including Jing, Yingkuan, Omar, Hossein, Mehrdrad, Ajmal, Soren, Chunhim, Bharat, Neil and Sagar. their helps and resources have contributed in various ways to the completion of this thesis, and I appreciate the moments and discussions we had together over more than four years.

Most importantly, heartfelt thanks to my family and my girlfriend for their unwavering encouragement, understanding, patience, and love. I am grateful for all the moments, happiness, and challenges we went through together.